MIT Open Access Articles

Constrained Density Functional Theory

The MIT Faculty has made this article openly available. ***Please share*** how this access benefits you. Your story matters.

Citation	Kaduk, Benjamin, Tim Kowalczyk, and Troy Van Voorhis. "Constrained Density Functional Theory." Chemical Reviews 112.1 (2012): 321–370. © 2012 American Chemical Society
As Published	http://dx.doi.org/ 10.1021/cr200148b
Publisher	American Chemical Society (ACS)
Version	Author's final manuscript
Citable link	http://hdl.handle.net/1721.1/74564
Terms of Use	Article is made available in accordance with the publisher's policy and may be subject to US copyright law. Please refer to the publisher's site for terms of use.

Massachusetts Institute of Technology

DSpace@MIT

Constrained Density Functional Theory

Benjamin Kaduk, Tim Kowalczyk and Troy Van Voorhis
Department of Chemistry, Massachusetts Institute of Technology
77 Massachusetts Avenue, Cambridge MA 02139

May 2, 2011

Contents

1 Introduction

Among the diverse and ever-expanding array of approaches to the electronic structure problem, the rise of approximate density functional theory (DFT) as the method of choice for practical calculations has been nothing short of meteoric.[1,2] The stage for this explosion of interest was set by three pivotal developments: the establishment of the ground-state energy as a functional of the density by the Hohenberg-Kohn theorems;[3] the Kohn-Sham reformulation of the problem in terms of self-consistent field (SCF) equations with an approximate exchange-correlation (XC) functional;[4] and the invention of accurate approximations to the XC functional itself.[5–7]

A key distinction of Kohn-Sham DFT, compared to *ab initio* methods based on the Hartree-Fock (HF) reference wavefunction, is the favorable scaling with system size that can be obtained with many popular XC functionals. Thus, approximate DFT accounts for much of the dynamical correlation energy absent in HF theory, but at roughly the cost of a HF calculation.[8] This superior balance of accuracy and low computational overhead has spurred much of the growth in popularity of approximate DFT over the last two decades. For traditional semilocal and hybrid functionals, the computational cost of a single-point energy calculation scales nominally as $O(N^3)$, where N is the number of basis functions; a variety of techniques have since been devised to obtain linear-scaling implementations of DFT for extended systems.[9,10] Fast implementations of Kohn-Sham DFT with Gaussian or plane-wave basis sets are available in many modern electronic structure packages.

Thanks to its computational tractability, DFT has been at the forefront of efforts to extend the reach of quantum chemistry beyond the traditional realms of single-point energies and geometries in the gas phase. DFT is now routinely employed alongside spectroscopic and electrochemical analyses[11,12] and is invoked in the interpretation of novel organic and organometallic reactivity.[13,14] The favorable accuracy-to-cost ratio of approximate DFT for

large systems has made it the method of choice for quantum chemical studies of biomolecular systems[15–17] and has enabled classical molecular dynamics simulations on high-dimensional Born-Oppenheimer potential energy surfaces (PES).[18,19] The introduction of a fictitious dynamics for the orbitals in the Car-Parrinello approach[20] further reduces computational costs and has enabled density functional simulations of bioactive and reactive species.[21–23]

The establishment of linear-response time-dependent DFT (LR-TDDFT) as a viable, and in principle exact,[24,25] formalism for obtaining excited states from DFT laid the groundwork for its routine application to excited states in organic compounds[26] and transition metal complexes.[27] Paired with a classical force field via QM/MM or ONIOM techniques, DFT and TDDFT have gained traction for computational modeling of systems once only accessible to classical simulation, such as enzymes[28] and chromophores strongly coupled to a solvent bath.[29,30] DFT has been enlisted to shed light on a dizzying variety of physical and chemical applications, from structure and reactivity at surfaces[31] and screening of organic dyes[32] to the characterization of superconductors[33] and materials simulations for art preservation.[34]

In light of the many strengths and diverse applications of DFT, it is easy to get the impression that the current stable of approximate XC functionals is adequate for all of chemistry. On the contrary, the scope of applicability of traditional functionals is limited by a number of shortcomings which in many cases lead to qualitatively incorrect predictions of chemical structure and reactivity. Traditional functionals suffer to varying degrees from self-interaction error (SIE) which results in spurious delocalization of the density with semilocal functionals but can also cause the opposite (localization) error in some hybrids.[35,36] These errors are largely responsible for the failures of traditional functionals for such fundamental properties as barrier heights of chemical reactions,[37] energies and structures of long-range charge-separated states,[38] and magnetic exchange couplings.[39] Furthermore, noncovalent van der Waals interactions are generally either absent entirely or treated incompletely by traditional functionals, although progress in addressing this problem has been rapid in recent

years.[40–43]

The shortcomings of traditional functionals naturally plague TDDFT as well. The LR-TDDFT approach is better suited for some types of excited states than for others. For instance, charge-transfer excitation energies are often grossly underestimated by LR-TDDFT with traditional functionals in the adiabatic approximation.[44,45] Conical intersections predicted by these methods can be qualitatively incorrect.[46,47] Some exotic excitations such as double excitations also pose problems for LR-TDDFT with traditional functionals and frequency-independent XC kernels.[46,48]

Strategies for addressing these shortcomings can be roughly grouped into three categories:

1. Wait patiently for the arrival of the exact functional; or if impatient, design better approximations to the exact functional.

2. Abandon the DFT approach in favor of systematically improvable but computationally demanding *ab initio* methods.

3. Adapt calculations involving existing traditional functionals to mitigate known shortcomings.

Of course, one can devise methods that fall between categories 1 and 2 by combining certain features of DFT and *ab initio* techniques.[49,50]

This review explores one particular method, constrained DFT (CDFT), that falls into the third category. The significance of CDFT is necessarily ephemeral, as improvements in functional approximations or *ab initio* techniques will eventually render CDFT unnecessary (we hope). However, in the here and now, CDFT has proven to be a valuable tool in the electronic structure toolbox, and this review presents an overview of its role in contemporary research. At a basic level, CDFT offers a partial workaround to some of the detrimental effects of SIE discussed above. However, CDFT also provides a direct route to diabatic electronic states and, by extension, to charge transfer excited states, using the basic machinery

of the Kohn-Sham SCF procedure. At a deeper level, these excited states lead naturally to the construction of physically motivated effective Hamiltonians for a variety of problems. The diversity of applications presented in this review does not reflect the breadth of CDFT so much as the narrowness of commonly used density functionals: there are many places CDFT is useful because there is a wide range of problems for which a truly satisfactory XC functional does not yet exist. Of course, solutions in each category enumerated above are being actively pursued and refined, and there is good reason to anticipate that solutions of all three types will extend the reach of electronic structure theory — and of DFT in particular — to ever more complex problems.

The remainder of the review is structured as follows. Section 2 develops the theory and working equations of CDFT. In the two subsequent sections, we illustrate applications of charge-constrained and spin-constrained CDFT states to problems in electron transfer (section 3) and in the chemistry of low-lying spin states (section 4), respectively. Section 5 addresses the question of how to compute couplings between CDFT states, with illustrative examples. The use of CDFT as a tool for parameterizing model Hamiltonians is considered in section 6, where we also discuss configuration-interaction (CI) expansions of CDFT states for improved treatment of transition states and conical intersections. Section 7 presents a handful of other category 3 methods that cover the same applications as CDFT: techniques that overcome SIE, or define diabatic states, or describe low-lying excited states through modifications of the Kohn-Sham SCF procedure. We conclude with our impression of the role to be played by CDFT and related methods in the future development and application of approximate DFT.

2 Theory

In this section, we outline the working equations of CDFT and describe how they can be solved efficiently. Development of modern CDFT has benefitted greatly from the foresight of the original presentation of CDFT, which fully anticipated all manner of applications and formalisms.[51] In modern molecular usage, the theory of CDFT has been refined so that constraints are typically phrased in terms of the charge and spin on arbitrary molecular fragments, which are defined in terms of an atomic charge prescription.[38,52–55] This portrayal allows for multiple constrained fragments, analytical gradients, and efficient determination of the self-consistent constraint potential. In this section we introduce the general theory with emphasis on the formulation in terms of populations. We close the section with a few illustrations of best practices in using constraints to solve chemical problems.

2.1 Original CDFT Equations

The first presentation of a constrained DFT formalism is due to Dederichs *et al.*[51] and proceeds as follows. Suppose we seek the ground electronic state of a system subject to the constraint that there are N electrons in a volume Ω. One can accomplish this by supplementing the traditional DFT energy functional, $E[\rho(\mathbf{r})]$, with a Lagrange multiplier:

$$E(N) = \min_{\rho} \max_{V} \left[E[\rho(\mathbf{r})] + V \left(\int_{\Omega} \rho(\mathbf{r}) d^3r - N \right) \right] \tag{1}$$

The addition of a single Lagrange multiplier term $V\left(\int_{\Omega} \rho(\mathbf{r}) d^3r - N\right)$ is sufficient to effect a constrained optimization that yields the lowest-energy state with exactly N electrons in the volume Ω. This would clearly be useful, for example, in looking at the localization of charge around an impurity. Continuing along these lines, one can easily come up with other interesting constraint formulations.[51] One could constrain local d (or f) charge variation in

transition (or rare-earth) metals:

$$E(N) = \min_{\rho} \max_{V_d} \left[E[\rho(\mathbf{r})] + V_d \left(\int \rho_d(\mathbf{r}) d^3r - N_d \right) \right] \tag{2}$$

or the (net) magnetization:

$$E(N) = \min_{\rho} \max_{H} \left[E[\rho(\mathbf{r})] + H \left(\int_{\Omega} m(\mathbf{r}) d^3r - M \right) \right] \qquad \left[m(\mathbf{r}) \equiv \rho^{\alpha}(\mathbf{r}) - \rho^{\beta}(\mathbf{r}) \right]. \tag{3}$$

One could go even further and note that the magnetization in a given system need not have a uniform orientation throughout, so that one could partition the system into magnetization domains with different axes of magnetization. In this case, the magnetization on each domain would become an independent parameter, with the energy $E(\vec{M}_1, \ldots, \vec{M}_N)$ being a function of the constrained parameters.

All of the constraints above can be cast in a unified notation:[52]

$$W[\rho, V; N] \equiv E[\rho] + V \left(\sum_{\sigma} \int w^{\sigma}(\mathbf{r}) \rho^{\sigma}(\mathbf{r}) d^3r - N \right) \tag{4}$$

$$E(N) = \min_{\rho} \max_{V} W[\rho, V; N]. \tag{5}$$

Here, one introduces a (spin-dependent) weight function, $w^{\sigma}(\mathbf{r})$, that defines the property of interest. For example, to match equation (1), $w^{\alpha}(\mathbf{r}) = w^{\beta}(\mathbf{r})$ would be the characteristic function of Ω. To match equation (3), $w^{\alpha}(\mathbf{r}) = -w^{\beta}(\mathbf{r})$ would again be the characteristic function of Ω. In this way, we think of the various constraints as specific manifestations of a single unified formalism.

These core equations have been widely used for determining the U parameter in LDA+U, Anderson, and Hubbard models,[56–71] frequently in combination with the Hund's rule exchange parameter J.[72–86] A closely related fixed spin moment (FSM) class of methods,

which will not covered in the present review, originated in tandem with the original CDFT work of Dederichs *et al.*[87–89] Related use of CDFT for producing constrained magnetic configurations has been rather widespread,[90–105] and the ability to fix different spin orientations at distinct sites allows for *ab initio* spin dynamics[106] with extension to relativistic spin dynamics.[107] A survey of the results based upon CDFT finds that virial and Hellmann-Feynman theorems have been given for CDFT,[108] and the theory has been generalized for application to the inverse Kohn-Sham problem.[109] CDFT has found use examining charge localization and fluctuation in the d density of bulk iron,[110] studying localized excitons on the surface of GaAs(110),[111] and constraining core orbital occupations to obtain core excitation energies.[112] Combining Janak's theorem and its integrated version the Slater formula with CDFT yields an efficient method for determining the charge on quantum dots,[113] and using CDFT to constrain orbitals to a fixed atomic form provides a projection operator for use in self-interaction correction (SIC) calculations;[114] the CDFT equations have been reformulated for use with DFTB+ tight-binding models.[115] With this slew of varied applications, the theory of constraining properties of DFT states has proven quite versatile, being applied to study a wide variety of phenomena. In recent years, it has seen broad use constraining the charge and spin on molecular fragments, which will be of particular importance for this review.

2.2 Constrained Observables

There is a great deal of flexibility available for constraining the ground-state density in equation (4), since in an unrestricted KS DFT framework an arbitrary constraint may be applied to the integrated population of each spin, over any number of arbitrary regions of space, subject to an arbitrary weighting scheme. In practice, this degree of flexibility is simply overwhelming, and requires some way to streamline the choice of appropriate constraints. In this spirit, real-space atomic charge schemes have driven much of the modern work with

CDFT: they are flexible enough to define a variety of states in accord with chemical intuition, but at the same time compact enough that the number of reasonable constraints is not too large.

First, it is important to note that a variety of commonly used prescriptions for computing the charge on atom A can be cast in the form

$$N_A \equiv \int w_A(\mathbf{r})\rho(\mathbf{r})d^3r. \tag{6}$$

Thus, constraining the charge or spin using one of these population prescriptions is just a special case of equation 4. The easiest to understand is probably the Voronoi method,[116] which partitions space up into cells Ω_I consisting of all points closest to atom I. The number of electrons on atom A is then

$$N_A \equiv \int_{\Omega_A} \rho(\mathbf{r})d^3r \tag{7}$$

which is obviously a special case of equation (1). The Becke population scheme is similar:[117] here one defines a weight function, w_I^{Becke}, that is nearly unity inside the Voronoi cell, nearly zero outside and smoothly connects the two limits. The number of electrons on A is then

$$N_A \equiv \int w_A^{\text{Becke}}(\mathbf{r})\rho(\mathbf{r})d^3r. \tag{8}$$

In a completely different fashion, the Hirshfeld (or Stockholder) partitioning can also be written in terms of atomic weight functions.[118] In the Hirshfeld scheme, one constructs a promolecule density, $\tilde{\rho}(\mathbf{r})$ that is just the sum of (usually spherically averaged) atomic densities, $\rho_I(\mathbf{r})$. One then defines an atomic weight function and number of electrons respectively by:

$$w_A^{\text{Hirshfeld}}(\mathbf{r}) \equiv \frac{\rho_A(\mathbf{r})}{\tilde{\rho}(\mathbf{r})} \qquad N_A \equiv \int w_A^{\text{Hirshfeld}}(\mathbf{r})\rho(\mathbf{r})d^3r. \tag{9}$$

Similar constructions apply to the variations on this theme — including Hirshfeld-I[119] and

iterated Stockholder[120] — with mild adjustments to the definitions of w_A. It is also in principle possible to phrase more sophisticated schemes — such as partition theory[121–123] and Bader's atoms-in-molecules approach[124] — in terms of a weight function w_A, although to our knowledge these connections have never been made in the context of CDFT. Finally, there are charge prescriptions (including the popular Mulliken,[125] Löwdin[126] and NBO[127] schemes) that can not be written in terms of the density. In these cases, the charge is defined by partitioning the one-particle density *matrix* (1PDM) which technically goes outside the scope of constrained *density* functional theory. However, in practice it is a simple matter to apply constraints to the 1PDM within the same formalism[52,53] and thus when one constrains Löwdin or Mulliken populations it is still colloquially referred to as CDFT.

With a prescription for atomic charges in hand, one can easily build up a weight, w_F, for the charge on a fragment F, consisting of any group of atoms within a molecule or solid. The charge on the fragment is just the sum of the atomic charges, so that

$$\begin{aligned} N_F &\equiv \sum_{I\in F} N_I = \sum_{I\in F} \int w_I(\mathbf{r})\rho(\mathbf{r})d^3r \\ &= \int \sum_{I\in F} w_I(\mathbf{r})\rho(\mathbf{r})d^3r \equiv \int w_F(\mathbf{r})\rho(\mathbf{r})d^3r \qquad\qquad [w_F(\mathbf{r}) \equiv \sum_{I\in F} w_I(\mathbf{r})]. \end{aligned} \tag{10}$$

We can thus constrain the number of electrons on any fragment by adding the Lagrangian term

$$V_F \left(\int w_F(\mathbf{r})\rho(\mathbf{r})d^3r - N_F \right) \tag{11}$$

to the energy expression. Here N_F is the total number of electrons on the fragment, though for practical calculations the nuclear charge is subtracted off and only the net number of electrons on the fragment ($-q_F \equiv N_F - Z_F$) need be specified as input to the calculation.

For magnetic systems, we would also like to be able to constrain the local spin using population operators. That is, we would like the equivalent of equation (3) for subsets of the

entire system. To accomplish this, we note that the number of electrons of spin σ ($\sigma = \alpha, \beta$) on F is just

$$N_F^\sigma \equiv \int w_F(\mathbf{r})\rho^\sigma(\mathbf{r})d^3r. \tag{12}$$

The net spin polarization (i.e. the local M_S value) is $(N_\alpha - N_\beta)/2$, where the factor of $1/2$ reflects the fact that electrons are spin-1/2 particles. We can thus constrain the net magnetization of any fragment by adding the Lagrangian term:

$$H_F \left(\int w_F(\mathbf{r})(\rho^\alpha(\mathbf{r}) - \rho^\beta(\mathbf{r}))d^3r - M_F \right) \tag{13}$$

M_F is then the net number of spin up electrons on the fragment, which is the same as twice the M_S value.

Finally, we can apply any number of spin and charge constraints by adding a number of such terms:

$$\begin{aligned} W[\rho, V_F, H_{F'}; N_F, M_{F'}] \equiv E[\rho] &+ \sum_F V_F \left(\int w_F(\mathbf{r})\rho(\mathbf{r})d^3r - N_F \right) \\ &+ \sum_{F'} H_{F'} \left(\int w_{F'}(\mathbf{r})(\rho^\alpha(\mathbf{r}) - \rho^\beta(\mathbf{r}))d^3r - M_{F'} \right) \end{aligned} \tag{14}$$

$$E(N_F, M_{F'}) = \min_\rho \max_{V_F, H_{F'}} W[\rho, V_F, H_{F'}; N_F, M_{F'}]. \tag{15}$$

The actual form of w_F (and thus the constraint) will depend on the choice of target populations as described above. But it is a trivial matter to write the equations in a manner that is independent of the population, and we will maintain this level of abstraction in what follows.

2.3 Choosing a Constraint

Even if we restrict our attention only to charge and spin constraints, in any given application one still has several choices to make about how an appropriate constraint should be defined. What atomic population should be used? Which atoms should be included in the fragment? Does the basis set matter? For the most part, the answers to these questions must be determined on a case-by-case basis either by trial and error or using chemical intuition. However, the literature does contain a number of empirically determined guidelines that can be helpful in practice:

- **Mulliken populations are not reliable.** One abiding rule is that Mulliken populations are unrealistic in CDFT. For example, in Figure 1, Mulliken populations spuriously predict that separating charge in dinitrogen to obtain the N^+N^- configuration should only require a fraction of an eV, whereas all other prescriptions predict energies on the order of 5-10 eV. This failure can be linked to the ability of Mulliken populations to become negative in some regions of space.[128]

- **When diffuse functions are involved, density based prescriptions are more stable.** Here again, the observation is tied to a known weakness of an atomic population scheme: AO-based schemes (like Löwdin, Mulliken or NBO) tend to get confused when diffuse functions are added.[129] In the worst cases, this fault keeps Löwdin-CDFT energies and properties from converging as the size of the basis set is increased. Such a case is illustrated in Table 1, which presents the electronic coupling (discussed in section 5) between benzene and chlorine at two different separations for a variety of basis sets. Clearly the Löwdin result shows an unreasonably large increase as the basis size increases, while the density-based Becke prescription shows fast convergence. Real-space population schemes such as the Becke weighting scheme and Hirshfeld partitioning correct for the broad spread of diffuse basis functions, giving good results for

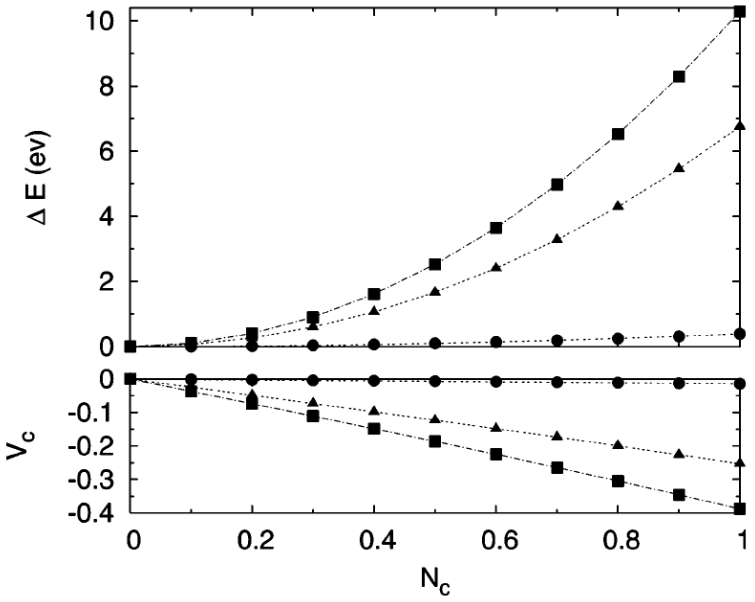

Figure 1: The energy and constraint potential as a function of charge separation in N_2 with different charge prescriptions. Squares: Becke population; triangles: Löwdin population; dots: Mulliken population. Calculations performed using B3LYP in a 6-31G* basis set. Used with permission from reference 53.

CDFT.[53,130]

Table 1: Diabatic coupling (in mHartree) for electron transfer from benzene to Cl. Reproduced with permission from ref 38.

d (Å)	0.604		1.208	
	Löwdin	Becke	Löwdin	Becke
6-31G	21.3	58.2	30.1	65.9
6-31G(d)	21.0	56.9	29.9	64.8
6-31+G(d)	39.6	46.7	46.1	53.9
VDZ-ANO	95.3	48.8	94.0	56.1

- **Larger fragments give more consistent results.** This conclusion has mainly been drawn from the application of CDFT to predict exchange couplings in magnetic organometallic compounds, where there is a wealth of experimental data to compare to.[39] The qualitative picture is that all excess spin resides on the metal atoms. However, in practice, constraining the net spin of the metal atoms alone using any of the

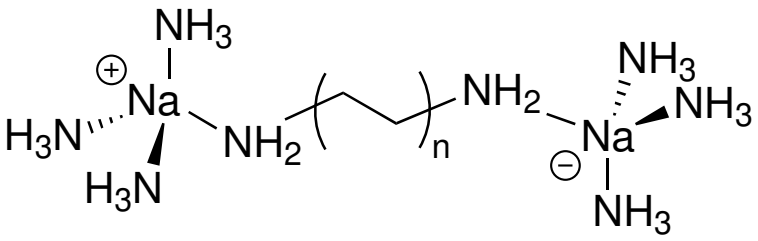

Figure 2: Structure of the n-alkyl di(sodium tetraamine) donor-acceptor complexes discussed in this section.

standard schemes gives unreasonable exchange couplings. The most reliable results are obtained if the fragments are made as large as possible; if there are two metals (A and B) then every atom in the molecule is assigned either to fragment A or fragment B, even if there is thought to be no net magnetization on that fragment. Likewise, for charge transfer, making the fragments large helps stabilize the excess charge, e.g. constraining a metal center and its ligands (instead of just the metal), or not leaving an unconstrained "bridge" in a fully conjugated aromatic charge-transfer system. Making the constrained region too small can cause the constraint to be artificially too strong; a charged metal center really will delocalize charge to its ligands (Figure 3), and a charge-transfer state in a conjugated system will delocalize the electron and hole as much as possible to stabilize itself. By making the CDFT constraint region as large as possible, the minimum perturbation needed to enforce the constraint can be applied, with the system naturally seeking the correct level of localization. It is important to emphasize that adding "spectator" atoms to a fragment does not necessarily place any charge or spin on the spectator; adding the atom to the fragment merely means that the variational CDFT optimization *can* place additional charge or spin on that atom, not that it will. For example, in Figure 3, when half of the bridge is added to each fragment, not all of the bridge carbons will have extra charge.

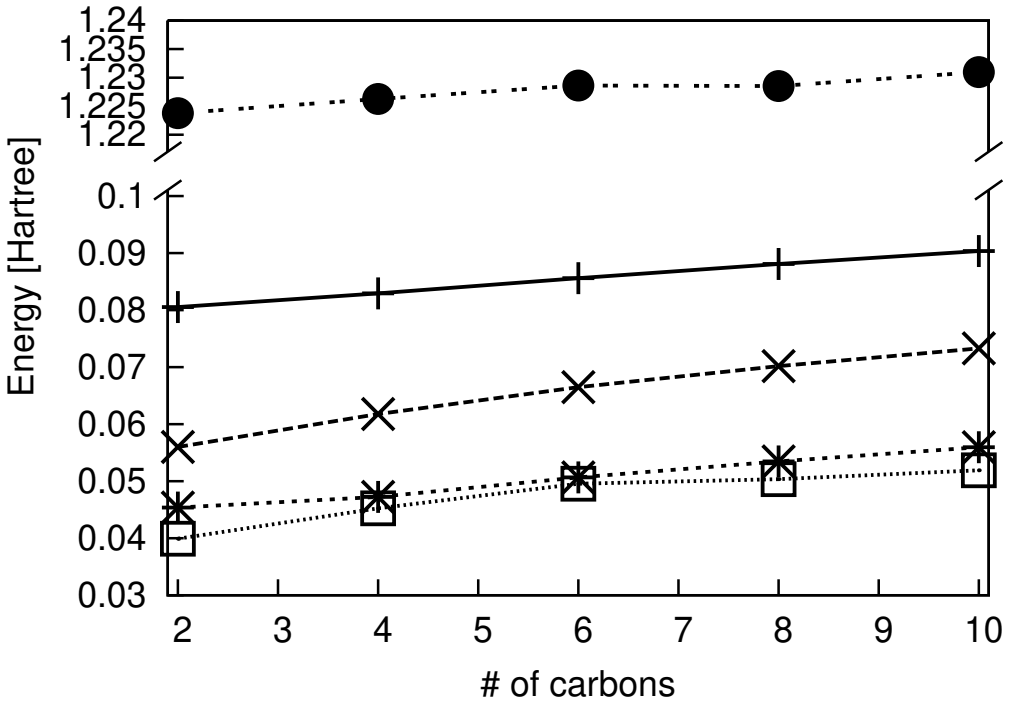

Figure 3: The energy behavior of $[Na(NH_3)_3]^+H_2N(CH_2)_nNH_2[Na(NH_3)_3]^-$ with the constraint applied to just the metal atoms ($\bullet$), the $Na(NH_3)_3$ groups ($+$), the metal and ammonias and the amine group of the bridge ($\times$), splitting the complex in two down the middle of the bridge ($*$), or with a promolecule-modified constraint applied to the $Na(NH_3)_3$ groups ($\square$). Energy differences are measured with respect to the ground-state DFT energy for each system, and plotted as a function of the number of carbons in the alkyl amine. Geometries are constructed with bond lengths and angles corresponding to the optimized geometry of the eight-carbon system. The metal-only constraint is comically overstrong (note the broken y-axis), while expanding the constraint region to include the ligands or the ligands plus bridge leads to reasonable results. The constraint in ($*$) is a weaker constraint than all the other curves except the promolecule-corrected constraint on the sodium and ammonias; this is because when the system is literally divided in two, only one constraint region is needed — the other partitionings require that one region is constrained to $+1$ charge and the other to -1, with an implicit constraint that the bridge is neutral.

- **When possible, constrain charge and spin together.** Suppose you were interested in charge transfer between C_{60} and C_{70} (i.e. $C_{60}^{+} \cdots C_{70}^{-}$). You could generate this state in one of two ways: either constrain only the charge (e.g. $q_{C_{60}} = +1$) or the charge and spin (e.g. $q_{C_{60}} = +1$ and $M_{C_{60}} = 1$). In many cases these two routes will give nearly identical answers (as long as the calculations are spin-unrestriced). However, in the cases where they differ significantly, it can often be the case that constraining the charge leads to a state that still has significant overlap with the ground state. This phenomenon is known as "ground state collapse" and generally leads to erroneous results for energetics. Thus, to be on the safe side, it seems best to constrain both charge and spin rather than just charge alone.

- **There can be many equivalent ways of specifying the same state.** Returning to the $C_{60}^{+}...C_{70}^{-}$ example, because the overall charge on the system is fixed, specifying $q_{C_{60}} = +1$ or $q_{C_{70}} = -1$ would obtain exactly the same answer in CDFT. Alternatively, requiring that $q_{C_{60}} - q_{C_{70}} = +2$ would also give the same result. These observations are general: it is always mathematically equivalent to describe the system with constraint N_A on A and with constraint $N_B \equiv N - N_A$ on $B \equiv \mathbb{R}^3 \setminus A$. The ability to add and subtract constraints in this manner is reminiscent of the elementary row operations of linear algebra, allowing for different presentations of equivalent physical constraints. The charge difference constraint illustrated above has been used rather extensively[53,130] because, in cases where the constraint regions do not cover all of space, the charge difference constraint is insensitive to fluctuations in the overall charge.

- **When donor and acceptor are very close to one another, CDFT may fail.** When atoms are bound together in molecules, there is no perfect prescription for assigning atomic charges: at some point any method for dividing delocalized charge becomes arbitrary. It is particularly challenging when atoms are very close to each

other, e.g. the two nitrogen atoms in N_2, illustrated in Figure 1. Here, even when two reasonable charge prescriptions (Löwdin and Becke) are used, the energy of the N^+N^- state varies by more than 3 eV. This is clearly an unacceptably large error for chemical purposes and trying more population prescriptions will not fix the problem. There is simply no unambiguous way to apportion the charge in N_2 to the different nitrogen atoms. In section 2.5 we will discuss how these problems can be mitigated somewhat by using fragment densities, but they cannot be entirely ignored.

Thus, while defining an appropriate constraint is not a trivial task, in practice we at least have some empirical guidelines of what to do and what not to do when we approach a new problem with CDFT.

2.4 Implementation

A full implementation of CDFT needs to find the density which obeys the specified charge/spin constraints at SCF convergence. That is to say, it needs to solve for the stationary points of the Lagrangian in equation (15). Ideally, we would like to solve these equations with approximately the same computational cost as a regular KS-DFT calculation. Toward that end, we re-write equation 15 as

$$E(N_k) = \min_{\rho} \max_{V_k} W[\rho, V_k; N_k] = \min_{\rho} \max_{V_k} \left[E[\rho] + \sum_k V_k \left(\int \sum_{\sigma} w_k^{\sigma}(\mathbf{r}) \rho^{\sigma}(\mathbf{r}) d^3r - N_k \right) \right] \tag{16}$$

where the index k indexes charge and spin constraints: for charges $V_k \equiv V_F$ and $w_k^{\alpha} = w_k^{\beta} = w_F$, while for spins $V_k \equiv H_F$ and $w_k^{\alpha} = -w_k^{\beta} = w_F$. This notation obfuscates the meaning somewhat, but makes the equations uniform. Recall that the DFT energy expression is

defined by

$$E[\rho] = \sum_{\sigma} \sum_{i}^{N_\sigma} \left\langle \phi_{i\sigma} \middle| -\frac{1}{2}\nabla^2 \middle| \phi_{i\sigma} \right\rangle + \int v_n(\mathbf{r})\rho(\mathbf{r}) d^3r + J[\rho] + E_{xc}[\rho^\alpha, \rho^\beta] \tag{17}$$

where the terms on the right hand side are, in order, the electronic kinetic, electron-nuclear attraction, Coulomb and exchange-correlation energies. Requiring that equation (16) be stationary with respect to variations of the orbitals, subject to their orthonormality, yields the equations:

$$\left(-\frac{1}{2}\nabla^2 + v_n(\mathbf{r}) + \int \frac{\rho(\mathbf{r}')}{|\mathbf{r} - \mathbf{r}'|} d^3r' + v_{xc}^\sigma(\mathbf{r}) + \sum_k V_k w_k^\sigma(\mathbf{r}) \right) \phi_{i\sigma} = \epsilon_{i\sigma} \phi_{i\sigma} \tag{18}$$

with Hermitian conjugate for $\phi_{i\sigma}^*$. These equations are just the standard Kohn-Sham equations with the addition of some new potentials. These potentials are proportional to the Lagrange multipliers, which illustrates the physical mechanism by which CDFT controls charges and spins: it alters the potential in such a way that the ground state in the new potential satisfies the desired constraint. Another way to say it is that the excited state of the unperturbed system can be approximated by the ground state of the system in the presence of the constraining potential. Thus, CDFT takes the fact that the KS approach is exact for any potential and exploits it to obtain information about nominally inaccessible excited states.

However, these constraint potentials are not yet fully specified — though the w_k are given as parameters, the Lagrange multipliers V_k are only implicitly defined by the constraints on the fragment charges and spins. These constraints become clear when we attempt to make

W stationary with respect to the V_i:

$$\frac{dW}{dV_k} = \sum_{\sigma} \sum_{i}^{N_\sigma} \left(\frac{\delta W}{\delta \phi_{i\sigma}^*} \frac{\partial \phi_{i\sigma}^*}{\partial V_k} + \text{cc} \right) + \frac{\partial W}{\partial V_k} \tag{19}$$

$$= \sum_{\sigma} \int w_k^\sigma(\mathbf{r}) \rho^\sigma(\mathbf{r}) d^3r - N_k \tag{20}$$

$$= 0 \tag{21}$$

where the eigencondition $\delta W / \delta \phi_{i\sigma}^* = 0$ has been used. Note that only the constraint with index k remains after differentiation, even when multiple constraints are imposed on the system, and the stationary condition of the derivative being zero enforces the desired charge/spin constraints.

The separate conditions of equations (18) and (21) imply that V_k and ρ must be determined self-consistently to make W stationary. This is somewhat daunting, as the Lagrangian optimization is typically only a stationary condition — that is, it is *not* typically a pure maximization or minimization. As a practical matter, it is much more difficult to locate indefinite stationary points than maxima or minima. For example, it is significantly harder to find a transtition state (an indefinite stationary point) than an equilibrium structure (a minimum). However, even though the CDFT stationary point is not a maximum or a minimum, it is easy to locate, because one can show that the desired solution is a *minimum* with respect to ρ and a *maximum* with respect to V_k.[52,53] Thus, the stationary point can be solved for via alternating between minimization along one coordinate (the density) followed by maximization along the others (the potentials).

To see this, note that for any fixed V_k, equations (18) determine a unique set of orbitals, $\phi_i[V_k]$. These orbitals define a density $\rho[V_k]$, which can then be used as input to W. In this manner, one can think of W as a function *only* of V_k: $W(V_k)$. We can work out the second

derivatives of this function:[53]

$$\frac{\partial^2 W}{\partial V_k \partial V_l} = \sum_\sigma \sum_i^{N_\sigma} \int w_k^\sigma(\mathbf{r}) \phi_{i\sigma}^*(\mathbf{r}) \frac{\delta \phi_{i\sigma}(\mathbf{r})}{\delta[V_l w_l^\sigma(\mathbf{r}')]} w_l^\sigma(\mathbf{r}') d^3r d^3r' + \text{cc} \tag{22}$$

$$= \sum_\sigma \sum_i^{N_\sigma} \int w_k^\sigma(\mathbf{r}) \phi_{i\sigma}^*(\mathbf{r}) \sum_{a \neq i} \frac{\phi_{a\sigma}^*(\mathbf{r}') \phi_{i\sigma}(\mathbf{r}')}{\epsilon_{i\sigma} - \epsilon_{a\sigma}} \phi_{a\sigma}(\mathbf{r}) w_l^\sigma(\mathbf{r}') d^3r d^3r' + \text{cc} \tag{23}$$

$$= 2 \sum_\sigma \sum_i^{N_\sigma} \sum_{a > N_\sigma} \frac{\langle \phi_{i\sigma} | w_k^\sigma | \phi_{a\sigma} \rangle \langle \phi_{a\sigma} | w_l^\sigma | \phi_{i\sigma} \rangle}{\epsilon_{i\sigma} - \epsilon_{a\sigma}} \tag{24}$$

where first-order perturbation theory is used in evaluating the functional derivative $\delta \phi_{i\sigma}(\mathbf{r}) / \delta[V_l w_l^\sigma(\mathbf{r}')]$. The index i only covers the occupied orbitals of the constrained state, whereas the index a need only cover the virtual orbitals, as the summand is antisymmetric in i and a. This Hessian matrix is nonpositive definite because[53]

$$\sum_{k,l}^m V_k \frac{\partial^2 W}{\partial V_k \partial V_l} V_l = 2 \sum_\sigma \sum_i^{N_\sigma} \sum_{a > N_\sigma} \frac{\left| \langle \phi_{i\sigma} | \sum_{k=1}^m V_k w_k^\sigma | \phi_{a\sigma} \rangle \right|^2}{\epsilon_{i\sigma} - \epsilon_{a\sigma}} \leq 0 \tag{25}$$

This holds because the KS method chooses the lowest-energy eigenstates as the occupied orbitals, so for every occupied orbital i and virtual orbital a, $\epsilon_{i\sigma} \leq \epsilon_{a\sigma}$. Thus, the overall Hessian product is nonpositive, as desired, giving a stationary point as a maximum.

Having worked out the second derivatives, we see two features that simplify the CDFT optimization procedure. First, the condensed version of W is globally concave in the V_k, giving a *unique* fixed point which satisfies all the applied constraints. Thus, there can be no confusion about local versus global maxima. Second, since both the first and second derivatives of $W(V_k)$ are easily computed, rapidly converging algorithms such as Newton's method can be used to locate its stationary point. Convergence to the constrained SCF minimum can thus be achieved by means of a nested-loop algorithm with outer SCF loop and inner constraint loop. The outer loop closely resembles a normal DFT calculation, with SCF iterations being performed to optimize the orbitals. Within each step of the outer loop,

a second loop of microiterations is performed to determine the Lagrange multipliers V_k that make the density satisfy the charge and spin constraints (equations (10) and (12)). Because the V_k contribute to the Fock matrix, the orbitals must be redetermined by diagonalization of the Fock matrix at each microiteration step. Fortunately, the V_k contribution to the Fock matrix is easy to calculate and a full build with exchange and correlation contributions is not necessary, making the microiterations relatively cheap for atom-centered basis sets. After the first few iterations of the outer loop, it is common for the inner loop to converge after only two or three microiterations.

Essentially all available SCF codes use a convergence accelerator, such as direct inversion in the iterative subspace (DIIS). Since CDFT introduces an extra layer of microiterations at each SCF step, care is needed in incorporating CDFT into existing SCF codes so as to not interfere with these accelerators. DIIS aids convergence by replacing the computed new Fock matrix at a given iteration (of our "outer loop") with a linear combination of it and the Fock matrices from previous iterations. In modifying DIIS to support CDFT, the central principle is that the extrapolation must be consistently done using the Fock matrix which is used to determine the orbital coefficients (that is, the one which includes the constraint potentials); however, a set of historic "core" Fock matrices which do not include the constraints must also be retained for each macroiteration. The DIIS extrapolation coefficients obtained from the constrained Fock matrices are then applied to the historic core Fock matrices to yield an extrapolated core Fock matrix; the microiterations to determine the constraint potentials add a constraint potential to this extrapolated core Fock matrix.

It is important to note that at stationarity, the Lagrangian, W (equation (16)), is equal to the physical energy of the system, E (equation (17)). The energy in the presence of the constraining potentials $V_k w_k$ is then a form of free energy,

$$F = E + V_{\mathrm{tot}} N_{\mathrm{tot}} + V_{\mathrm{spin}} M_{\mathrm{spin}}. \tag{26}$$

In accord with this free energy picture, we obtain the thermodynamic relations

$$\frac{dE(N_k)}{dN_k} = -V_k \qquad \text{and} \qquad \frac{dF(V_k)}{dV_k} = N_k \tag{27}$$

reflecting that E is a natural function of N_k but F is a natural function of V_k. It also follows that $d^2E/dN_k^2 = -(d^2W/dV_k^2)^{-1}$, so that the concavity of $W(V_k)$ implies convexity of $E(N_k)$, an important physical condition.

In addition to energy derivatives with respect to the internal parameters V_i and N_i, we may also wish to compute derivatives of the energy with respect to external parameters such as nuclear position. Such analytical gradients have been implemented for CDFT, making possible *ab initio* molecular dynamics on charge-constrained states and parameterizations of Marcus electron transfer theory therefrom, as will be seen in section 3. Consider the problem of computing the derivative of the electronic energy (equation (17)) with respect to the position of nucleus A. In addition to obeying $E[\rho_{\mathrm{CDFT}}] = W[\rho_{\mathrm{CDFT}}, V_k^{\mathrm{CDFT}}, N_{\mathrm{CDFT}}]$ at convergence, W has the additional property that it is variational with respect to both ρ and the V_i (in contrast to $E[\rho_{\mathrm{CDFT}}]$ which is not even a stationary point of the energy), which allows the use of the Hellmann-Feynman theorem, writing

$$\nabla_A W = \nabla_A E + \sum_i V_i \rho \nabla_A w_i \tag{28}$$

The first term is the standard gradient for unconstrained calculations, which includes the Hellmann-Feynman force, Pulay force, and terms from change in DFT integration grid with nuclear displacement; the second term represents the extra force due to the constraint condition on the density. The form of this term is necessarily dependent on the form of the population operator w used to define the constraint; for the Becke population scheme, these terms have been computed in reference 131. With a Mulliken or Löwdin treatment of population, which depends on the AO overlap matrix, this term has a more complicated form;

reference 38 performs the calculation for the Löwdin scheme. Oberhofer and Blumberger's plane-wave CDFT implementation using Hirshfeld's population scheme has also implemented analytical gradients; their expressions for the weight constraint gradient is in Appendix B of reference 130.

Finally, we note that we have focused here on the implementation of CDFT in localized orbital codes, but the method can equally well be implemented in plane-wave codes.[130] The primary difference is in the cost tradeoff — whereas diagonalization of the KS Hamiltonian is cheap in localized orbitals it is expensive for plane waves. Thus the relative cost of the microiterations is somewhat higher in a plane-wave-based scheme, but the SCF iterations can be significantly faster, particularly for pure functionals applied to condensed phase problems.

2.5 Promolecules

Molecular dynamics follows a system away from the ground-state geometry, and similarly molecular reactions and electronic excited state dynamics sojurn far from the ground-state. In such situations, molecules and molecular fragments come in close contact while they bounce around, jostle, relax, and react. CDFT is designed to construct electronic states of fixed character at arbitrary geometries, even those where fragments overlap, but sometimes it does not perform as well as might be hoped in such close-contact geometries. One of the sorest impediments to its ability to do so is the choice of atomic population prescription. In cases of close approach, the real-space constraint potentials must distinguish between fragments in regions where the density is nonzero, so that assignment of density in that transition region to fragment "A" or fragment "B" is ambiguous, a clear weakness of the available charge prescriptions. The simplest example that shows this ambiguity is H_2^+, with a single electron and two protons. Formally, we can constrain the electron to lie only on one proton ("A"), but when the two protons begin to approach each other, any real-space-based atomic population scheme will begin to assign some fraction of this electron to the

second nucleus ("B"), for any physically reasonable density corresponding to a constrained $H - H^+$ configuration. Thus, the formal charge constraint putting a full electron on atom A is unattainable with present charge prescriptions, and the numerical value of the constraint must be adjusted to accommodate their failings.

This failure of formal charge/spin constraint values extends to the case of arbitrary fragments, coming into play when constrained molecular fragments come in close approach, as in nucleophilic substitution reactions; the promolecule formalism was pioneered to allow CDFT to be used in precisely these types of situations. The sequence of steps involved in the promolecule formalism is a bit complex and probably best understood using an example. Take the typical S_N2 reaction:

$$ClCH_3 + F^- \leftrightarrow \left\{[Cl - CH_3 - F]^-\right\} \leftrightarrow Cl^- + CH_3F$$

for which the natural reactant and product configurations are $ClCH_3(N = 0, S = 0) + F(N = 1, S = 0)$ and $Cl(N = 1, S = 0) + CH_3F(N = 0, S = 0)$ respectively. These formal charge and spin values are exactly valid at infinite fragment separation; however, at small separation there will be overlap between the fragments, and the reported charge and spin will deviate from their formal values. The overlap is strongest at the reaction transition state, and the formal charges and spins simply do not represent realistic constraint values for any population scheme at that closest approach. The promolecule treatment corrects for these errors by modifying the formal integer charge (spin) constraints into values that are appropriate for a given charge prescription. The basic steps involved are illustrated in Figure 4.

The first step in the calculation is to break the system into the appropriate fragments — e.g. F^- and CH_3Cl for the reactant configuration — maintaining the internal geometry of each fragment (Figure 4a). One then performs separate calculations on each fragment with the relevant total charge and total spin (Figure 4b). These converged fragment densities

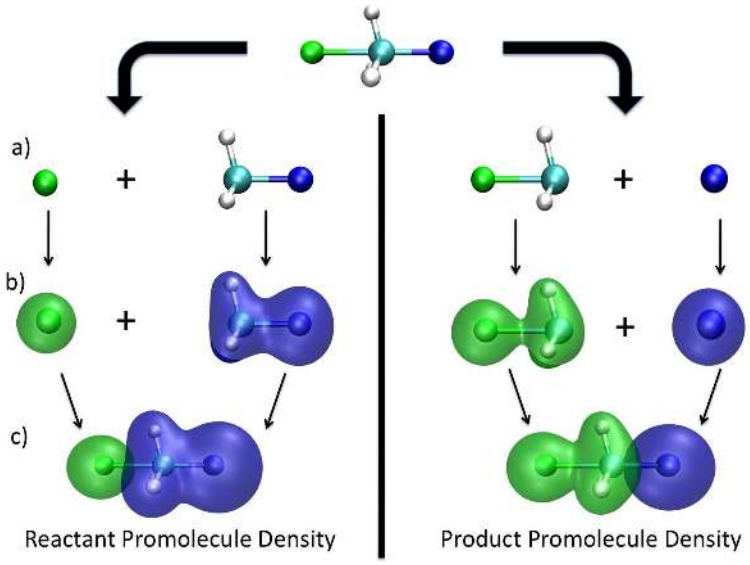

Figure 4: Construction of reactant and product promolecule densities for $[F \cdots CH_3 \cdots Cl]^-$. (a) The system is divided into fragments, with atoms being apportioned to the fragments corresponding to reactant (product) and the internal fragment geometry held fixed at the transition-state values. (b) The ground-state density of the isolated reactant (product) fragments is determined. (c) The fragment densities are superimposed to form the reactant (product) promolecule density. Used with permission from reference 132.

are the fragment promolecule densities — they approximate what an F^- or CH_3Cl density should look like. The fragment promolecule densities are then arranged in the original moelcular geometry and summed to obtain the total promolecule density, $\tilde{\rho}$ (Figure 4c). For the example S_N2 system in the reactant configuration, we obtain

$$\tilde{\rho}_r^\sigma(\mathbf{r}) = \rho_{\mathrm{ClCH_3}}^\sigma(\mathbf{r}) + \rho_{\mathrm{F^-}}^\sigma(\mathbf{r}) \qquad (\sigma = \alpha \text{ or } \beta) \tag{29}$$

With this full promolecule density $\tilde{\rho}(\mathbf{r})$, the actual constraint values used for the final reactant CDFT calculation are

$$N_{\mathrm{tot}} = \int w(\mathbf{r}) \left[\tilde{\rho}_r^\alpha(\mathbf{r}) + \tilde{\rho}_r^\beta(\mathbf{r})\right] d\mathbf{r} \tag{30}$$

$$M_{\mathrm{spin}} = \int w(\mathbf{r}) \left[\tilde{\rho}_r^\alpha(\mathbf{r}) - \tilde{\rho}_r^\beta(\mathbf{r})\right] d\mathbf{r} \tag{31}$$

as depicted in Figure 5. These modified constraint values reflect the expectation that a molecule constrained to be in the "reactant state" should, *within the limits of the charge prescription in use*, look as much as possible like the superposition of the reactants brought from infinite separation to the geometry in question. In many cases, the correction from the promolecule density is small and can safely be omitted, particularly when the constrained regions are on different molecules (as for charge transfer in organic semiconductors, section 5.6) or widely separated (as for molecular sensors, section 3.5). In other cases, though, the correction is essential, as for the very small fragments illustrated in Figure 1, or for reaction transition states that enter into CDFT-CI barrier height calculations (section 6.3). As the fragments come from being well-separated into closer approach, the effect of the correction grows smoothly, owing to the continuity of all functions involved. By the time the reacting fragments reach the transition-state geometry, the correction can be larger than half an electron! Nonetheless, the constraining potentials continue to enforce a consistent physical

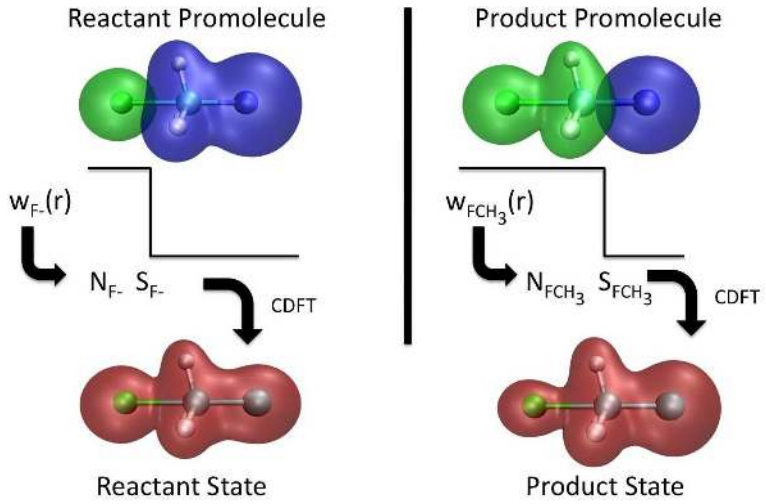

Figure 5: Computation of reactant- and product-like states for $[\mathrm{F}\cdots\mathrm{CH_3}\cdots\mathrm{Cl}]^-$. The total promolecule density is integrated against the charge prescription function $w(\mathbf{r})$ of the reactant (product) fragment to obtain target constraint values. CDFT calculations with these updated constraints produce the final reactant and product states. Used with permission from reference 132.

picture throughout the entire reaction, and allow higher-level methods to be built atop that picture.

2.6 Illustrations

In order to be concrete about how CDFT is used in practice, we now review two of the early applications of CDFT that opened the door to its vast utility: impurities in metals and long-range charge-transfer systems.

2.6.1 Metal Impurities

In bulk systems, a localized hole can be formed where the ejected electron does not localize to a particular site, instead being absorbed into the band structure. In such bulk systems, impurities tend to drive localization phenomena, and in fact the first published results using CDFT were for cerium impurities in silver and palladium. Palladium and silver are transition

metals, whereas cerium is a rare earth; as such, the most noticable distinction is the presence of the cerium f orbtials, which is where we focus our interest. The f orbitals of rare earths are generally decoupled from the overall band structure of the bulk, and thus they are vital for these localization phenomena. One therefore focuses on controlling the f population of the impurity atom while leaving the overall band structure unchanged (except for its local screening response). The energy response to such a site population change, $\Delta E(\Delta N_f)$, measures how a charged impurity affects the local environment of a bulk system. In order to induce such a population change, a constraining potential is applied; since the desired population change is only in the f orbitals of the cerium impurity, the functional form of equation (2) is appropriate. Applying a fixed extra potential V_f to the f orbitals gives a constrained state with a deviation in f population ΔN_f and in energy $\Delta E(\Delta N_f)$, as illustrated in Figure 6. The figure makes it clear that it is easier to add or remove charge from cerium in silver than in palladium — that is to say, cerium more easily traps electrons in silver than in palladium. Further, while $\Delta E(\Delta N_f)$ is very nearly symmetric for silver, it is noticeably asymmetric for palladium, indicating that cerium more readily traps electrons than holes in palladium.

Contemporary theoretical studies of cerium impurities postulated the existence of *two* stationary solutions for the $4f$ wavefunction, the canonical one and an additional one with a maximum outside the $5sp$ shell;[133,134] the existence of these states can be probed with CDFT. Consider adding to the energy a Lagrange multiplier term of the form

$$V\left[\int |r|^2 \rho_f(\mathbf{r}) d^3r - \langle r^2 \rangle \int \rho_f(\mathbf{r}) d^3r\right] \tag{32}$$

where $\langle r^2 \rangle$ is the target value that reflects the "size" of the f orbitals. When V is negative, the resulting potential will be monotonically decreasing (for $r > 0$), repulsive for $r^2 < \langle r^2 \rangle$, and attractive for $r^2 > \langle r^2 \rangle$, pushing electron density outwards from the nucleus. Now,

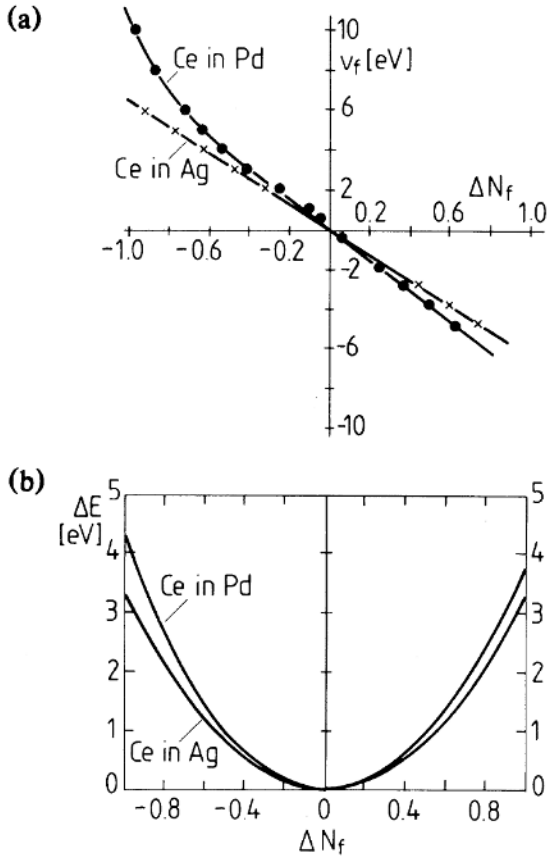

Figure 6: (a) The strength V_f of the constraint potential as a function of the enforced number of f electrons on a cerium impurity in palladium and silver (semirelativistic calculation). (b) The change in energy as a function of ΔN_f for the same systems.

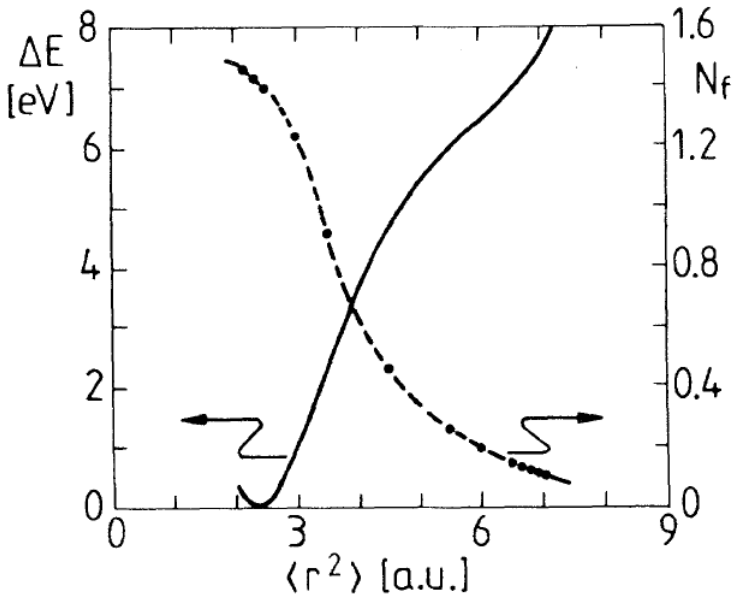

Figure 7: Energy change (left scale) and f occupation (right scale) as a function of the second moment of the f charge density for cerium in palladium (nonrelativistic calculation).

given the modern scheme, we could apply *both* the charge constraint and the size constraint to explore the $4f/5sp$ transition. But in the original studies, only the size constraint was applied, resulting in the $\Delta E(\langle r^2 \rangle)$ and $N_f(\langle r^2 \rangle)$ curves in Figure 7. Clearly, only a single minimum is found, suggesting that there is only one solution, which corresponds to the $4f$ state being inside the $5sp$ shell. Indeed, as $\langle r^2 \rangle$ is increased, N_f falls off sharply, indicating that it is more favorable to promote f electrons to the conduction band than have them extend past the $5sp$ shell.

Note that all of these early studies on impurities used the approach of scanning over V in order to qualitatively study charges and orbital sizes. At least in part, this is because the inverse problem of solving for V given a target value of N is more difficult to solve. More recently, it has become possible (cf Section 2.4) to directly solve for the precise value of V required to attain, for example, unit charge or unit spin transfer. These technical advances have thus opened up the possibility of studying long range charge-transfer, where quantization of charge allows CDFT to make quantitative predictions about excited states.

2.6.2 Long-range Charge-Transfer Excited States

As a representative application, consider the zincbacteriochlorin-bacteriochlorin (ZnBC-BC) complex, an important model system for how charge transfer (CT) states are formed and used to ferry electrons in the photosynthetic process of bacteria.[45,135] In one of the more spectacular failures of LR-TDDFT, commonly used functionals fail to yield reasonable energies for these CT states, giving excitation energies which are too small by >1eV and unphysically flat as a function of site-site separation. These limitations have motivated the development of range-separated hybrid functionals capable of describing long-range CT while maintaining a good description of short-range bonding.[136–140]

When considering a more correct treatment of these CT states, we note that the BC moieties are physically extended, with some twenty-four heavy atoms each arranged in a plane. In the biological system, ZnBC and zinc-free BC are combined in a joint complex, and charge-transfer states between the halves of the complex transfer electrons during photosynthesis. Understanding how these CT states behave at different geometries can help illustrate the internal behavior of part of the incredibly complex photosynthetic process. Because the BC moieties are well-separated from each other, it is natural to assign unit charge to each. Furthermore, at large separation, the interaction between BCs should be dominated by the $1/R$ Coulomb attraction between the opposing charges. To facilitate such distance-dependent studies, a model system with an adjustable-length flexible linker has been created,[45] allowing for calculations ranging from 5.84 Å up to 9.0 Å separation. To perform these calculations, though, the fragment regions must be determined. The BC moiety contains a large number of conjugated π bonds, and thus an extra electron or hole would be expected to delocalize throughout the whole construct. As such, the constraint is applied to the entire (Zn)BC moiety, as opposed to some smaller piece such as half of it, or just the zinc in the ZnBC case. With constraints in hand, the computed energies of $ZnBC^{+}BC^{-}$ and $ZnBC^{-}BC^{+}$ are computed and plotted against $1/R$, showing the expected linear behavior

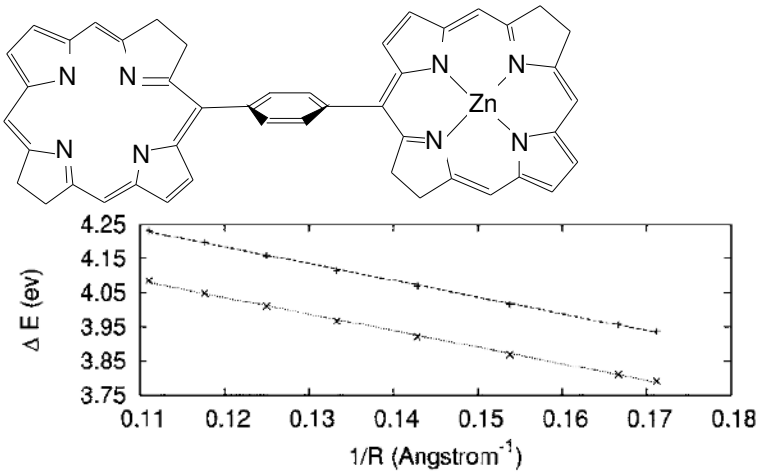

Figure 8: The charge-transfer state energies of ZnBC-BC as compared to its ground-state energy at 5.84 Å separation. Lower line, Zn^+BC^-; upper line, Zn^-BC^+. Used with permission from reference 52.

D	A	$E_D^+ + E_A^-$	$E(\infty)$
N_2	N_2	−218.360411	−218.361386
H_2O	F_2	−275.391972	−275.392850
C_2H_4	C_2F_4	−553.595853	−553.595591

Table 2: Charge-separated state energies extracted to infinite separation and the sum of ionic donor and acceptor energies, in Hartree.

for both species (Figure 8). The excitation energies for the shortest-linker complex (rightmost point) agree nicely with previous reference calculations[45] (3.79 and 3.94 eV versus the accurate values of 3.75 and 3.91 eV, respectively), showing much better agreement than the 1.32 and 1.46 eV excitation energies computed from TDDFT.[52]

Having shown that CDFT charge-transfer states give the correct $1/R$ scaling expected of electron-hole attraction, in order to give a full certification of accuracy, it remains to show that the asymptotic limit of this $1/R$ dependence is correct. The infinite-separation limit $E(\infty)$ is easily obtained by extrapolating $E(1/R)$ to $1/R = 0$. At that limit, donor and acceptor are completely isolated, so the full-system energy $E(\infty)$ should just be the sum of the isolated energies, $E(D^+) + E(A^-)$; Table 2 shows these quantities for three systems. In all three cases the extrapolated energy and sum of noninteracting energies agree to within

1 millihartree, a difference attributable to errors in the point charge approximation at finite separation and fitting errors. In order to get this agreement, unrestricted KS calculations must be used for the constrained calculations to be consistent with the isolated fragment calculations; restricted KS calculations yield correct scaling but an incorrect limit. With both correct scaling and the correct asymptotic limit, CDFT is an excellent tool for studying long-range charge-transfer states.

One can certainly wonder how it is that CDFT is able to describe these states so well, even with semi-local functionals like BLYP, whereas LR-TDDFT fails miserably. There are two insights that illuminate this finding. The first is that, by nature, LR-TDDFT is a *linear* response method, whereas CDFT involves non-linear response of the density (via the self-consistent determination of V and ρ). Thus, whereas TD-BLYP, as a linear response method, misses much of the electron-electron interaction, this interaction is recovered when higher order response is included, as in CDFT. The second insight derives from the fact that CDFT is, at the end of the day, a ground state method. At the asymptotic limit, every CT state separates into the *ground states* of the fragments with the appropriate charge and spin. It is fairly awkward to describe these charged ground states as excited states of the neutral system (as is done in TDDFT), but it is quite natural to describe them as ground states of a different potential (as is done in CDFT). Thus, CDFT is in some sense complimentary to TDDFT: the excited states for which TDDFT works well (valence states) are inaccessible to CDFT, while many of the excited states that are challenging in TDDFT are naturally treated in CDFT.

2.7 Future Challenges

CDFT has been developed as a robust framework for treating charge- and spin-constrained electronic states within the ground-state KS DFT scheme, with computationally feasible implementations that benefit from multiple analytical relations. Early applications revealed

great reliability for long-range charge-transfer states, and gave insights to the behavior of impurities in bulk systems; the following sections will continue on to describe more recent applications of the framework as it has expanded into other realms of application. Looking forward past these existing applications, there remain open areas for expansion. First, while analytic first derivatives of the CDFT energy with respect to nuclear positions are widely available, analytical Hessians have yet to be implemented. These Hessians would, for example, allow for the prediction of IR spectra of charge transfer excited states. Along the lines of using CDFT to correct commonly used functionals, the prospect of applying density constraints *within* TDDFT is tantalizing. For example, applying constraints on the charges of two fragments and maintaining those constraints through linear response would result in the prediction of TDDFT excited states that involve no charge transfer between the two states. That is to say, it would be an excitation spectrum that contained only neutral valence excitations. As TDDFT is typically quite good for valence excitations, this might be a good tactic if one wants to "clean up" a TDDFT spectrum that has been contaminated by unphysically low CT states. Finally, the question of the best underlying population prescription for use in CDFT is also open: though real-space schemes are preferred (over orbital-based methods such as Löwdin), there are still any number of such prescriptions available in the literature (e.g. Becke, Hirshfeld, Bader, Partition Theory...) Many of these have not even been explored in the context of CDFT. Could one population scheme significantly expand the applicability of CDFT? Indeed, how can we quantify when one real-space scheme is "better" than the others? Thus, while CDFT in its present state is a useful tool for applications, there are still a number of directions to be explored both in terms of the fundamentals of the method (how do constraints interact with the charge definition?) and extending its practical utility (e.g. by implementing Hessians).

3 Application to Electron Transfer

3.1 Background: Marcus Theory

Electron transfer (ET) lies at the heart of chemical reactivity, as captured by the "arrow-pushing" formalism in organic chemistry textbooks. Intermolecular ET reactions that proceed without bond breaking or bond formation are among the simplest chemical transformations, yet the kinetics of these reactions remain difficult to predict from first principles. ET can also occur within a molecule, from one functional group to another, as a consequence of thermal or photoinduced excitation. The quest for a quantitative understanding of ET kinetics has been ongoing for well over 50 years and continues to gain practical significance as demand for solar energy conversion accelerates.

The standard theoretical framework for ET reactions has been established for quite some time and is referred to as Marcus theory.[141] Several existing reviews detail the physical foundations,[142–144] applications,[143,145,146] and extensions[144,147,148] of Marcus theory, so we provide only a brief summary here. Marcus theory is a classical transition state theory of ET which assumes that the reactant and product electronic states are weakly coupled. Furthermore, Marcus theory assumes that the molecule(s) undergoing ET are surrounded by an environment that responds linearly to the ET event (linear response approximation). In this limit, the free energy profiles of the two ET states can be represented by a pair of crossing parabolas with identical curvature, illustrated in Figure 9.

Two parameters suffice to characterize the relative displacement and curvature of the reactant and product free energy curves: the driving force $-\Delta G$, which constitutes the free energy difference between reactant and product states, and the reorganization energy λ, which quantifies the free energy penalty associated with forcing the reactant into an equilibrium configuration of the product or vice-versa. The Marcus expression for the ET rate is the classical transition-state theoretical rate obtained from the free energy profiles in

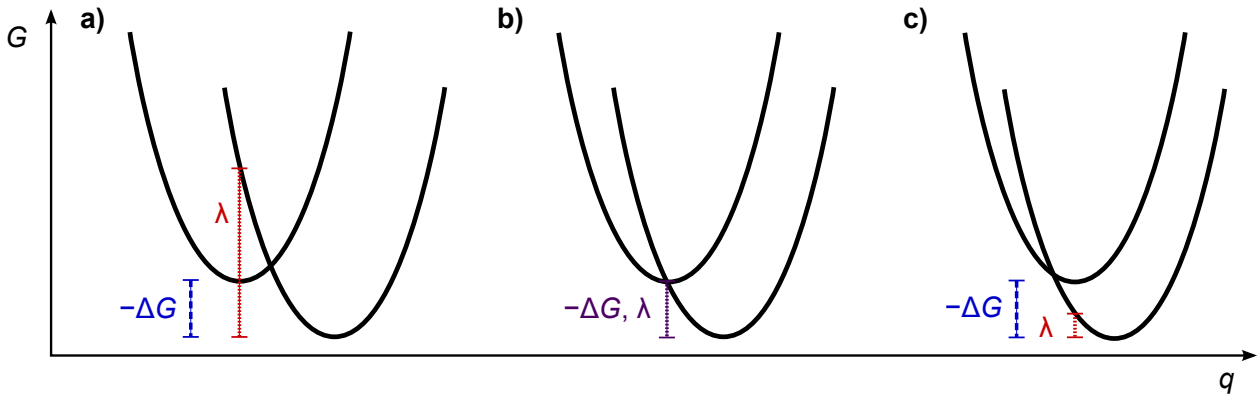

Figure 9: Marcus parabolas depicting free energy as a function of an ET reaction coordinate in different regimes. (a) The normal region,$-\Delta G < \lambda$. (b) The top region, $-\Delta G \approx \lambda$. (c) The inverted region, $-\Delta G > \lambda$.

Figure 9,

$$k_{\mathrm{ET}} = \frac{2\pi}{\hbar} \frac{|H_{ab}|^2}{\sqrt{4\pi\lambda k_{\mathrm{B}} T}} \exp\left[-\frac{(\lambda + \Delta G)^2}{4\lambda k_{\mathrm{B}} T}\right] \tag{33}$$

Here T is the temperature, k_{B} is the Boltzmann constant, $\hbar$ is the reduced Planck constant, and the pre-exponential factor is expressed in terms of thermodynamic quantities plus an electronic coupling term H_{ab} which will be considered in detail in section 5. According to eq 33, the ET activation energy $\Delta G^{\ddagger}$ is given by

$$\Delta G^{\ddagger} = \frac{(\lambda + \Delta G)^2}{4\lambda} \tag{34}$$

ET reactions are classified according to the relative magnitudes of $-\Delta G$ and λ. Reactions satisfying $-\Delta G < \lambda$ are said to occur in the "normal" regime, while those in the Marcus "inverted" regime satisfy $-\Delta G > \lambda$. Representative free energy curves for these two cases are shown in Figures 9a and 9c. In the intermediate "top" region of Figure 9b, a negligible activation free energy barrier results in the maximum ET rate for a given driving force. In the inverted regime, the Marcus theory predicts a decrease of the ET rate with increasing driving force; experimental evidence of Marcus inverted effects[149] has reinforced the value of the theory.

Given the demonstrated utility of the Marcus model, methods to predict Marcus ET parameters for real systems from first principles have proliferated in recent years. These predictions are challenging because they call for a *diabatic* representation of the ET states, whereas conventional electronic structure methods produce adiabatic states. In the adiabatic representation, one of the ET states is often an excited state. It is possible to estimate the driving force in the adiabatic representation from the energy difference of the ground and excited states at their respective equilibrium geometries, but this calculation requires optimization of the excited state geometry, which hampers its applicability to larger systems.

The reorganization energy λ presents further challenges to computation. It is fundamentally a nonequilibrium property because it requires the energy of one ET state at the equilibrium geometry of the other state.[150] The reorganization energy is often partitioned into two contributions: an inner-sphere reorganization energy associated with distortion of the molecular geometry and an outer-sphere reorganization energy reflecting the rearrangement of solvent to accommodate the new charge distribution. The outer-sphere reorganization energy often comprises the dominant contribution to the total λ,[151,152] so a proper description of solvent effects is crucial.

Still, significant progress has been made towards prediction of reorganization energies. A straightforward and popular approach is the four-point method,[153] which treats reorganization of the donor to its radical cation and of the acceptor to its radical anion independently. This approach can be used with high-level electronic structure methods but does not account for interactions between donor and acceptor, which cannot be neglected for intramolecular ET. Alternatively, one can employ a diabatization scheme[154] to compute energies for the two ET states at either state's equilibrium geometry. Adiabatic-to-diabatic transformations such as the generalized Mulliken-Hush approach[155] can be used for this purpose, or one can directly construct approximate diabats using tools such as empirical valence-bond methods,[156] frozen DFT,[157] or (as discussed below) using CDFT.

In this section we highlight applications of CDFT to the construction of diabatic ET states and to the computation of driving forces and reorganization energies. Special attention is given to techniques for incorporating solvent effects and to the pairing of CDFT with molecular dynamics (MD) simulations to obtain ET free energy profiles without direct invocation of the Marcus model.

3.2 Diabatic ET States from CDFT

3.2.1 Choosing Suitable Density Constraints for ET

CDFT can be used to construct diabatic states for any ET reaction whose electron donor and acceptor moieties are known in advance. Example systems include metal ions undergoing self-exchange in solution,[130,158] charge-transfer states in extended molecules,[53,159] and donor-acceptor interfaces in organic semiconductors.[160] In ET systems with a neutral ground state, the frontier orbitals of the ground and CT states are of the general form illustrated in Figure 10. In the ground state, both the donor and acceptor have closed shells. The transfer of one electron from the donor HOMO to the acceptor LUMO defines the CT state. Considered as isolated species, the donor and acceptor are both charged radicals after ET; hence the CT state is also commonly dubbed a radical ion-pair state.

To obtain diabatic ET states from CDFT, one first defines which regions of the system are to be associated with the donor or with the acceptor. Then, net charges (or a net charge difference) are assigned to the donor and acceptor in accordance with the character of the target state, as outlined in section 2. For example, to define the CT diabatic state in Figure 10, one may constrain the donor (acceptor) to have one fewer (more) electron than it would possess as an isolated, neutral system. A diabatic representation of the neutral ground state is obtained by constraining the net charges on the donor and acceptor to zero. In practice, the constrained neutral state usually differs negligibly from the adiabatic ground state, so a

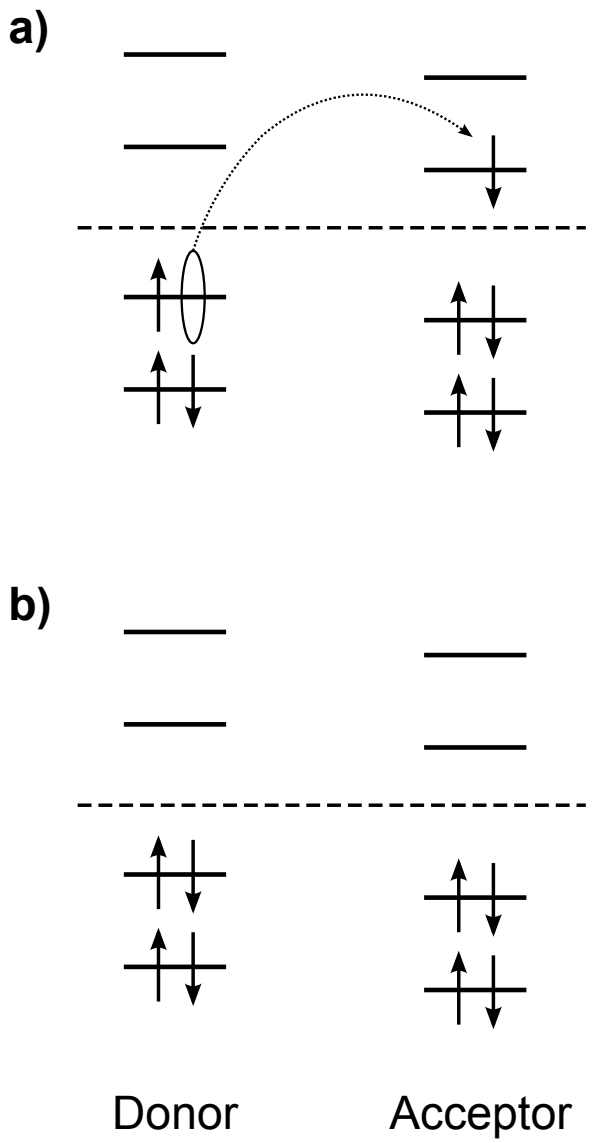

Figure 10: Frontier orbitals for the CT excited state (a) and the ground state (b) involved in ET reactions. Adapted with permission from ref 53.

ground state calculation can often suffice for this purpose.

As discussed in section 2, constraint regions are typically defined in terms of atomic populations such as the Mulliken,[125] Löwdin,[126] Becke[117] or Hirshfeld[118] populations. However, simpler constraining potentials have also proven useful in some related methods for studying charge transfer. One important example is provided by the perturbed ground state (PGS) method,[161] a constrained-state approach to ET in which perturbing potentials are used to explore how the strength of the perturbation affects the splitting between the two lowest-energy states. The diabatic energies and the electronic coupling can both be deduced from the PGS procedure, although the requirement to scan over the constraining potential makes the method more computationally expensive than CDFT. In these studies, spherical well potentials centered on the donor and acceptor and possessing opposite signs provided states of sufficiently diabatic character to extract diabatic energies and couplings for hole transfer in He^{2+} and in a simplified model of a peptide bond.[161]

3.2.2 Illustrations

The diabatic ET states of a diverse and growing number of systems have been determined from CDFT calculations. Long-range CT-state energies of model systems such as the N_2 dimer and stretched ethylene-tetrafluoroethylene obtained from CDFT match the sum of the energies of the isolated radical ions.[53] This correspondence confirms the expectation that the CDFT approach to CT states mitigates the effects of self-interaction error. The proper $1/R$ depenence of the CT state energy on donor-acceptor distance R was also verified in the zincbacteriochlorin-bacteriochlorin complex,[52] where TDDFT obtains an incorrect scaling.[45]

To understand the structural consequences of ET, it is instructive to consider the dependence of the diabatic energies on nuclear configuration. CDFT was used to construct diabatic states for proton-coupled ET across a hydrogen-bonded bridge in a model bipyridine-dinitrobenzene complex[53] (Figure 11a). In this study, the position of a proton along the

hydrogen-bonded bridge was varied from one side of the bridge to the other, and the diabatic energies were computed as a function of this proton coordinate. A +0.3 a.u. point charge was affixed to the bipyridine of the donor to model the effect of a Ru center in the real system. As shown in Figure 11b, two minima were found along the reaction coordinate, corresponding to localization of electron density on either the donor or the acceptor. The predicted reaction barrier height, 7 kcal/mol, is significantly lower than the 25 kcal/mol barrier height predicted by a multiconfiguration SCF (MCSCF) calculation.[162] The MCSCF calculation, however, is essentially free of the dynamical correlation effects captured by any DFT approach. Thus, much of the difference between barrier heights predicted by MCSCF and CDFT can be attributed to dynamical correlation.

ET in mixed-valence compounds represents another challenge for DFT, particularly in compounds defined as Class II within the Robin-Day classification scheme.[163] The Class II compounds possess two charge centers with different formal oxidation states, and ET takes place intermittently between the two charge centers. The two formal oxidation state pairs are diabatic states and are thus amenable to a CDFT treatment. A recent example is provided by the characterization of the mixed-valence Fe(II)−Fe(III) complex $\{Cp^*(dppe)Fe(C{\equiv}C-)\}_2(1,3\text{-}C_6H_4)$ (Figure 12c), which was reported from experiments to exhibit charge-localized states on the Au(111) surface[164] (dppe = 1,2-bis(diphenylphosphino)ethane).

Scanning tunneling microscopy (STM) of the mixed-valence complex, shown in Figure 12a, presented one bright and one dim region on each molecule, in agreement with CDFT-simulated STM images of the molecule in Figure 12b.[164] Given the enforced diabaticity of the charge-localized CDFT states, the qualitative agreement between the simulated and measured STM images provides strong evidence that charge localization is the correct interpretation of the STM experiments on this Fe(II)−Fe(III) compound on Au(111). This feature could make such compounds useful as components in solid-state molecular electronics.

The availability of analytic gradients for CDFT states enables fast geometry optimiza-

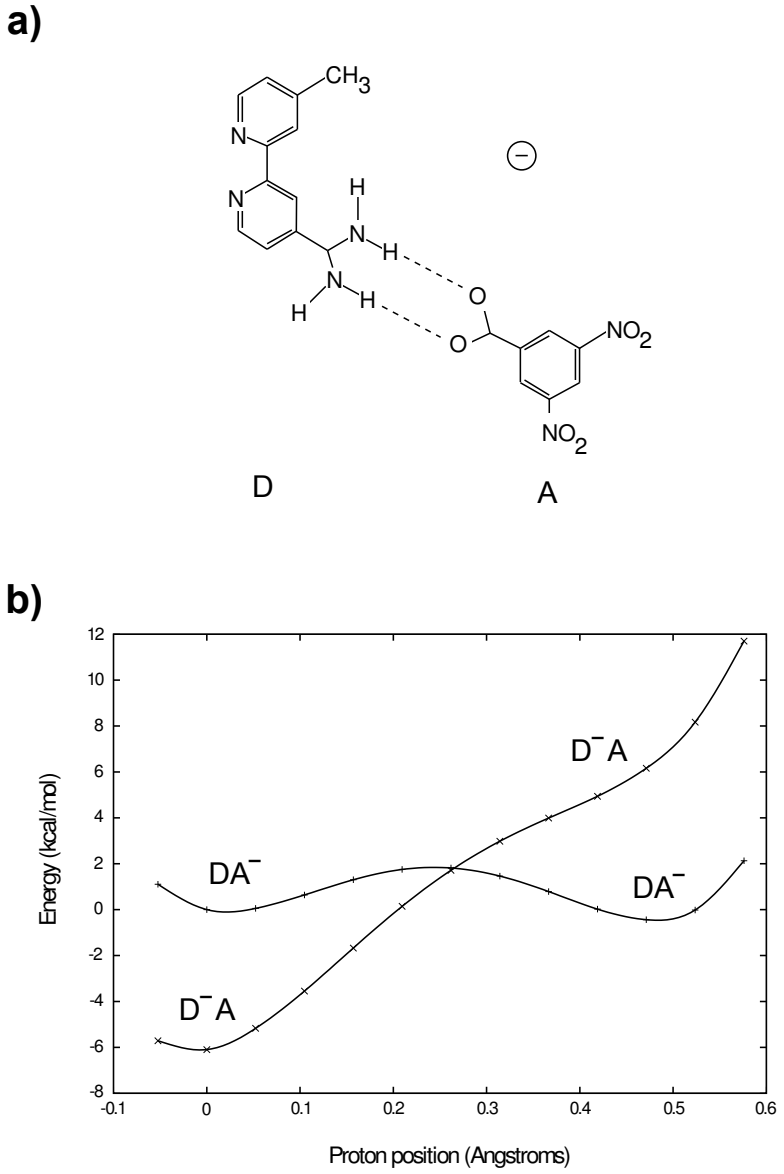

Figure 11: (a) Model hydrogen-bonded DA system for proton-coupled ET. (b) Energy profiles of D^-A and DA^- states along a linear proton transfer coordinate. Adapted with permission from reference 53.

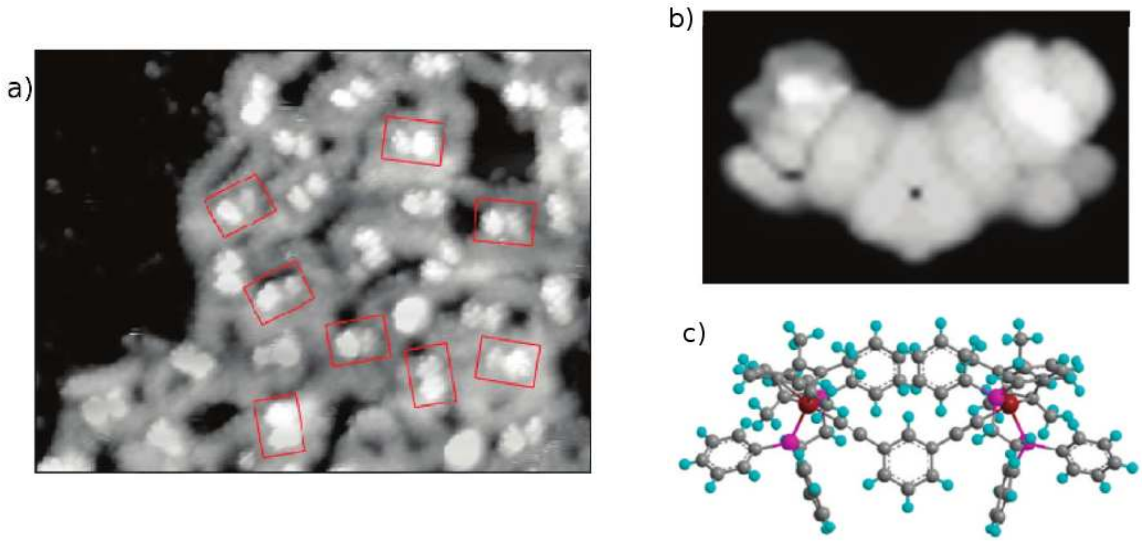

Figure 12: (a) Experimental and (b) simulated STM images of a mixed valence diiron complex, along with (c) the ground state geometry of the Fe(II)−Fe(III) mixed-valence compound. The difference in brightness between the two sides of the compound in the STM images is indicative of charge localization.

tions for diabatic states,[38] a prerequisite for computation of the inner-sphere reorganization energy. The optimized geometry of the charge-localized states in a mixed-valence compound can differ significantly from that of the delocalized state provided by a conventional DFT calculation, as illustrated by the mixed-valence tetrathiafulvalene-diquinone anion [Q-TTF-Q]$^{-}$. Full geometry optimizations on the charge-constrained Q^{-}-TTF-Q, with the excess electron confined to one side of the molecule, produce C−C bond lengths differing by several pm relative to the unconstrained DFT geometry of the [Q-TTF-Q]$^{-}$ anion, shown in Table 3. For clarity, we emphasize that geometry optimization of the constrained state is not constrained in the conventional sense of applying constraints to chosen nuclear degrees of freedom; the only constraint in the optimization is the density constraint self-consistently applied within the electronic Hamiltonian at each step of the optimization.

In the charge-localized state, the geometry of the quinone bearing the excess electron resembles the bare quinone anion, whereas the geometry of the neutral quinone side re-

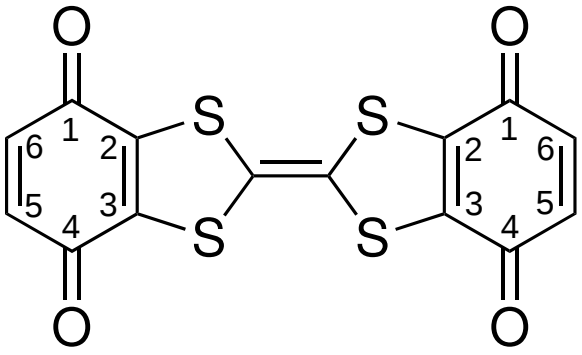

Figure 13: The mixed-valence Q-TTF-Q anion. The quinone ring-numbering shown here is used to describe bond lengths in Table 3.

	Q-TTF-Q$^-$			Q-TTF-Q	Q	Q$^-$
	DFT	C-neutral	C-reduced			
O-C1	1.246	1.226	1.268	1.226	1.227	1.273
C1-C2	1.464	1.481	1.450	1.481	1.487	1.452
C2-C3	1.370	1.359	1.378	1.359	1.345	1.375
C1-C6	1.470	1.491	1.450	1.489	1.487	1.452
C5-C6	1.358	1.342	1.376	1.343	1.345	1.375
α	168.5	171.4	160.2	166.7		

Table 3: Geometries of the quinone groups in Q-TTF-Q$^-$ and Q-TTF-Q, obtained by conventional (DFT) and constrained (C) calculations, with geometries of an isolated neutral (Q) and anionic (Q$^-$) 1,4-benzoquinone molecule. Reproduced with permission from reference 38.

sembles that of the neutral quinone molecule. From these calculations, the inner-sphere reorganization energy of [Q-TTF-Q]$^-$ is obtained as

$$\lambda_i = E(\text{Q}^-\text{-TTF-Q}|\text{Q-TTF-Q}^-) - E(\text{Q-TTF-Q}^-|\text{Q-TTF-Q}^-)$$

where $E(\text{A}|\text{B})$ represents the energy of state A at the optimized geometry of state B. Here, the computed $\lambda_i = 13.08$ kcal/mol corresponds to slightly more than half of the estimated total reorganization energy $\lambda = 22$ kcal/mol of [Q-TTF-Q]$^-$ in a 10:1 ethyl acetate/*t*-butyl alcohol solution.[165]

In polar environments, the outer-sphere reorganization energy is often the dominant contribution to the total reorganization energy. The ET driving force can also be significantly modified by the environment, especially in polar solvents which preferentially stabilize CT states. Next we consider methods to account for the influence of the environment on CDFT energies and structures.

3.3 Incorporating Solvent Effects

The role of the environment in modulating ET properties is an essential feature of Marcus theory.[141] Figure 14 provides a schematic for nonadiabatic ET in polar media. Solvent polarization, on average, acts to stabilize an electron localized on an electron donor. However, thermal fluctuations of the solvent can bring the two diabatic states into a transient energetic degeneracy, at which point the electron can hop to the acceptor with probability proportional to the square of the electronic coupling.

At first glance, the mechanism illustrated in Figure 14 appears well-suited for a dielectric continuum model of the solvent.[166,167] In the continuum models, the solute is placed in a cavity carved out of a continuous dielectric medium characterized by its dielectric constant ϵ, and the solvation free energy is obtained by solving the Poisson-Boltzmann equation for the

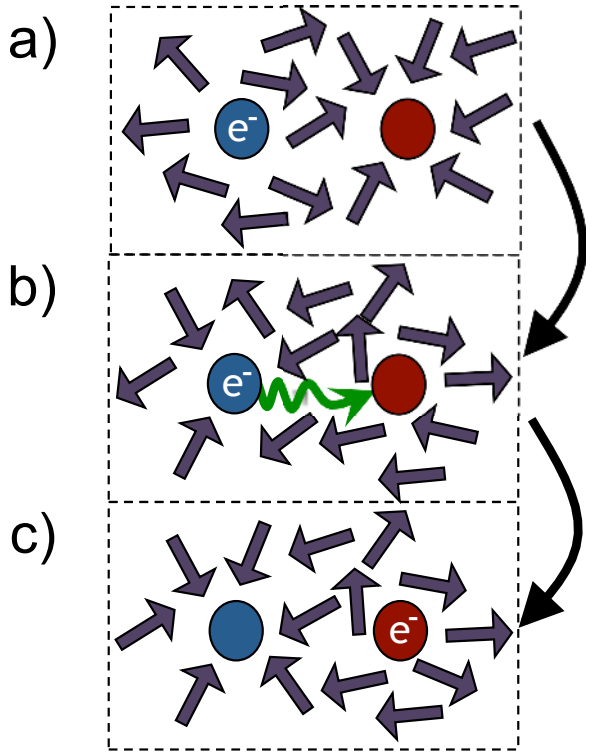

Figure 14: Schematic of solvent reorganization accompanying ET. Reproduced with permission from reference 154.

surface charge on the cavity induced by the dielectric response of the solvent to the solute electron density. These continuum models typically make the approximation that the solvent can be characterized by a frequency-independent dielectric constant ϵ. This approximation is often quite good for ground-state solvation energies, especially in solvents lacking significant nonelectrostatic interactions, e.g. hydrogen bonding or π-stacking.

However, the approximation of a single dielectric constant breaks down in immediately after electronic excitation of the solute, especially for CT states. The underlying reason is that vertically excited states are out of equilibrium: the solvent electron density equilibrates with the CT density of the solute, but the larger mass of the solvent nuclei causes orientational polarization to take place on a slower timescale. Immediately after electronic excitation, the solvent nuclear degrees of freedom remain in equilibrium with the ground state of the solute. Rather than introduce a fully frequency-dependent dielectric $\epsilon(\omega)$ to model this behavior, it is convenient and practical to separate the solvent polarization response into fast and slow components in accordance with solvent electronic and nuclear relaxation.[168,169] Electronic response is characterized by the optical dielectric constant ϵ_∞, which is the square of the refractive index of the dielectric, while nuclear response is characterized by the zero-frequency dielectric constant ϵ_0.

The ability of CDFT + implicit solvent to provide ET driving forces and reorganization energies was assessed for the small donor-acceptor dyad formanilide-anthraquinone (FAAQ) in DMSO solution[38] using the COSMO continuum solvent model.[170] The predicted driving force $-\Delta G = 2.31$ eV is in reasonable agreement with electrochemical studies which provide estimates $-\Delta G = 2.24 - 2.68$ eV.[171,172] These electrochemical estimates of $-\Delta G$ probe the one-electron reduced and one-electron oxidized states of FAAQ rather than directly probing the zwitterionic CT state; unfortunately, a direct assessment of the driving force through an experimental CT state energy is unavailable due to the state's small oscillator strength.

The total reorganization energy of FAAQ obtained from CDFT calculations with COSMO

solvent is $\lambda = 0.6$ eV, which amounts to less than half of the experimentally inferred $\lambda = 1.4 - 1.8$ eV. The experimental estimate of λ was obtained within the linear response approximation by comparison of CT state lifetimes of FAAQ and its ferrocenated derivative FcFAAQ.[171,172] There are several viable reasons for the discrepancy between the CDFT/COSMO and experimental λ, including an inadequate theoretical characterization of the nonequilibrium state and the lack of configurational sampling of low-energy solute conformers. In the following section, we will consider how explicit solvent models can be used to address these and other shortcomings.

3.4 Molecular Dynamics and Free Energy Simulations

By including an explicit description of the solvent in the calculation of ET parameters, one no longer needs to rely on assumptions such as linear response to attain a tractable model of solvent effects; instead, one may sample the configuration space of the system through Monte Carlo or molecular dynamics (MD) simulations to obtain a statistical description of the ET energetics. However, the introduction of so many solvent degrees of freedom can obscure the notion of an ET reaction coordinate describing collective solvent motions.

An elegant solution to this problem is to choose the energy gap ΔE between the diabatic states as a reaction coordinate;[173] this choice of reaction coordinate condenses all important solvent motions onto a single quantity in which the free energy is quadratic in the limit of linear response.[174] Using the energy gap as the ET reaction coordinate, a standard protocol for the simulation of ET free energies in explicit solvent has emerged.[173,175–177] The procedure is illustrated in Figure 15: first one runs long MD trajectories on one or both diabatic states and samples ΔE along these trajectories (Figure 15a). Then a probability distribution for the energy gap, $P(\Delta E)$ is obtained by fitting the sampled energy gaps to a pre-determined distribution, most often a Gaussian. (Figure 15b). Finally, free energy profiles along the energy gap reaction coordinate are computed through the relation $P(\Delta E) = -k_{\mathrm{B}}T \ln G(\Delta E)$.

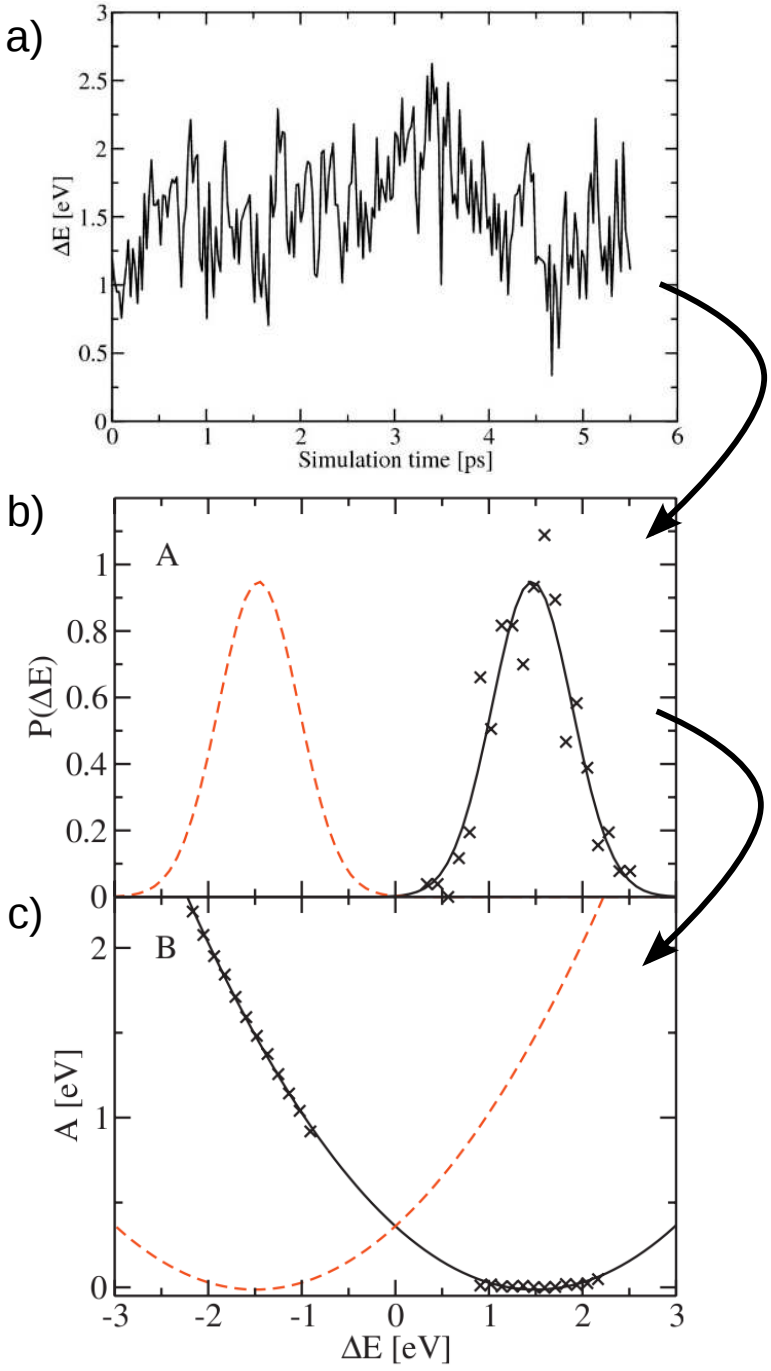

Figure 15: Simulation of ET free energy profiles in explicit solvent: (a) tracing the energy gap along MD trajectories, (b) fitting the energy gap statistics to construct a probability distribution for the energy gap, and (c) producing ET free energy curves from the temperature-scaled logarithm of the probability distributions. Reproduced with permission from reference 130.

CDFT has recently become a popular choice for obtaining diabatic states for ET simulations in explicit solvent. Marzari and co-workers studied self-exchange in the aqueous $Fe^{2+}-Fe^{3+}$ dimer using a penalty function approach to CDFT on the full aqueous system.[158] In this study, ET parameters were first obtained with the PBE functional in the limit of infinite separation of the two ions, where a constrained approach is not necessary. Instead, it is possible to run MD on just one of the ions with the total system charge fixed at $(3-r)$, where $r \in [0,1]$ serves as an umbrella sampling parameter to obtain equilibrium configurations of the system in oxidation states between +2 and +3. For each pair of sampled configurations, the energy gap was obtained by calculating the energy of one configuration at a total charge +2 and of the other configuration at a total charge +3, and taking the difference. These gaps were fit to a Gaussian with coefficient of determination $R^2 = 0.9996$ and a reorganization energy $\lambda = 1.77$ eV, compared to an experimental value of 2.1 eV at a separation distance of 5.5 Å.

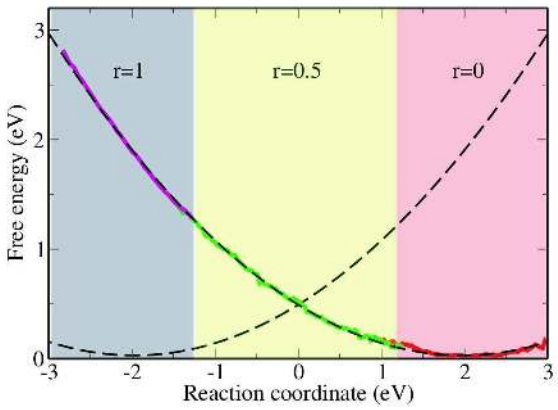

Figure 16: Diabatic free energy surfaces for ET in the aqueous $Fe^{2+}-Fe^{3+}$ system at finite Fe−Fe separation, obtained using CDFT. The portion of the reaction coordinate sampled using each of three values for the umbrella sampling parameter r is indicated by color. Reproduced with permission from ref 158.

Computational access to the reorganization energy at realizable finite distances is hindered by delocalization of density over both ions, a consequence of the self-interaction error. To overcome the problem, Marzari and co-workers introduced a penalty functional, akin to

CDFT, which was designed to steer the largest eigenvalue of the minority-spin occupation matrix of the Fe^{2+} and Fe^{3+} ions towards the value they attain for isolated $[Fe(H_2O)_6]^{2+}$ and $[Fe(H_2O)_6]^{3+}$, respectively.[158] *Ab initio* MD trajectories for $Fe^{2+}-Fe^{3+}$ in a periodic box of 62 water molecules were obtained with the added penalty functional for a set of fixed charge states $Fe^{(2+r)+}-Fe^{(3-r)+}$. The energy gap probability distribution constructed from this data yield the free energy surfaces shown in Figure 16. The resulting reorganization energy $\lambda = 2.0$ eV is only 0.1 eV below the experimental value. Excellent statistics were achieved using only three values for the umbrella sampling parameter, corresponding to equilibrium configurations of the reactant ($r = 0$) and product ($r = 1$), plus transition-state configurations, ($r = 0.5$).

In addition to the penalty functional approach, the CDFT formalism as outlined in section 2 has also been applied to MD simulation of ET free energies in explicit solvent.[130] Oberhofer and Blumberger implemented CDFT energies and forces with a plane-wave basis and with constraints defined in terms of Hirshfeld weights.[118] They assessed the CDFT-MD approach on a standard model system for ET simulations, the $Ru^{2+}-Ru^{3+}$ self-exchange reaction in water. Various classical MD approaches have obtained a range of values for the reorganization energy in this system, $\lambda = 1.60 - 1.87$ eV, depending on the particular water model employed.[178] CDFT-MD simulations on the aqueous diruthenium system were run with a charge difference constraint $N = 1$ imposed between the two ruthenium hexahydrates. The evolution of the energy gap obtained from such a trajectory is depicted in Figure 15a. Because the system possesses symmetric ET states, it is possible to obtain probability distributions for the energy gap on either diabatic state — and hence, free energy profiles for either state — using energy gaps sampled from only one diabatic state. As for the $Fe^{2+}-Fe^{3+}$ system, the energy gaps can be mapped reasonably well onto a Gaussian, resulting in parabolic free energy profiles possessing a reorganization energy $\lambda = 1.53$ eV. A correction term +0.09 eV was applied to the reorganization energy to account for the exclu-

sion of the outer-shell and bulk water from the constraint region.[178] No direct experimental probe of the reorganization energy is available for comparison to the CDFT-MD estimate $\lambda = 1.62$ eV. However, an estimate $\lambda = 2.0$ eV obtained by applying several assumptions to experimental data[179] suggests that the CDFT-MD approach attains at least a qualitatively correct picture of ET self-exchange between aqueous metal ions at finite separation.

The qualitatively correct reorganization energies obtained in the aqueous self-exchange studies show that an explicit description of the solvent can capture intermolecular interactions that the implicit models miss. However, the increase in computational cost associated with a DFT description of the solvent can be prohibitive for larger systems. Therefore, hybrid QM/MM models — which treat the solute (and possibly some nearby solvent) with DFT or another QM method while using an empirical force field to describe the solvent — have become popular in theoretical simulations of complex systems,[180] including ET systems.[177] It is straightforward to construct diabatic states from CDFT in the context of a QM/MM model, provided one makes the common approximation that no charge is transferred between the QM and MM subsystems. Then, the standard machinery of electronically embedded QM/MM can be used without modification for density-constrained QM/MM simulations.

A CDFT/MM approach was recently used to compute ET free energy profiles for charge recombination in the FAAQ dyad introduced in section 3.3. In this study, polarizability of the DMSO environment was incorporated through reparameterization of an existing force field[181] to confer isotropic polarizabilities on the heavy atoms using a charge-on-spring model.[182] Equilibrium configurations of each diabatic state were sampled from CB3LYP/MM MD simulations and used to construct probability distributions that presented a greater degree of skewness than was observed in the self-exchange studies.[183] Making the linear response approximation, the free energy profiles are Marcus parabolas with equal curvature, and the reorganization energy obtained from the simulations is $\lambda = 1.64$ eV, within the range

$\lambda = 1.4 - 1.8$ eV inferred from experiment. The ET parameters obtained from this study are shown in Table 4.

Basis set	$\langle \Delta E \rangle_{\mathrm{N}}$	$\langle \Delta E \rangle_{\mathrm{CT}}$	λ	$-\Delta G_{\mathrm{CR}}$	$\Delta G^{\ddagger}_{\mathrm{CR}}$
3-21G	4.13	0.86	1.63	2.49	0.11
6-31G*	4.03	0.74	1.64	2.38	0.08

Table 4: ET parameters for FAAQ in DMSO obtained from CDFT-MD simulations: average energy gap ΔE in the neutral (N) and charge transfer (CT) diabatic states, reorganization energy λ, driving force $-\Delta G_{\mathrm{CR}}$ and activation free energy $\Delta G^{\ddagger}_{\mathrm{CR}}$. All energies are in eV. Reproduced with permission from reference 183.

In section 3.3, an implicit solvent approach determined $\lambda = 0.6$ eV for the same system. The explicit model clearly reproduces the solute-solvent interactions in the experiment more faithfully than the implicit model, albeit at greatly increased computational expense. The success of the CDFT/MM approach in the case of FAAQ is especially promising because, unlike in the ion self-exchange systems, ET in FAAQ is asymmetric and intramolecular; both of these features should challenge the method, and yet the obtained reorganization energy is quantitatively correct.

3.5 Related and Ongoing Work

The early successes of CDFT for describing ET states, together with the availability of fast implementations of CDFT, are catalyzing a shift from proof-of-principle calculations towards active use in the interpretation of experimental data.

The ability of CDFT to assist in the characterization of mixed-valence compounds was illustrated in section 3.2 by the calculation of charge-localized geometries and by the simulation of STM images of a mixed-valence compound. CDFT can also provide access to the vibrational signatures of charge-localized states. This feature was exploited by Hoekstra and co-workers in the interpretation of Raman spectra of the mixed-valence 4,4′-dinitrotolane radical anion in several solvents.[184] Optical spectra of the compound[185] suggest an equi-

librium between the charge-localized (Class II) structure and the charge-delocalized (Class III) structure, the balance of which depends on the intrinsic reorganization energy λ_s of the solvent. As an alternative test of this hypothesis, Hoekstra and co-workers obtained Raman spectra of the radical anion in solvents with differing λ_s. They then calculated the relevant vibrational frequencies of the geometry-optimized anion in its charge-delocalized and charge-localized states, as obtained by conventional and constrained DFT, respectively. By correlating differences between the gas-phase DFT and CDFT frequencies to spectral shifts, they were able to assign the two sets of peaks in the Raman spectra to the charge-localized and charge-delocalized states. The study provided further evidence that an equilibrium between two charge states exists in solution and depends on the solvent reorganization energy.

In addition to its role in the interpretation of spectroscopic measurements, CDFT is also poised to broaden our understanding of the role of CT states in photophysical and photochemical applications. For example, the relative energies of low-lying localized and CT excited states can control the relative likelihood of radiative or nonradiative relaxation to the ground state after photoexcitation. Taking advantage of this phenomenon, synthetic chemists have designed a panoply of small-molecule sensors whose fluorescence is modulated by the presence of a particular analyte.[186] This switching behavior depends on small changes in the relative energies of a localized excited state and a CT excited state, and thus it presents a challenge for theoretical modeling within the framework of DFT. A recent study of the localized and CT excited states in the zinc sensor Zinpyr-1 (ZP1) used TDDFT and CDFT to characterize the local and CT excited states, respectively, in the absence and in the presence of its Zn^{2+} analyte.[187]

CDFT calculations confirmed that the CT state in ZP1 is energetically inaccessible for fluorescence quenching by photoinduced ET when the sensor is binding two Zn^{2+} ions. The ordering of the excited states in the absence of Zn^{2+} was found to depend strongly on pH, clouding the ability of the approach to provide a complete picture of the photophysics in ZP1.

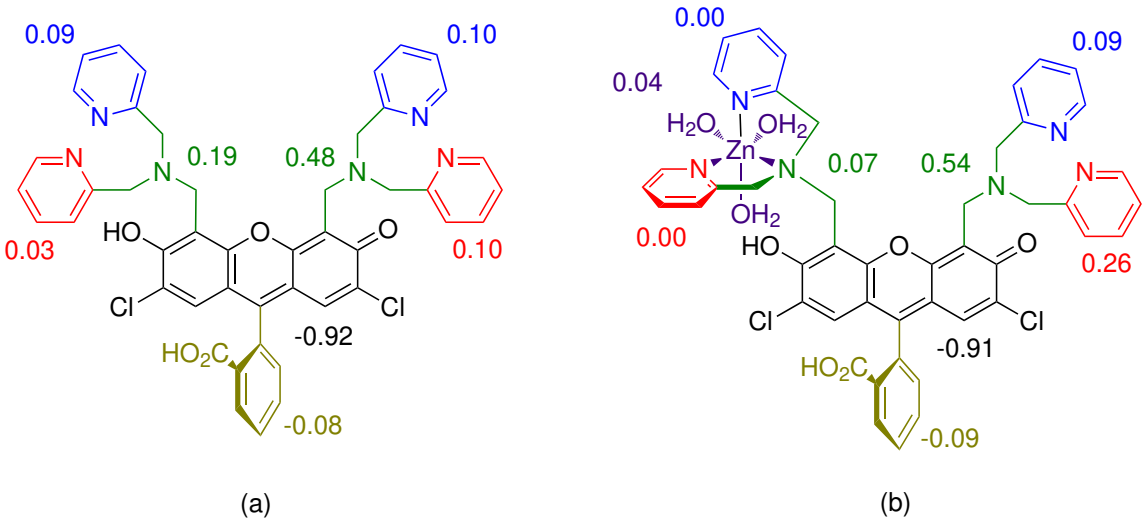

Figure 17: Decomposition of electron density in the CT state of ZP1 by functional group, without and with zinc analyte. Reproduced with permission from reference 187.

Still, the CDFT approach provided supporting evidence for the hypothesis that the electron donor in ZP1 is primarily the amine nitrogen of the dipicolylamine arm, with some minor contribution from the pyridyl nitrogens. This evidence was obtained by decomposing the Becke populations of the constrained CT state over the functional groups of the sensor, shown in Figure 17. Both dipicolylamine arms donate electron density to the central xanthone ring in bare ZP1; however, if one of the arms binds Zn^{2+}, then ET from the corresponding arm is mostly quenched, and the other arm donates a larger fraction electron density to compensate.

Together, the studies highlighted in this section have established that CDFT can parameterize diabatic potential energy surfaces on the fly with an accuracy nearing that of ground-state DFT. This capability should prove valuable for real-time quantum and semiclassical dynamics simulations which trace the evolution of the wavefunction describing the ET system. Together with an explicit solvent model, CDFT calculations can provide access to diabatic states of larger systems in strongly interacting environments. It will be interesting to see how else this efficient scheme for constructing diabatic states might be applied to further our understanding of ET processes.

4 Low-lying Spin States

In systems with unpaired electronic spins, the energy spectrum of available spin states often underlies key physical and chemical properties. These states dictate, for example, the strength of molecular magnets[188] and the coordination chemistry and color of transition metal complexes. Interconversions between spin states can influence the product distributions of photochemical reactions[189] and have direct bearing on the efficiency of charge separation and recombination in organic photovoltaics (OPVs) and organic light-emitting diodes (OLEDs).[190]

The full electronic structure of the system, as embodied in the N-electron wavefunction, often represents a finer level of detail than is required to understand the spin properties of the system. After all, in the ground and low-lying excited states of a molecule, most of the electrons are spin-paired and can therefore contribute only indirectly to spin properties. Instead, it is common practice to adopt a simplified local model of spin in which unpaired electrons are assigned to local sites A, B, ... in accordance with chemical intuition. For example, excess spin may be localized on a radical center in an organic molecule or on a paramagnetic ion in a transition metal complex. The spin states and their energies are then modeled as eigenstates of a Heisenberg Hamiltonian,[191]

$$\hat{H} = -2 \sum_{A<B} J_{AB}\, \hat{\mathbf{S}}_A \cdot \hat{\mathbf{S}}_B. \tag{35}$$

The coefficients J_{AB} are the exchange coupling constants which describe the interaction strength of unpaired spins A and B, and $\hat{\mathbf{S}}_A$ ($\hat{\mathbf{S}}_B$) is the spin operator for the electron at site A (B). Although this model is approximate,[192] it effectively captures the important spin degrees of freedom and enjoys widespread use.

The idea of parameterizing a Heisenberg Hamiltonian using *ab initio* data harkens back to Nesbet[193] and continues to be a popular way to model spin states. More recently, Clark

and Davidson introduced a projection method[194] to compute expectation values of local spin operators from quantum chemistry calculations. This technique employs the Löwdin atomic populations[126] to define fragment projection operators P_A, which are applied in turn to the total spin to obtain local spin operators

$$\mathbf{S}_A = \sum_{i=1}^{N} \mathbf{S}(i) P_A(i) \tag{36}$$

where $\mathbf{S}(i)$ is the spin operator for electron i. In applications to simple closed and open-shell molecules, this approach revealed relationships between expectation values of quantities such as $\langle \hat{\mathbf{S}}_A \hat{\mathbf{S}}_B \rangle$ and $\langle \hat{\mathbf{S}}_A^2 \rangle$ and the intuitive concept of chemical bond order.[194] Several related approaches to the definition of local spin states exist; for further reading on the topic, we suggest the recent review by Reiher.[195]

Local spin operators are valuable tools for extracting information about spin from converged electronic structure calculations. Moreover, provided a satisfactory definition of local spin, it becomes possible to construct self-consistent electronic structure methods which are intentionally steered to achieve a particular value of the local spin. Constrained DFT is especially well-suited for this class of applications because CDFT constraints can be defined over arbitrary local sites in the system.

In this section we review several studies in which CDFT has been applied to spin states. In some cases, the spin is localized on one molecule in a larger system, while in others the spin is localized on a particular site within a molecule, such as a metal center. In both cases, the CDFT approach alleviates certain shortcomings with the conventional DFT description and brings theory closer to agreement with experiment through more controlled approximations to spin states.

4.1 Tracing Out Constant-spin States

In certain situations, it can be useful to treat entire molecules as local spin sites within a larger system. This picture is especially fruitful in the study of reactions between subsystems of different spin symmetry, in which an adiabatic picture of the reaction can excessively delocalize the spin and lead to an incorrect description of the reaction. CDFT has been used to study reactions of this type. In a particularly striking illustration of this approach, CDFT helped elucidate the origins of a long-standing disagreement between theory and experiment concerning a fundamental process in surface science: the dissociative adsorption of molecular oxygen on the (111) surface of aluminum.[196]

The probability that an oxygen molecule incident on the Al(111) surface will dissociate and be adsorbed is known from experiments to depend strongly on the kinetic energy E of the O_2 molecule, a ground-state triplet.[197] A plot of the adsorption probability as a function of the O_2 kinetic energy, known as a sticking curve, is shown in Figure 18. The sticking curve shows that O_2 molecules with very low kinetic energy are unlikely to be adsorbed. The adsorption probability increases with increasing O_2 kinetic energy until reaching a plateau at higher energies.

Several theoretical treatments of the dissociative adsorption of O_2 on Al(111), including sophisticated first-principles investigations,[198,199] predicted near-unity sticking probability regardless of O_2 kinetic energy due at least in part to the lack of a barrier to dissociation on the O_2/Al(111) potential energy surface (PES). Scheffler *et al.* examined the adiabatic PES in detail with the PBE and revised PBE (RPBE) functionals and observed spurious fractional charge transfer from Al to O_2 even at long distances.[196] Spin conservation laws strongly disfavor this partial quenching of the unpaired spin in triplet O_2 at long distances. To compensate for this shortcoming of the adiabatic PES, they introudced a spin-constrained DFT approach to force the O_2 molecule in the interacting O_2/Al(111) system to remain in its triplet ground state during their simulations.[196]

The adiabatic and diabatic (triplet) sticking curves were computed through a three-step procedure.[200] First, the PES of the O_2/Al(111) system was mapped along the six O_2 degrees of freedom, with the metal surface held fixed. An analytical form for the PES was then obtained through a neural network interpolation scheme.[201,202] Finally, thousands of molecular dynamics (MD) trajectories were simulated on the analytical PES and the sticking probabilities were calculated from statistical analysis of the trajectories.

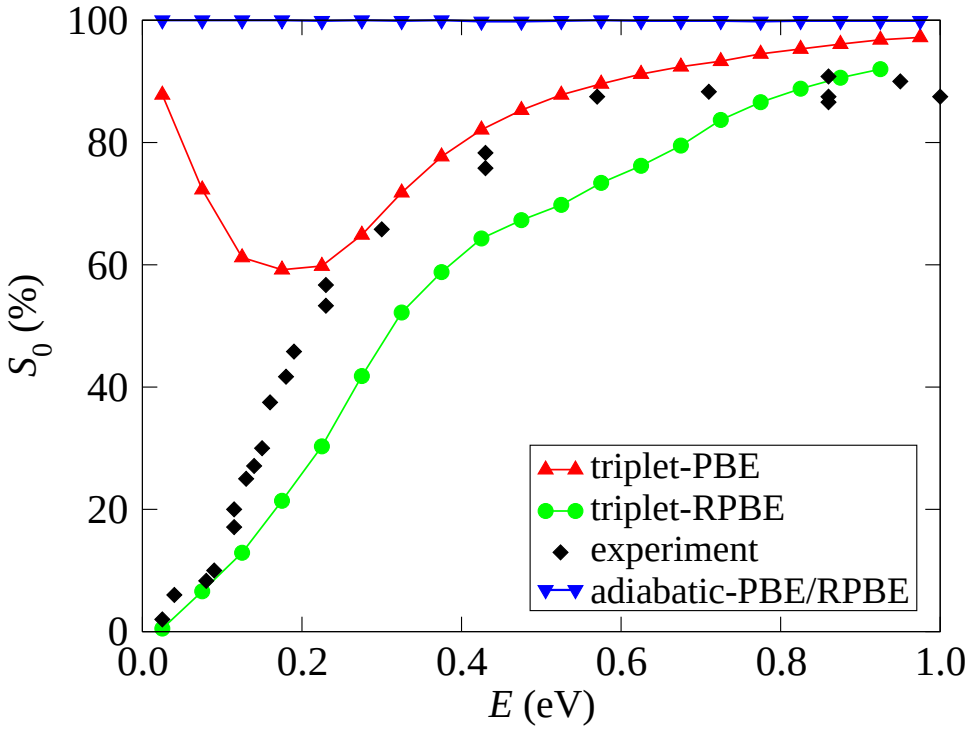

Figure 18: Experimental (black), conventional adiabatic DFT (blue), and triplet spin-constrained DFT (red and green) initial sticking curves for O_2 on the Al(111) surface. Reproduced with permission from ref 200.

The adiabatic simulations generally presented barrierless pathways to O_2 dissociation, even if the Al degrees of freedom were included in the simulations. In contrast, CDFT parameterization of the diabatic PES revealed barrier heights up to 0.9 eV, as illustrated schematically in Figure 19. MD simulations on the diabatic PES gave sticking curves that qualitatively agree with experimental data for moderate to high O_2 kinetic energy (Figure

18). At lower kinetic energies, the PBE functional showed an unphysical trend towards higher sticking probabilities. This feature was rationalized in terms of the tendency of the PBE functional to predict lower dissociation barriers for the O_2/Al(111) system relative to the RPBE functional. Several pathways were identified on the PBE PES which enabled low-energy O_2 molecules to undergo barrierless dissociation, artificially raising the sticking probability.

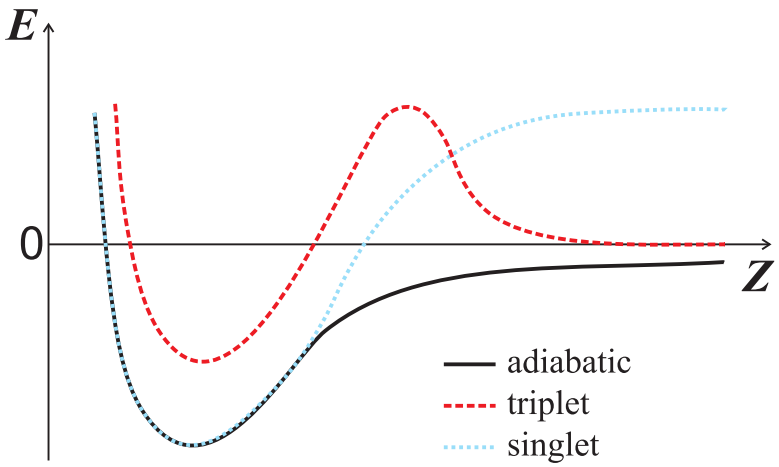

Figure 19: Schematic of the diabatic (singlet and triplet) and adiabatic PES for O_2 approaching the Al(111) surface. Z represents the O_2–Al(111) distance. The diabatic triplet PES was found to exhibit a barrier which is responsible for the experimentally observed scattering of most incident O_2 molecules at low kinetic energy. Reproduced with permission from ref 200.

A magnetization density analysis of O_2 at the barrier to dissociation illustrates one reason behind the success of the constrained spin-density approach. In Figure 20, the magnetization density of the system near the dissociation barrier is shown for (a) the pure ground-state O_2 triplet; for (b) the adiabatic O_2 PES; for (c) a fixed spin moment (FSM) calculation in which the total spin of the system is constrained but not localized on O_2; and for (d) the constrained diabatic O_2 PES. The physical origin of the dissociation barrier is attributed to enhanced Pauli repulsion at the O_2/Al(111) interface, which is only evident in (d). The fixed spin moment calculation in (c) shows a negligible dissociation barrier despite the constraint

on total spin because the magnetization density of the triplet O_2 is largely transferred to the aluminum.

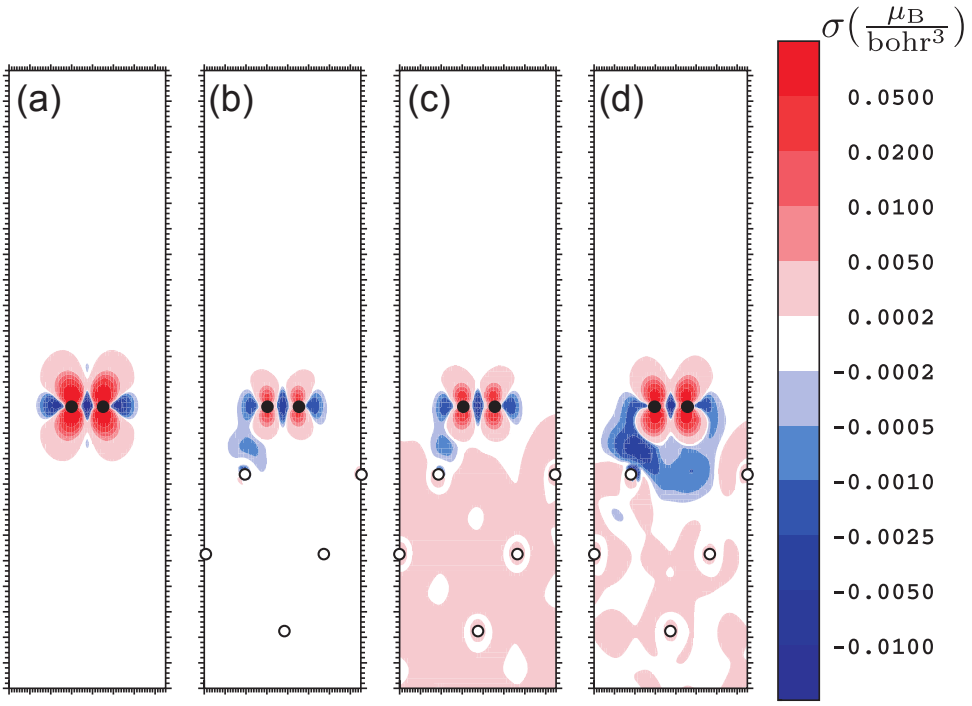

Figure 20: Magnetization density cross-section of triplet O_2 at the energetic barrier to its approach to the Al(111) surface. Black dots represent O nuclei; white dots represent Al nuclei. (a) Free O_2 triplet, no aluminum. (b) Adiabatic O_2/Al(111) calculation. (c) Fixed spin moment calculation. (d) Spin-constrained calculation. Reproduced with permission from ref 200.

Constrained DFT provided the earliest qualitatively correct first-principles theoretical description of the dissociative adsorption of O_2 on Al(111). This reaction continues to attract significant interest in surface science. More recent theoretical studies have employed nonadiabatic surface-hopping MD simulations[203] and have considered the roles of self-interaction error[204] and memory effects[205] on adsorption at metal surfaces. In these studies, CDFT provides a convenient way to capture nonadiabaticity by forcing molecules to preserve their proper spin states as they begin to interact. In the next section, we consider applications in which spin constraints are applied on an *intra*molecular scale in order to describe single molecules with several spin centers.

4.2 The Heisenberg Picture of Molecular Magnets

The promise of tunable magnetism at the single-molecule level has driven a vast and growing body of research in molecular magnetism that is too large to review here. The interested reader may find several reviews discussing the scope of candidate structures,[206,207] the range of applications,[207] and the underlying physics.[188,208] Molecular magnets generally possess one or more metal centers on which most of the spin density is localized. In this section, we discuss how CDFT has been used to enforce spin localization when it is artificially diminished due to limitations of available density functional approximations; but first, we summarize some features of other density functional approaches to molecular magnetism.

The Heisenberg Hamiltonian (equation (35), also sometimes referred to as the Heisenberg-Dirac-van Vleck or HDVV Hamiltonian) is a common starting point for theoretical models of molecular magnetism. Semi-empirical or *ab initio* methods may be used to compute the exchange couplings J, which in turn determine the energies of the available spin states. Most molecular magnets are too large to describe using correlated wave-function methods, so DFT is the more commonly employed tool for computing the exchange couplings. Within the Kohn-Sham formalism, the difficulty arises that certain spin states may not be representable by a single Kohn-Sham determinant with available density functional approximations. For example, in a system with two unpaired electrons, the singlet spin state $|\Psi_s\rangle$ is a linear combination of two Kohn-Sham determinants,

$$|\Psi_s\rangle = \frac{1}{\sqrt{2}}\left(|\uparrow\downarrow\rangle \; - |\downarrow\uparrow\rangle\right) \tag{37}$$

The $|\uparrow\downarrow\rangle$ and $|\downarrow\uparrow\rangle$ determinants are referred to as broken symmetry (BS) states because they are not eigenfunctions of $\hat{S}^2$. Note that the highest-spin state of a given multiplet is always representable by a single determinant, e.g. for two unpaired electrons the high-spin triplet can be described by the determinant $|\uparrow\uparrow\rangle$.

Noodleman proposed a way to extract exchange couplings from the BS states[209] by treating each BS state as an uncoupled spin state, i.e. a state in which the unpaired electrons are each assigned a local site and spin such that they reproduce the z component of the total spin of the state. For the case of two metal centers A and B, the BS-DFT exchange coupling is given by

$$J_{AB} = \frac{E_{\mathrm{BS}} - E_{\mathrm{HS}}}{4S_A S_B} \tag{38}$$

where E_{HS} (E_{BS}) is the energy of the high-spin (low-spin) state. An alternative formula has been proposed[210] that treats the low-spin BS state as an approximation to the coupled low-spin configuration with $\langle \hat{S}^2 \rangle = (S_A - S_B)(S_A - S_B + 1)$ rather than the uncoupled configuration with $\langle \hat{S}^2 \rangle = (S_A - S_B)^2$,

$$J_{AB} = \frac{E_{\mathrm{BS}} - E_{\mathrm{HS}}}{2\left(2S_A S_B + S_B\right)} \tag{39}$$

An expression in terms of the $\langle \hat{S}^2 \rangle$ value of the relevant Kohn-Sham determinants has also been proposed,[211]

$$J_{AB} = \frac{E_{\mathrm{BS}} - E_{\mathrm{HS}}}{\langle \hat{S}^2 \rangle_{\mathrm{HS}} - \langle \hat{S}^2 \rangle_{\mathrm{BS}}} \tag{40}$$

This expression can be thought of as an interpolation between the uncoupled and coupled spin approximations in Equations 38 and 39, respectively.[39]

Notwithstanding the many successes of the BS approach,[212] the method is known to overstabilize singlets, resulting in J_{AB} values that are too negative.[213,214] Further, from a formal perspective, the existence of BS states is an artifact of approximations to the exchange-correlation functional:[39] the exact exchange-correlation functional takes spin symmetry fully into account and therefore obtains the exact ground state of each spin configuration.[215] Thus, BS states obtained from inexact exchange-correlation functionals are not rigorous approximations to the uncoupled spin states; in particular, the spatial extent of excess spin density

in BS states is uncontrolled.

As an alternative approach to the uncoupled spin states, CDFT can be used to enforce localization of the unpaired spins on their assigned centers.[39] For example, in a hetero-bimetallic complex with metal centers A and B, one might constrain the spin density on metal center A to integrate to one net α ($\uparrow$) spin while also constraining the spin density on metal center B to integrate to one net β ($\downarrow$) spin. The CDFT exchange coupling is then computed according to

$$J_{AB} = \frac{E_{\uparrow\downarrow} - E_{\uparrow\uparrow}}{4S_A S_B} \tag{41}$$

These local spin states are a more controlled approximation to the uncoupled spin states than those defined through the BS approach,[39] and their single-reference character is well-suited to available density functional approximations.

Complex	J_{AB} (cm^{-1})				
	CDFT	Eq. 38	Eq. 39	Eq. 40	Expt.
$[Cu^{II}_2(MeC(OH)(PO_3)_2)_2]^{4-}$	-16	-139	-70	-139	-31[a]
$[(Et_5dien)_2Cu^{II}_2(\mu\text{-}C_2O_4)]^{2+}$	-44	-133	-67	-132	-37[b]
$[Mn^{II}(NH_3)_4Cu^{II}(oxpn)]^{2+}$	-128	-284	-237	-278	-16[c]
$[(\mu\text{-}OCH_3)V^{IV}O(maltolato)]_2$	-83	-89	-45	-89	-107[d]
$[Ph_4P]_2[Fe^{II}_2OCl_6]$	-124	-163	-136	-160	-112[e]
$[Mn^{III}Mn^{IV}(\mu\text{-}O)_2(\mu\text{-}OAc)DTNE]^{2+}]$	-128	-168	-134	-165	-110[f]
$[Cu_2(DMPTD)(\mu_2\text{-}N_3)(\mu_2\text{-}Cl)Cl_2]CH_3CN$	112	113	57	110	84[g]
$[Cu_2(\mu\text{-}OH)_2(bipym)_2](NO_3)_2{\cdot}4H_2O$	57	112	56	111	57[h]
$[(Dopn)Cu^{II}(OH_2)Cr^{III}(OCH_3)L](ClO_4)_2{\cdot}H_2O$ [i]	23	10	7	10	19[j]
$[(Dopn)Cu^{II}(\mu\text{-}CH_3COO)\text{-}Mn^{III}L](ClO_4)_2{\cdot}H_2O$[i]	75	48	38	48	55[j]

[a]reference 216; [b]reference 217; [c]reference 218; [d]reference 219; [e]reference 220; [f]reference 221; [g]reference 222; [h]reference 223; [i]) L=1,4,7-trimethyl-1,4,7-triazacyclononane; [j]reference 224.

Table 5: Magnetic exchange couplings for different dinuclear complexes obtained by CDFT and the indicated BS-DFT approaches, with experimental results for comparison. Modified with permission from ref 39.

Rudra *et al.* demonstrated the advantages of the CDFT approach to magnetic exchange couplings relative to the BS approach for a diverse collection of magnetic transition-metal complexes.[39] Comparing the CDFT exchange couplings with couplings obtained from sev-

eral BS-DFT prescriptions, shown in Table 5, it is clear that CDFT offers comparable to superior accuracy relative to BS calculations for both antiferromagnetically ($J > 0$) and ferromagnetically ($J < 0$) coupled centers. CDFT predicts qualitatively correct exchange couplings whereas BS-DFT couplings show some tendency to overestimate the strength of these interactions.

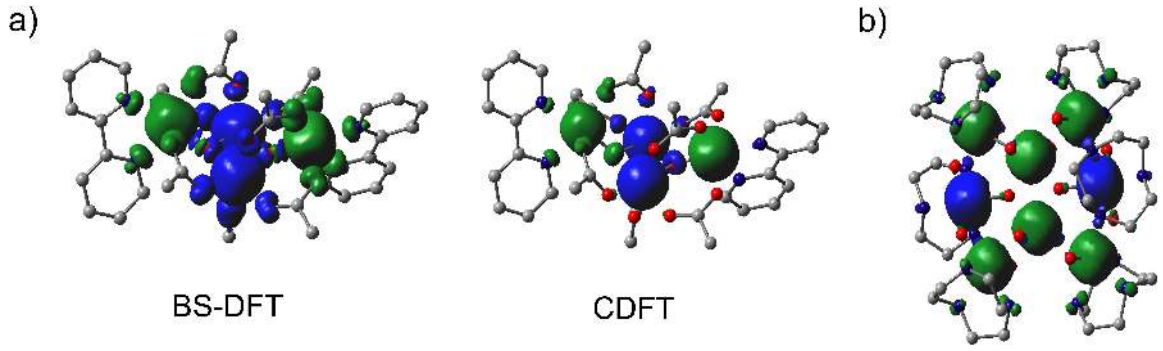

Figure 21: (a) Spin density of a low-spin state of a tetranuclear iron cluster, determined from BS-DFT (left) and CDFT (right). The spin density is significantly more localized on the metal centers in the CDFT calculation. (b) Ground-state spin density of the Fe_8 molecular magnet from CDFT calculations. Green (blue) isosurfaces represent net α (β) spin density. Reproduced with permission from ref 225.

The CDFT approach to exchange couplings is applicable to the more general case of several local spin sites, as shown by Rudra and co-workers[225] in a computational study of frustrated molecular magnets such as the tetranuclear iron cluster $[Fe_4O_2(O_2CCH_3)_7(bpy)_2]^+$ shown in Figure 21a. This study demonstrated that the difficulty of describing low-spin excited states with BS-DFT leads to predictions for molecular magnets that sometimes contradict experimental findings, whereas the CDFT results were at least in qualitative agreement with experiment in each case. For example, CDFT predicts the experimentally known antiferromagnetic interaction for the weaker of the two exchange couplings in the tetranuclear iron cluster, whereas the interaction is ferromagnetic in BS-DFT. Delocalization of the spin density of low-spin states in BS-DFT (left side of Figure 21a) artificially stabilizes these states relative to other states, resulting in an incorrect sign for the coupling. Note that

the spin density in CDFT is mostly localized on the iron centers in Figure 21a despite the fact that the ligands were also included in the constraint regions. The spin-frustrated ground state spin density of the Fe_8 cluster obtained from CDFT and shown in Figure 21b agrees with data from polarized neutron diffraction and ^{57}Fe NMR experiments.[226,227] Thus, CDFT calculations can quantify the relative energetics of complicated spin systems, including those arising in frustrated molecular magnets.

Broken symmetry methods remain popular because they are well-studied and readily available; nevertheless, the CDFT approach to exchange couplings holds promise for future studies of molecular magnetism for two reasons. First, CDFT allows control of the spin localization, which can be quite useful in locating the various spin states. Though not widely publicized, the biggest challenge in BS-DFT is usually getting the various spin states to converge. CDFT circumvents this obstacle by giving the user manual control over which localized spin pattern the calculation converges to, making the calculations much more reliable. Second, CDFT offers an even-handed description of ground and excited states. In the following section, we illustrate the latter point by focusing on the splitting between a special pair of spin states: the lowest singlet and triplet charge transfer excited states in dimers of organic dyes.

4.3 Singlet-Triplet Gaps of Intermolecular CT States

The relative populations of singlet and triplet states in organic semiconductors (OSCs) directly affect the efficiency of organic light-emitting devices (OLEDs) and organic photovoltaics (OPVs). In the case of OLEDs, free electrons and holes in the OSC associate at a donor-acceptor interface to form charge-transfer (CT) excited states. These CT states may be generated with either singlet or triplet spin. Charge recombination of the CT state to form a localized electron-hole pair, or exciton, generally takes place with retention of spin character. Singlet excitons are efficient light emitters, because the relaxation to the ground

state via fluorescence is spin allowed. The analogous transition from the triplet exciton is forbidden. Hence, triplet formation is considered an indirect loss mechanism for OLEDs, and the relative populations of singlet versus triplet CT states formed at the interface influence the overall efficiency of the OLED.

If free electrons and holes associate randomly in an OLED, one expects a 3:1 statistical ratio of triplet to singlet CT states. In practice, some OSCs exhibit this ratio while others obtain a larger fraction of singlet CT states.[228–230] Enhancement of the singlet pathway is certainly beneficial for the efficiency of OLEDs, but the mechanism underlying this enhancement is not immediately clear. Initial proposals invoked Marcus inverted region behavior: the triplet exciton is lower in energy than the singlet, so the free energy of charge recombination from the CT state to the singlet exciton will be smaller than that for the triplet, $\Delta G_S^{\mathrm{CR}} < \Delta G_T^{\mathrm{CR}}$. Since ΔG^{CR} is on the order of 1 eV and the reorganization energy λ is on the order of 0.1 eV, the recombination is in the inverted regime and the singlets will form faster than the triplets. Thus, if one assumes facile spin randomization in the CT state, then the kinetics dictate enhanced singlet exciton generation because they are formed more frequently.[190]

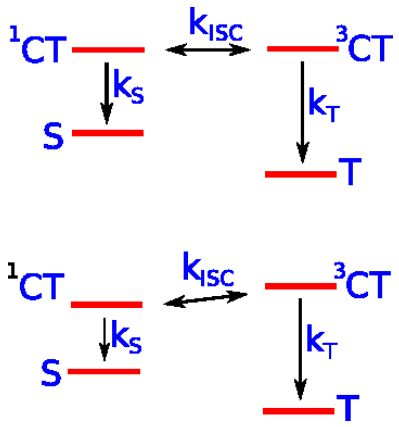

Figure 22: Exciton formation pathways for nearly degenerate CT states (top) and for $\Delta E_{\mathrm{ST}} < 0$ (bottom). S and T label singlet and triplet excitons, respectively. Reproduced with permission from Ref. 231.

An alternative hypothesis is that the ratio of singlet versus triplet excitons is governed by the energy gap between the singlet and triplet CT states, $\Delta E_{\mathrm{ST}} = E\,(^3\mathrm{CT}) - E\,(^1\mathrm{CT})$. To explore the role of the energy gap on the relative rates of singlet and triplet exciton formation, Difley *et al.* used CDFT to compute the energies of these CT states and obtain ΔE_{ST} directly.[231] Their investigation centers on the observation that, for systems in the Marcus inverted region, a large ΔE_{ST} discourages intersystem crossing; thus fluorescence in an OSC may be enhanced by a small ΔE_{ST} or precluded by a large ΔE_{ST}.

Contrary to the common (Hund's rule) assumption, it was found that $\Delta E_{\mathrm{ST}} < 0$ for the CT states of the studied chromophore dimers. As shown in Table 6, the magnitude of the splitting varies from a few meV to over 100 meV depending not only on the particular dimer but even on the translational offset of the donor relative to the acceptor in the solid state.

	ΔE_{ST} (meV)	
Chromophore	3-21G	6-31G*
α-Alq_3 [a]	-2	-2
β-Alq_3 [a]	-6	-7
δ-Alq_3 [b]	-60	-74
1-R_1-dpa [c]	-58	-61
4-R_2-dpa [c]	-1	-5
4-R_3-dpa [c]	-30	-42
$Zn(sada)_2$ [d]	-102	-102
$[Zn(bbp)_2]^{2+}$ [e]	-67	-57
$[Zn(tpt)_2]^{2+}$ [e]	-19	-48
$[Zn(tpy)_2]^{2+}$ [e]	-85	-89

Table 6: ΔE_{ST}. [a]Alq_3 = tris(8-hydroxyquinoline)aluminum(III) [b]Alq_3 = tris(8-hydroxyquinoline)aluminum(III) [c]dpa = 2,2′-dipyridylamine, R_1 = pyrenyl, R_2 = (1-pyrenyl)phenyl, R_3 = 4′-(1-pyrenyl)biphenyl [d]$Zn(sada)_2$ = bis[salicylidene(4-dimethylamino)aniline]zinc(II) [e]bbp = 2,6-bis(1*H*-benzimidazol-2-yl)pyridine, tpt = 2,4,6-tris(2-pyridyl)-1,3,5-triazine, tpy = 2,20′:6′,2″-terpyridine Adapted with permission from ref 231.

The negative singlet-triplet splittings predicted using CDFT were rationalized using a

perturbation theory-based expression for the splitting,

$$\Delta E_{\mathrm{ST}} = -\frac{t^2}{\Delta E} + K \tag{42}$$

where t is an intrinsic electron hopping rate between donor and acceptor, while ΔE describes the energy gap between the initial state and virtual states in the system that facilitate hopping. The second term K is the usual exchange integral which stabilizes the triplet. On the other hand, the first term, which describes kinetic exchange, tends to stabilize the singlet, as illustrated in Figure 23. This exchange process stabilizes the singlet CT state because of the transient pairing of spins, which is an inaccessible configuration for the triplet CT state.

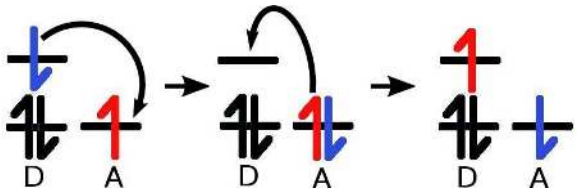

Figure 23: Illustration of the kinetic exchange mechanism. The process of exchanging spins involves transient spin-pairing; this process favors the singlet CT state because Pauli repulsion prevents this type of kinetic exchange in the triplet CT state. Reproduced with permission from ref 231.

To assess the kinetic exchange hypothesis, Difley *et al.* approximated the hopping term t by donor-acceptor orbital overlaps S and studied how ΔE_{ST} and S vary as a donor and acceptor are laterally displaced from one another. Figure 24 shows that the variation in HOMO/LUMO S^2 along the displacement coordinate tracks the variation in ΔE_{ST} rather well for poly-*p*-phenylene and for DCM. This proportionality suggests that the kinetic exchange term $-t^2/\Delta E$ is the dominant factor controlling ΔE_{ST} in these dimers and that the kinetic exchange stabilization is dominated by HOMO/LUMO interactions.

Interest in understanding and tuning ΔE_{ST} is only expected to grow as research into OLEDs and OPVs increasingly turns to the manipulation of spin states to increase per-

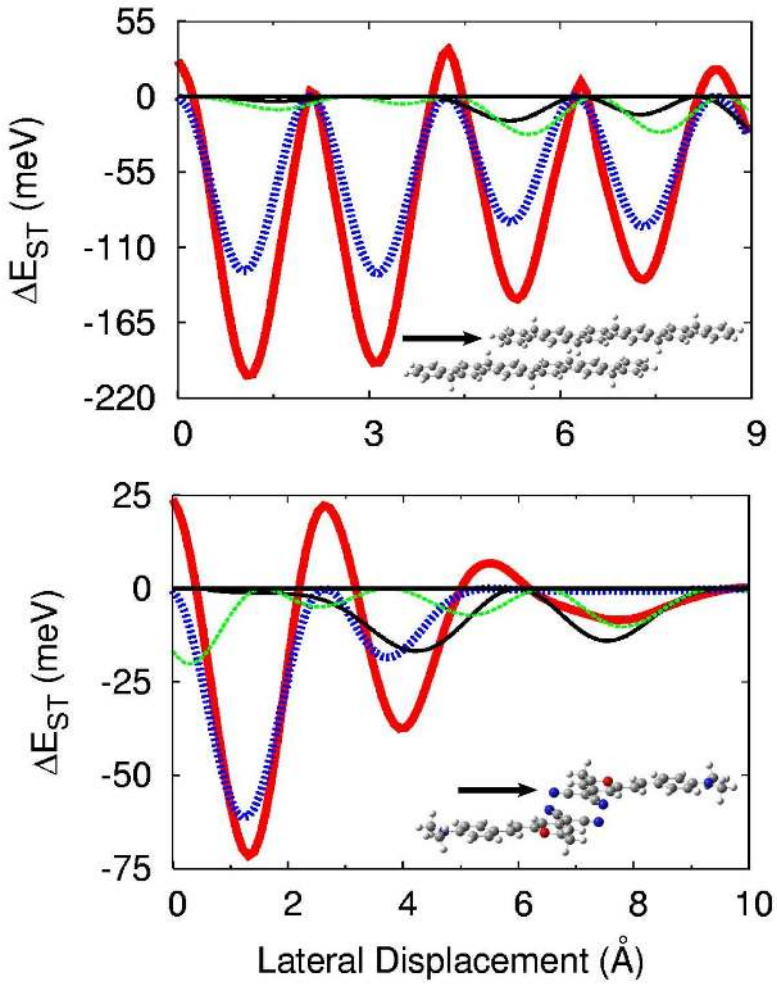

Figure 24: ΔE_{ST} (thick solid red curve) and squared orbital overlaps for poly-*p*-phenylene (top) and DCM (bottom) as a function of layer monomer displacement. Squared overlaps (in arbitrary units) are shown for: HOMO/LUMO (thick dashed blue line), HOMO−1/LUMO (thin solid black line), and HOMO/LUMO+1 (thin dashed green line). Reproduced with permission from ref 231.

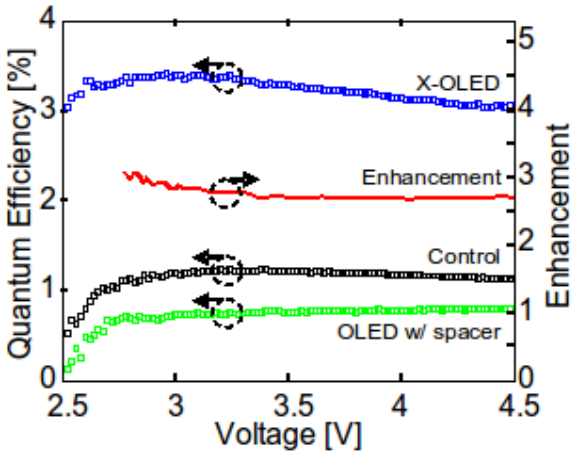

Figure 25: Quantum efficiency of a heavy metal doped OLED (X-OLED) device versus control OLED. The efficiency enhancement (thick red line) is also shown, plotted against the right axis. Reproduced with permission from ref 235.

formance.[232,233] Insights into the role of ΔE_{ST} in modulating singlet versus triplet exciton generation have already been brought to bear on OLED design. Segal *et al.* incorporated an iridium complex (FIrpic)[234] as the electron transport layer of an OLED to enhance spin randomization during exciton formation through increased spin-orbit coupling.[235] The resulting extrafluorescent OLED (X-OLED) demonstrated nearly threefold enhancement of the quantum efficiency (Figure 25). It has also been pointed out[233] that spin control of CT-state generation appears to be a more promising route to achieving long-lived CT states in small-molecule donor-acceptor dyads than the exploitation of Marcus inverted region behavior in these systems. Reliable first-principles calculations of ΔE_{ST} will prove valuable in the interpretation of ongoing time-resolved EPR[236] and CINDP experiments[237] that can probe ΔE_{ST} in OLED and OPV matrerials.

4.4 Related and Ongoing Work

The use of constraints on the spin density is finding application in several other areas of chemistry and physics. One promising use of the technique is in the suppression of spin

	None	All	Ligands	Experiment
$\langle \hat{S}^2 \rangle$	2.1266	0.7525	0.7525	(0.75)
A_{iso}	-340	-1	-284	-219
A_{dip}	-30	-145	-145	-115.2

Table 7: $\langle \hat{S}^2 \rangle$ values, isotropic and anisotropic components of the hyperfine coupling constant A (in MHz) for the $[Mn(CN)_5NO]^{2-}$ complex obtained via unconstrained (None), fully constrained (All), and ligand-constrained (Ligands) calculations with the BHPW91 functional. Adapted with permission from ref 238.

contamination in unrestricted Kohn-Sham (UKS) calculations.[238] By taking advantage of a previously proposed approximate density-based metric[239] for $\langle \hat{S}^2 \rangle$,

$$\langle \hat{S}^2 \rangle = S(S+1) - \int_{\mathcal{R}=\left\{\mathbf{r} \,|\, \rho^\alpha(\mathbf{r}) - \rho^\beta(\mathbf{r}) < 0\right\}} \left(\rho^\alpha(\mathbf{r}) - \rho^\beta(\mathbf{r})\right)\, d^3r \tag{43}$$

Schmidt *et al.* fixed a target value of $\langle \hat{S}^2 \rangle$ and solved the UKS equations subject to the constraint defined by equation (43) on the density.

This spin contamination constraint is useful not only for eliminating spin contamination from UKS calculations, but also for restricting spin contamination only to regions of a system where spin polarization is anticipated on physical grounds. The hyperfine coupling tensor $\mathbf{A}$, which describes the interaction of an electronic spin $\mathbf{S}$ and a nuclear spin $\mathbf{I}$ via the Hamiltonian $H = \mathbf{S} \cdot \mathbf{A} \cdot \mathbf{I}$, is an experimentally observable probe of spin polarization; thus, DFT modeling of hyperfine couplings is especially sensitive to the description of spin polarization. Spin-contamination constrained calculations on the transition metal complex $[Mn(CN)_5NO]^{2-}$ bring predictions of the anisotropic component of the hyperfine coupling constant within 30% of the experimental value, whereas the unconstrained calculation disagrees with experiment by more than 70%, as shown in Table 7. The spin contamination constraint was also applied to compute diabatic dissociation curves for the OF radical. This approach was able to correctly predict the OF distance at which the cross-over from singlet to triplet character is expected to occur.

Constrained density functional methods are also becoming standard in computational studies of nanoscale magnetization in metallic clusters and bulk metals. Because magnetically excited states (i.e. magnons) in metals[240] do not necessarily correspond to stationary points on the adiabatic PES, these states require an approach in which the magnetization is constrained. A common approximation in DFT modeling of magnetic configurations in a metal is the atomic sphere approximation (ASA),[241] in which the spin density is projected onto a pre-defined local spin quantization axis[95] within a sphere around each atom prior to evaluation of the exchange-correlation energy. The ASA is a further approximation beyond the local spin density approximation. It has been shown[242] that constraining the density with the ASA can result in magnetizations which are not parallel to the self-consistently determined magnetic fields which produce them — a situation which is technically not stationary and leads to drastically incorrect predictions of the moment magnitudes for Ni and Co metal.[95]

Gebauer and Baroni used a constrained DFT approach to study magnetic excitations from the spin-spiral ground state of bcc iron.[243] Unlike charge and spin constraints in CDFT — which are enforced by an external electric potential — their magnetization constraint is enforced by an external magnetic potential which depends self-consistently on the density. Calculations of the magnon frequencies in bcc iron yielded a dispersion curve in near-quantitative agreement with experiments on pure iron at 10 K.[243] A comparative study of ASA and constrained LSDA descriptions of magnetic configuarations in Fe, Ni, and Co revealed that constrained LSDA is not only more accurate for predicting magnetic moments in metals, but it is also more robust to the choice of approximate representation of the magnetization density than the ASA.[95]

Across a diverse set of applications, the CDFT description of spin states has proven useful for computing spin-dependent observables from first principles. Furthermore, in studies of molecular magnets and OLEDs, CDFT has provided physical insights, such as the trend for

singlet CT states to lie energetically below their triplet counterparts. CDFT is an important step towards quantitative first-principles descriptions of spin energetics and dynamics which may contribute to the understanding and development of next-generation spin-dependent technologies. Further, constrained spin states form a suitable basis for configuration interaction methods such as CDFT-CI (discussed in section 6), which gives accounts for couplings between spin states.

5 Coupling CDFT States Together

The previous sections have shown a variety of applications wherein CDFT is used to produce localized diabatic states which are then analyzed to yield information about electron transfer, CT-state dynamics, molecular magnets, and more. Diabatic states such as these have a long history in chemistry, being incorporated into valence bond theories of bonding and models for molecular energy surfaces, with a strong continuing presence in the diverse spread of methods for their determination.[155,156,244–261] Diabatic states do not change character as a function of nuclear position and as such are at the core of many qualitative pictures of molecular electronic structure, including the charge-transfer states of section 3 and the uncoupled spin states of section 4. But to fill out the diabatic picture, electronic couplings between these diabatic states are also needed, describing how population flows between the diabats as the system evolves. This is in contrast with the adiabatic (Born-Oppenheimer) picture, where electronic states are always taken to be eigenstates of the electronic Hamiltonian with no direct coupling to each other, no matter the geometry of the system. Nonetheless, the diabatic picture proves itself quite useful, producing PESs for dynamics that vary slowly with nuclear coordinates and thus avoid sharp changes where errors can accumulate. Additionally, diabats are invoked to assign vibronic transitions in spectroscopy and for qualitative descriptions of molecular bonding (as for the LiF example of Figure 42), electron transfer (cf section 3), and proton tunneling. However, since the diabatic states are not eigenstates of the electronic Hamiltonian, chemistry (that is, reactions) in the diabatic basis must necessarily incorporate multiple diabats, and the diabatic coupling between them:

$$H_{ab} = \left\langle \Psi_a \middle| \hat{H} \middle| \Psi_b \right\rangle . \tag{44}$$

These couplings aid in determining the rate of electron-transfer processes (cf equation (33)) as occur in organic semiconductors (OSCs)[160,262–264] and solution electrochemistry,[265–268] and

also govern energy transfer in photochemistry.[269–271] In addition to these direct applications, the couplings can be combined with the diagonal diabatic energies as an alternate route to adiabatic energies, as will be explored in section 6.

In this section we describe how to compute the coupling H_{AB};[47,54,55,132,272] we then compare these couplings with results from other coupling prescriptions that have seen use, and describe how our scheme fits in with the landscape of other proposed approaches to diabatic couplings. Finally, we give a few illustrations of how diabatic couplings may be used in the context of chemical or electronic transformations.

5.1 Evaluating CDFT Couplings

Given two electronic states $|\Psi_1\rangle$ and $|\Psi_2\rangle$, the coupling between them is just the matrix element of the Hamiltonian,

$$H_{AB} = \langle \Psi_1 | \hat{H} | \Psi_2 \rangle \tag{45}$$

The behavior of this coupling is in general quite complicated, but there are simple cases that can be more easily understood. Considering a system that includes electron donor and acceptor moieties, natural descriptions of $|\Psi_1\rangle$ and $|\Psi_2\rangle$ would be to have an electron on the donor and acceptor, respectively. If the moieties are spatially removed from each other, the coupling is dominated by overlap between the tails of the wavefunctions on the two fragments. Since the tail decays exponentially, the coupling is also expected to decay exponentially with donor-acceptor separation as a result of this "through-space" coupling.[273] However, when the donor and acceptor are joined by a bridge moiety, the coupling can be increased due to a superexchange mechanism involving the electrons on the bridge, a form of "through-bond" coupling.[274,275]

It is a bit difficult to see how equation (45) can be computed in the context of CDFT. The exact expression is writen in terms of the wavefunctions for donor and acceptor, but

KS theory only gives us the *density* of each state. The KS wavefunctions, $|\Phi\rangle$, are fictitious determinants that are constructed to give the correct density. Hence, in practice we need some approximate (but hopefully accurate) prescription for computing the coupling betwen two CDFT states. The most common prescription for this task was provided in ref 54. Here, we note that if the diabatic states are defined by constraints, then neither of the exact wavefunctions, $|\Psi_i\rangle$, is an eigenstate of the Hamiltonian. Rather they are eigenstates of $\hat{H}$ plus the relevant constraining potential $V_i w_i(\mathbf{r})$:

$$\left[\hat{H} + V_i w_i(\mathbf{r})\right] |\Psi_i\rangle = F_i |\Psi_i\rangle. \tag{46}$$

We can therefore manipulate equation (45) to read:

$$\begin{aligned}
H_{AB} &= \left\langle \Psi_1 \middle| \hat{H} \middle| \Psi_2 \right\rangle && (47)\\
&= \left\langle \Psi_1 \middle| \frac{\hat{H} + V_1\hat{w}_1(\mathbf{r}) + \hat{H} + V_2\hat{w}_2(\mathbf{r})}{2} - \frac{V_1\hat{w}_1(\mathbf{r}) + V_2\hat{w}_2(\mathbf{r})}{2} \middle| \Psi_2 \right\rangle && (48)\\
&= \left\langle \Psi_1 \middle| \frac{F_1 + F_2}{2} - \frac{V_1\hat{w}_1(\mathbf{r}) + V_2\hat{w}_2(\mathbf{r})}{2} \middle| \Psi_2 \right\rangle && (49)\\
&= \frac{F_1 + F_2}{2} S_{12} - \left\langle \Psi_1 \middle| \frac{V_1\hat{w}_1(\mathbf{r}) + V_2\hat{w}_2(\mathbf{r})}{2} \middle| \Psi_2 \right\rangle && (50)
\end{aligned}$$

Thus, the coupling only requires the free energies F_i (introduced in eq 26 in section 2), the overlap between the states and the matrix elements of a one-electron potential between the states. This is certainly simpler than the many electron matrix element we started with, but it still requires the (unknown) wavefunctions $|\Psi_i\rangle$. Hence, at this point we approximate the true wavefunctions by their KS surrogates ($|\Psi_i\rangle \approx |\Phi_i\rangle$) to arrive at a formula for the CDFT diabatic coupling:

$$H_{AB} \approx \frac{F_1 + F_2}{2} S_{12}^{\mathrm{KS}} - \left\langle \Phi_1 \middle| \frac{V_1\hat{w}_1(\mathbf{r}) + V_2\hat{w}_2(\mathbf{r})}{2} \middle| \Phi_2 \right\rangle \tag{51}$$

Approximating the exact wavefunction with the appropriate KS determinant is an uncontrolled approximation and it must be tested in practice. As a whole the approximation holds up well, but it is obvious that a more rigorous definition of the diabatic coupling in CDFT would be a significant discovery. For now, we will move forward with the approximation of equation (51).

In the framework of CDFT, the diabatic states $|\Phi_1\rangle$ and $|\Phi_2\rangle$ are not mutually orthogonal, so we must perform an orthogonalization procedure in order to produce a physically meaningful coupling H_{ab} (note the use of lower case indices for orthogonal states). Toward this end, we may begin with the Hamiltonian in the non-orthogonal basis, and transform it into an orthogonal basis via the symmetric Löwdin orthogonalization.[47] Putting

$$\mathbf{H}' = \begin{pmatrix} H_{11} & H_{12} & \cdots & H_{1N} \\ H_{21} & H_{22} & & H_{2N} \\ \vdots & & \ddots & \vdots \\ H_{N1} & H_{N2} & \cdots & H_{NN} \end{pmatrix} \tag{52}$$

and

$$\mathbf{S} = \begin{pmatrix} 1 & S_{12} & \cdots & S_{1N} \\ S_{21} & 1 & & S_{2N} \\ \vdots & & \ddots & \vdots \\ S_{N1} & S_{N2} & \cdots & 1 \end{pmatrix} \tag{53}$$

the desired Hamiltonian in the orthogonal basis is then

$$\mathbf{H} = \mathbf{S}^{-1/2}\mathbf{H}'\mathbf{S}^{-1/2} \tag{54}$$

The final couplings H_{ab} are the elements of the $\mathbf{H}$ matrix, $[\mathbf{H}]_{ab}$. The orthogonalization procedure can sometimes induce drastic changes in the nature of the basis states — e.g. when

two of the nonorthogonal basis states are symmetric with respect to a swap of spin indices, they orthogonalize to a singlet and a triplet state. Since the triplet state has essentially zero coupling to the other singlet states produced, this phenomenon is quite easy to recognize. In any case, at the end of this orthogonalization process, we have obtained electronic couplings H_{ab} in an orthogonal diabatic basis, starting from the nonorthogonal diabatic states and their couplings H_{AB}. Unfortunately, this route for orthogonalization is not unique, and other techniques can be used.[276] The ambiguity here is tied to the fact that diabatic states are themselves non-unique. The differences between different orthogonalized bases is expected to be rather small in physical applications, and the differences vanish entirely when the couplings are used in a CI approach (as discussed in the next section). However, the somewhat fuzzy nature of H_{ab} needs to be kept in mind as we discuss its application.

5.2 Electron Transfer Couplings and Energy Gaps

One of the most important applications of the diabatic coupling is to electron transfer, as H_{ab} plays an important role in computing the Marcus rate (equation (33)). As such, there is a long (and growing) list of alternative schemes for computing the coupling, and we must briefly review a few such expressions before going on to evaluate the CDFT coupling.

Perhaps the most natural way to obtain H_{ab} is to try to extract it from the adiabatic energies of the system. An example of this is given in Figure 26, which shows two generic diabatic energy curves and illustrates qualitatively how H_{ab} splits the two diabats to obtain two adiabats. It is easy to quanify this relationship: at the crossing point, the diabatic states are degenerate and the Hamiltonian is of the form

$$\mathbf{H} = \begin{pmatrix} E & H_{ab} \\ H_{ab} & E \end{pmatrix} \tag{55}$$

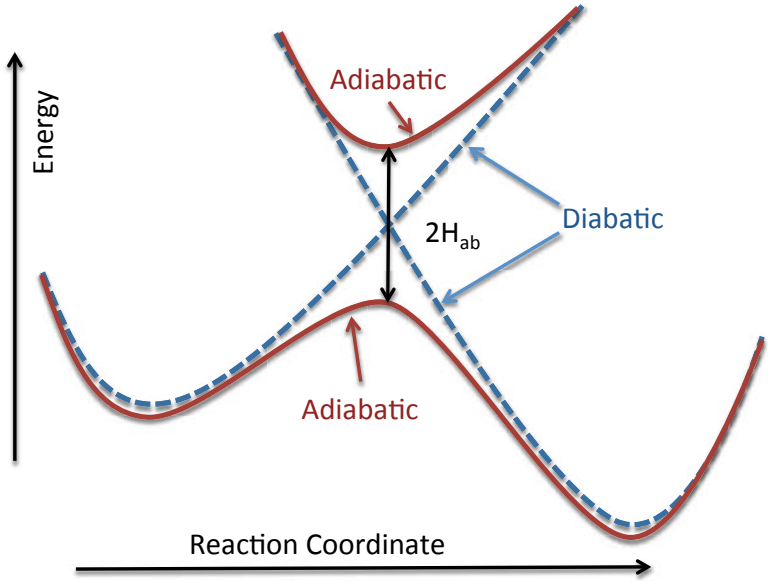

Figure 26: Schematic of the interplay of diabatic states, adiabatic states and the diabatic coupling. Where the diabatic states cross, the adiabatic states avoid one another and the gap between the two adiabats is given by twice the diabatic coupling (H_{ab}). Far from the crossing, the diabats and adiabats are very similar.

which has eigenvalues $E_{\pm} = E \pm H_{ab}$. Clearly, the difference between the eigenvalues is twice the off-diagonal element, so the coupling element is determined as

$$H_{ab} = \frac{E(S_1) - E(S_0)}{2} \tag{56}$$

Thus, for reactions where the two-state approximation is valid, approximations to H_{ab} may be obtained solely from adiabatic energies. At least one of the adiabatic energies is necessarily an excited state energy; it can be approximated using Koopmans' theorem[277] or TDDFT excitation energies,[278] as well as higher-order wavefunction-based methods.[279] This energy-gap method bears a striking resemblance to how magnetic exchange couplings in transition-metal complexes are computed from the energies of the high-spin and broken symmetry states in section 4.

Of course, equation (56) only gives us *one* value of the coupling — the value at the

crossing point. If diabatic state energies are also available in addition to the ground-state energy, we can use that information to compute the coupling at an arbitrary point along the reaction coordinate. One of the simplest such coupling prescriptions relies on the analytical relationship between the diabatic energies, couplings, and the adiabatic energies for a two-state system; when the diabatic states are orthogonal, the coupling between diabats is equal to:

$$|H_{ab}| = \sqrt{(E - E_A)(E - E_B)} \tag{57}$$

where E is the ground state energy and E_A and E_B are the two diabatic energies. The orthogonality assumption can also be relaxed by including the overlap element $S = S_{AB}$ giving:

$$|H_{ab}| = \frac{\sqrt{(E - E_A)(E - E_B)} + S\frac{(E-E_A)+(E-E_B)}{2}}{1 - S^2} \tag{58}$$

where once again a Löwdin orthogonalization has been performed to obtain H_{ab}.[269] We henceforth refer to equation (58) as the mixed adiabatic-diabatic coupling, or just the mixed coupling.

Molecular systems have more than two states; however, a two-state approximation is valid for a multi-state system when the two states considered are energetically well-separated from the other states. In this case, the (full) conversion between adiabats and diabats largely preserves the two-state subsystem and the formulas which are exact for a two-state system are a good approximation for the real system.

In what follows, we will see that despite the apparent theoretical advantages, these methods all perform quite poorly in conjunction with DFT, primarily due to SIE.

5.3 Applications

Given the preceding expressions for the coupling, we now proceed to investigate their accuracy. The square of the electronic coupling is proportional to the rate of transitions between

the two diabatic states via Fermi's golden rule. When considering charge transfer between a spatially separated donor and acceptor, the rate is primarily governed by tunneling, which is expected to decay exponentially with the separation. Thus, one sanity check for any coupling prescription is to verify that it decays exponentially at large separations. The first study of the CDFT coupling (equation (51)) found this decay to be present for a prototypical homonuclear diatomic hole transfer system, Zn_2^+, shown in Figure 27. The behavior was tested for

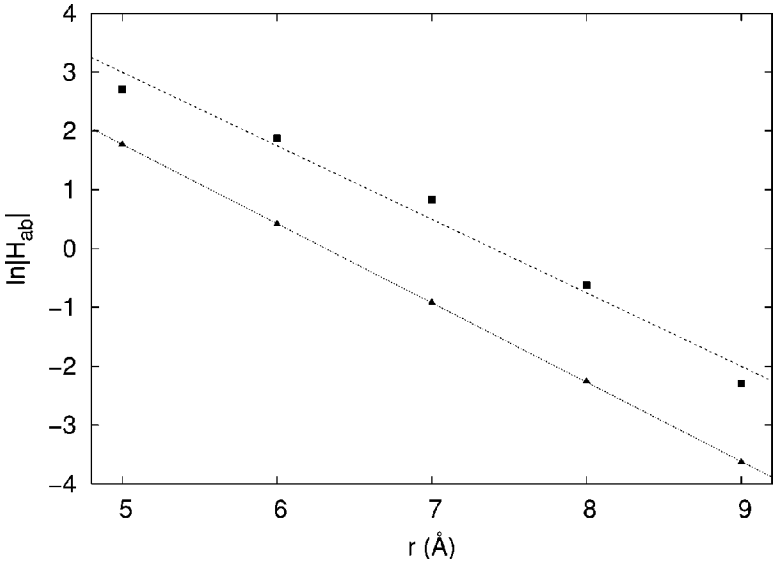

Figure 27: Electronic coupling matrix element $|H_{ab}|$ for hole transfer in Zn_2^+ versus Zn–Zn distance. Straight lines represent best linear fits; squares are the couplings from using Löwdin population and triangles the couplings from using the Becke weight population. Used with permission from reference 54.

two different choices of the charge prescription underlying CDFT; both schemes yield similar decay factors, but the Becke weight population scheme gives consistently smaller couplings. Figure 32 will show that the Becke scheme gives better agreement with other schemes that have been used as reference values, in line with our expectation that real-space population schemes (like Becke's) are more reliable than AO-based ones (like Löwdin's). In any case, this initial application supports the validity of the approximations made to obtain equation (51).

Going a step further, recent theoretical work has used CDFT couplings from equation (51) to classify bridged ferrocene systems as exhibiting through-space coupling or through-bond coupling for a wide variety of bridge moieties, as ilustrated in Figure 28.[265] As the data in Table 8 show, CDFT predicts the qualitatively correct trend of exponential decay of the coupling with distance, while comparison with experimental results suggests that the CDFT couplings only slightly overestimate the couplings.[265] These results argue strongly for the accuracy and efficiency of the CDFT coupling.

At the same time, these mixed valence compounds expose significant problems with the energy gap formulae, as also shown in Table 8. Using either the HOMO-LUMO energy gap or the mixed diabatic coupling gives a gross overestimate of the overall coupling and the wrong distance dependence — the coupling either remains flat or increases with increasing separation! These errors are particularly noticable for the saturated bridges, where the CDFT coupling decays to almost nothing for the longest (12-carbon) bridge, but the other formulae predict unphysically large couplings. The conjugated bridges (which are expected to have some delocalization) are not immune to this form of error, with the values from the mixed coupling formula (equation (58)) growing *larger* as the bridge length increases, while the actual couplings should decrease with increasing separation. Figure 28 gives insight into why the energy gap methods fail. For ferrocenes separated by a twelve-carbon saturated bridge, the HOMO and LUMO are both fully delocalized (unphysically) over the metal centers, which is problematic for functionals with significant SIE. Meanwhile, for long unsaturated bridges, the HOMO and LUMO actually have more amplitude on the bridge than on the donor and acceptor, which is almost certainly incorrect. Indeed, because the HOMO and LUMO are always delocalized, the adiabatic ground-state energy is too low (because of reduced self interaction error), which causes the mixed diabatic coupling to be too large and the HOMO-LUMO gap to be artificially increased (the so-called band gap problem[280]), leading to large couplings from the HOMO-LUMO gap as well.

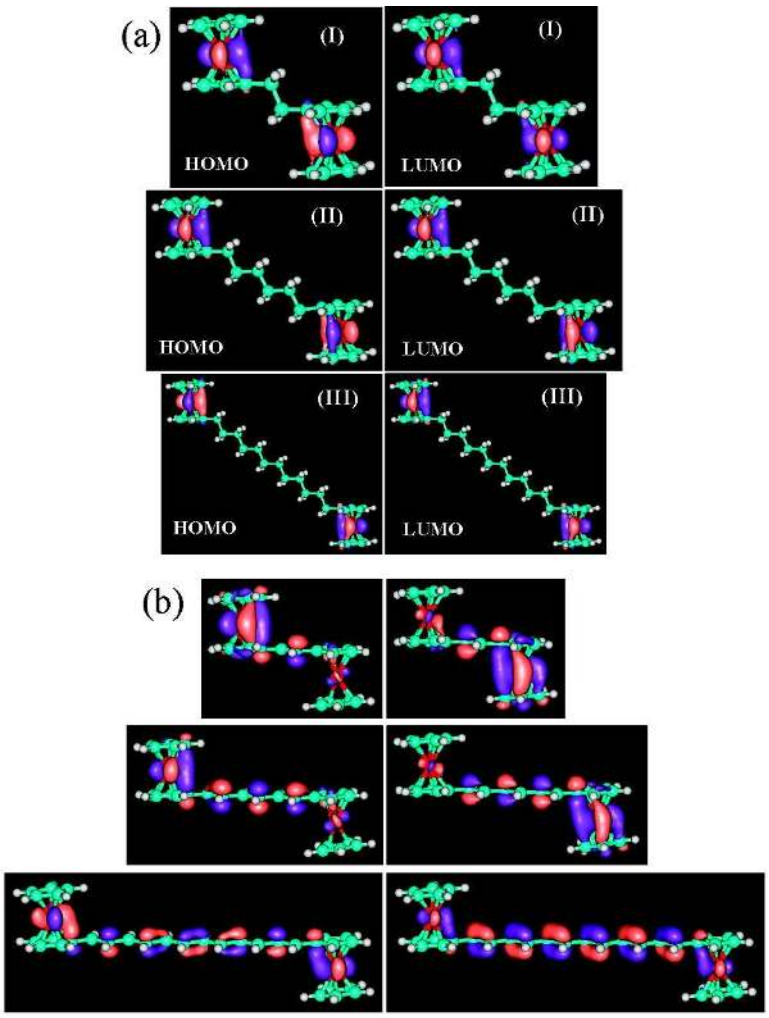

Figure 28: HOMO and LUMO surfaces for series of ferrocene systems with different-length bridges. (a) saturated $(CH_2)_n$ linkages. (b) monounsaturated conjugated linkages. The delocalization of the frontier orbitals is chemically unphysical in (a), leading to couplings that are too large. Used with permission from reference 265.

Fe-bridge-Fe^+	H_{ab} from HOMO-LUMO gap	H_{ab} from eqn (58)	H_{ab} from CDFT
$Fe - Fe^+$	16.6	6.8	3.26
$Fe - CH_2 - CH_2 - Fe^+$	5.5	2.4	0.88
$Fe - (CH_2 - CH_2)_3 - Fe^+$	2.8	13.3	0.15
$Fe - (CH_2 - CH_2)_6 - Fe^+$	1.7	13.9	0.03
$Fe - CH = CH - Fe^+$	14.4	13.8	3.22
$Fe - (CH = CH)_3 - Fe^+$	13.6	18.9	3.42
$Fe - (CH = CH)_6 - Fe^+$	14.2	21.5	1.02

Table 8: Coupling elements for bridged diferrocene systems. CDFT couplings are more physical than those computed using the ground-state DFT energy, which suffers from delocalization error. Data taken from reference 265.

The CDFT prescription for the coupling avoids these errors by using the diabatic states directly. The degrees of localization and self-interaction in both diabatic states are the same, and thus these terms largely cancel when taking energy differences involving just those diabatic states. The above results show that the CDFT coupling (equation (51)) behaves in the ways expected for an electronic coupling element, in contrast to energy-gap-based methods for obtaining diabatic couplings. This result is perhaps a bit surprising in that the less accurate method (i.e. the energy gap prescription) is more rigorous. This discrepancy is primarily attributable to the limitations of commonly-used functionals: it appears that the energy-gap coupling is simply more sensitive to errors in the functional than the total energy is.

It is important to note that the diabatic picture does not always predict an exponential decay — it also lends itself to the Condon approximation that the coupling is insensitive to (transverse) nuclear motion (e.g. relaxation within the donor or acceptor fragment).[281] The availability of CDFT couplings permits investigation of the validity of this approximation for intramolecular electron transfer, by computing the coupling element as a function of the reaction coordinate. Table 9 shows the variation in the electronic coupling along the reaction coordinate for intramolecular charge transfer in the mixed-valence tetrathiafulvalene-diquinone (Q-TTF-Q) anion discussed in section 3. In the anion, the excess electron localizes

on one of the quinone rings, causing some out-of-plane distortion of the structure. Here, as the reaction coordinate moves from q=1 to q=-1 the conformation changes from "electron on left" to "electron on right". As the data make clear, the electronic coupling changes very little over the full domain of the reaction coordinate, showing that the Condon approximation is reasonable for this system.

$q(\pm)$	$\lvert H_{ab}\rvert$
1.0	2.89
0.8	2.95
0.6	3.00
0.4	3.03
0.2	3.05
0.0	3.06
-0.2	3.05
-0.4	3.03
-0.6	3.00
-0.8	2.95
-1.0	2.89

Table 9: The electronic coupling element $|H_{ab}|$ (kcal/mol) for Q-TTF-Q anion as a function of the charge-transfer reaction coordinate. $q = -1$ corresponds to charge fully localized on the left quinone, and $q = 1$ to charge localized on the right. Data taken from reference 54.

5.4 Exciton-CT Coupling

CDFT provides diabatic electronic states, and couplings between them. In some cases, though, it is of interest to compute an electronic coupling between a CDFT diabatic state and an excited state obtained from other means. For example, in photovoltaic cells, one is typically interested in charge separation emanating from an *excited state* of the system.[263] These localized, charge-neutral, excited states are typically referred to as "excitons". Similarly, in light-emitting devices, one is interested in charge recombination events that *form* excitons, which subsequently luminesce. In these situations, the Marcus rate expression (equation (33)) still applies, but either the "donor" or "acceptor" state is itself an excited

state of the system — it cannot be written as the ground state of the system in an alternate potential and is thus not accessible via CDFT. Hence, in computing the H_{ab} coupling element, equation (51) cannot be used because one of the states is not a constrained state. In most cases, the exciton state is well-described by TDDFT, while the charge separated state is well described by CDFT (as illustrated above). We thus require a formula for the coupling that applies when one of the states derives from CDFT while the second comes from TDDFT.

In order to accomplish this goal, we need to be able to associate an approximate wavefunction with a TDDFT excited state. Just as was the case for KS-DFT, this is problematic because TDDFT only provides access to the excited state *density* and not the excited state wavefunction. However, each linear-response TDDFT state can be associated with a sum of Slater determinants

$$|\Psi^{ex}\rangle = \sum_{ia} c_{ia} |\Psi_i^a\rangle \tag{59}$$

The sum runs over singly excited states, with Ψ_i^a being the Slater determinant obtained by taking the ground-state KS wavefunction and replacing occupied orbital i with virtual orbital a. The coefficients $c_{ia} = x_{ia} + y_{ia}$ are simply related to the canonical x and y TDDFT amplitudes.[282] This form for the TDDFT wavefunction reproduces the exact TDDFT transition density, and so in this sense can be thought of as the "wavefunction" for the excited state. Inserting this $|\Psi^{ex}\rangle$ into the CDFT coupling formula, the coupling element then involves *sums* of overlaps and constraint potential matrix elements between the CDFT state and the singly-excited determinants which comprise $|\Psi^{ex}\rangle$.

However, the computational efficiency of the direct route is rather poor: with a sum over $O(N^2)$ singly-excited states and an $O(N^3)$ coupling calculation for each, the overall complexity is $O(N^5)$, which is impractical for large systems. However, the scaling can be reduced to $O(N^3)$ by using a Thouless rotation[283] to convert the sum over single excitations

into a sum of just two determinants. The core idea of the Thouless rotation is to convert the representation of the exciton from a sum of $N_{occ} \cdot N_{virt}$ singly-excited determinants into a difference of two Slater determinants made of slightly perturbed occupied orbitals. Putting

$$\phi_i(\pm\epsilon) \equiv \phi_i \pm \epsilon \sum_a c_i^a \phi_a \tag{60}$$

as these perturbed occupied orbitals, we build the Slater determinants $\Phi(\pm\epsilon)$:

$$\Phi(\pm\epsilon) = \Phi \pm \epsilon \sum_{ia} c_i^a \Phi_i^a + O(\epsilon^2). \tag{61}$$

The TDDFT state is then written as

$$|\Psi^{ex}\rangle = \sum_{ia} c_i^a \Phi_i^a = \lim_{\epsilon \to 0} \left(\frac{\Phi(+\epsilon) - \Phi(-\epsilon)}{2\epsilon} \right) \tag{62}$$

with only two Slater determinants. This procedure is discussed in more detail in reference 262.

These coupling elements are still in the basis of the TDDFT and CDFT states, which are in general non-orthogonal (as the different constrained states were in section 5.1). As before, a Löwdin transformation can convert the states into an orthogonal basis. However, for this system, there is an alternate method available which definitively preserves the labeling of states as exciton or CT. The CDFT population operator $\hat{w}$ — used to define the constraint potential $V\hat{w}$ — provides a measure of degree of charge-transfer, and the eigenstates of $\hat{w}$ form an orthogonal basis for the Hamiltonian.[55] The matrix elements of $\hat{w}$ were used in computing the couplings (equation (51)), so there is minimal extra work in computing them. Solving

$$WC = nSC \tag{63}$$

for the state vectors C which diagonalize the weight matrix W of $\hat{w}$ in the nonorthogonal basis of exciton and CT states yields the orthogonal eigenstates. Transforming the Hamiltonian (and thus the couplings) into this new basis gives the orthogonalized couplings H_{ab}. The eigenvalues n of the weight matrix are also significant, directly assessing the degree of charge transfer in the orthogonal diabats, making clear the distinction between charge-transfer and local exciton states.

As a simple example, the coupling between local exciton states and a charge transfer state has been studied for the triphenylene $\cdots$ 1,3,5-trinitrobenzene system as a function of intermolecular separation.[262] These two molecules were chosen as typical representatives of an organic donor/acceptor interface, where triphenylene acts as the donor and 1,3,5-trinitrobenzene the acceptor. As such, there is a low lying donor→acceptor CT state that crosses three different localized exciton states. From the TDDFT calculations, the desired exciton states are easily identified by examining the the attachment and detachment densities, as shown in Figure 29. The excitons are easily identified as having attachment and

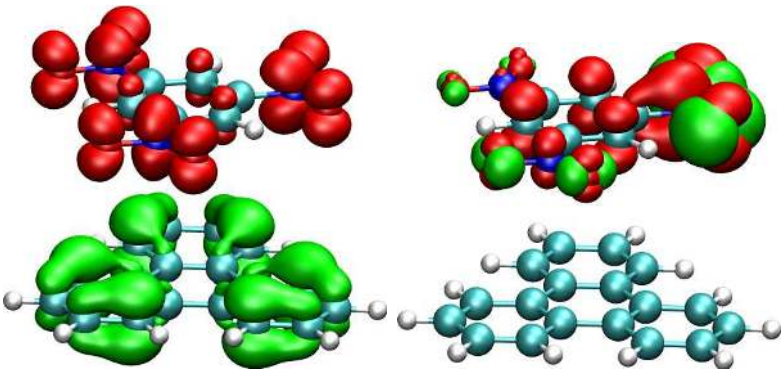

Figure 29: Attachment/detachment density plots for triphenylene:1,3,5-trinitrobenzene that show (a) nonlocal/CT and (b) localized exciton electron densities. The red (green) regions have excess (reduced) electron density compared to the ground state. Used with permission from reference 262.

detachment densities localized on a single molecule, while the CT state has the attachment and detachment densities on different molecules. Choosing only the three lowest exciton

states from the TDDFT calculation and computing the coupling of each exciton to the CT state gives the results in Figure 30. The strong coupling of the third excited state to the

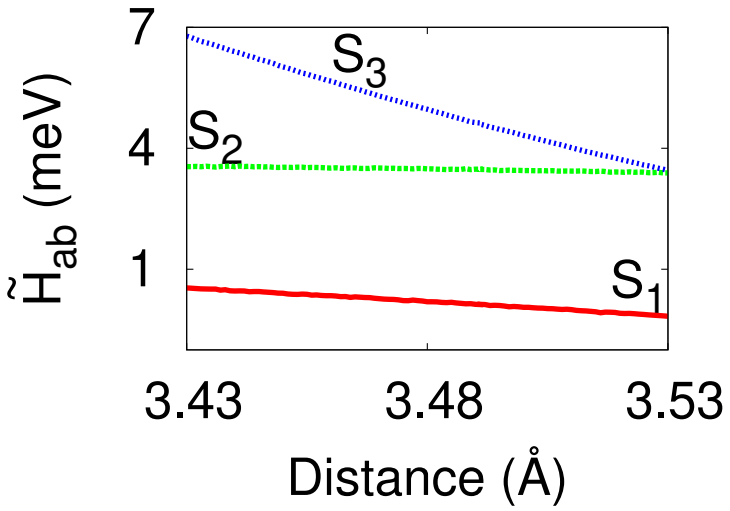

Figure 30: The electronic coupling between the CDFT CT state and three locally-excited TDDFT states for triphenylene $\cdots$ 1,3,5-trinitrobenzene. The coupling to the first excited state is quite small, and the coupling to the third shows strong variation with separation on this length scale. All the couplings tend to zero at large separations. Used with permission from reference 262.

charge-transfer state indicates that it is likely to be a significant contributor to charge separation for this system, whereas the first excited state has a much smaller coupling and should be less important, showing that it is not always sufficient to only consider the first exciton state in assessing the performance of OLED or photovoltaic systems. For this organic heterodimer, the nonadiabatic transition from local exciton state to diabatic charge-transfer state provides insight into the application of the materials in photoelectronics, providing a mechanism by which to understand the relaxation of a photoexcitation into free carriers or the reverse process.[262]

5.5 Alternative Coupling Methods

The desire to study chemistry in terms of diabatic states and the couplings between them is far from a new idea, being well-understood for several decades at least.[284–287] Strictly diabatic states which diagonalize the nuclear momentum coupling vector are not possible in general,[286] but this has not prevented a proliferation of approximate routes to diabatic states over the years.[154–156,244–261,288–290] In this section, we briefly describe a few often-used approaches to diabatic couplings in order to place the CDFT coupling formula in context.

One of the earliest methods used to obtain approximate diabatic states relies on broken-symmetry (BS) solutions of the SCF equations.[291,292] As discussed in Section 4.2, when treating magnetic or diradical systems, unrestricted KS calculations will sometimes converge to solutions in which the α and β orbitals differ. These states are not spin eigenstates (hence the broken symmetry moniker) but perhaps more importantly, they typically involve localization of spin and/or charge on certain parts of the molecule. These BS states can thus play a role very similar to CDFT states. The interpretation of BS states as diabats is tenuous, as it is not even possible to be certain that a given system will have BS KS solutions at all. For example, in the classic case of H_2 dissociation, the KS equations have no BS solutions at short bond lengths. However, past a critical distance (the Coulson-Fischer point) BS solutions appear and are, in fact, energetically lower than the spin-restricted solutions. In this sense, CDFT states should be thought of as a more reliable BS state because one can always generate the physically desired state using a constraint, while it is not clear if the same state will exist in the BS approach.

Nonetheless, the orbitals (and thus wavefunctions) of these BS states can be used to compute coupling matrix elements of the Hamiltonian, as was done in the early work of Farazdel *et al.* for intramolecular electron transfer using BS Hartree-Fock states.[291] Below, we will summarize their results, noting that the relevant BS determinants can come either from Hartree-Fock or Kohn-Sham calculations. For BS states, one directly computes the

electronic coupling matrix $H_{AB} = \langle \Psi_A | H | \Psi_B \rangle$ including both the one- and two-electron contributions. The algebra for these matrix elements in terms of non-orthogonal determinants can be worked out with complexity similar to a DFT energy evaluation.[293] Once again, the couplings need to be orthogonalized to obtain the physical coupling H_{ab}, and this can be done either using the Löwdin prescription or by finding the eigenvalues of the Hamiltonian in the diabatic basis and using the energy gap formula (equation (57)). We note that when this direct coupling formula is used for KS states, one is once again implicitly assuming the KS determinant is the true diabatic wavefunction, which is in general not justified. Nonetheless, the direct coupling formula and the CDFT coupling capture much of the same physics. Consider the direct coupling between CDFT KS states ($H_{AB} = \langle \Phi_A | \hat{H} | \Phi_B \rangle$) compared against CDFT couplings from equation (51). For the simple molecule LiH, Figure 31 compares the behavior of these two prescriptions for the coupling between the orthogonalized ionic (Li^+H^-) and neutral states.[294] The couplings are clearly in qualitative agreement and exhibit the same exponential decay behavior.

Directly computing the coupling element between diabatic states is far from a unique route to couplings; on the other end of the spectrum are methods that compute diabatic couplings directly from a set of adiabatic states. There are a large number of such methods[245,248,249,253,254,258,259] of which one deserves special discussion at present: the generalized Mulliken-Hush (GMH) prescription.[155,256] GMH is widely used for electron transfer problems, and it is often taken as the definitive reference method for computing diabatic couplings (see Figure 32). We therefore spend a bit of time discussing this alternative. The core idea of the GMH method is to define diabatic states as the eigenstates of the dipole moment operator in the basis of the low-lying adiabatic states. This makes physical sense: the eigenvalues of the dipole will be the extreme values and the desired neutral and CT states will have very small and very large dipole moments, respecively. Thus, given a set of N adiabatic states (e.g. from CASSCF theory), GMH first constructs matrix elements of the dipole operator

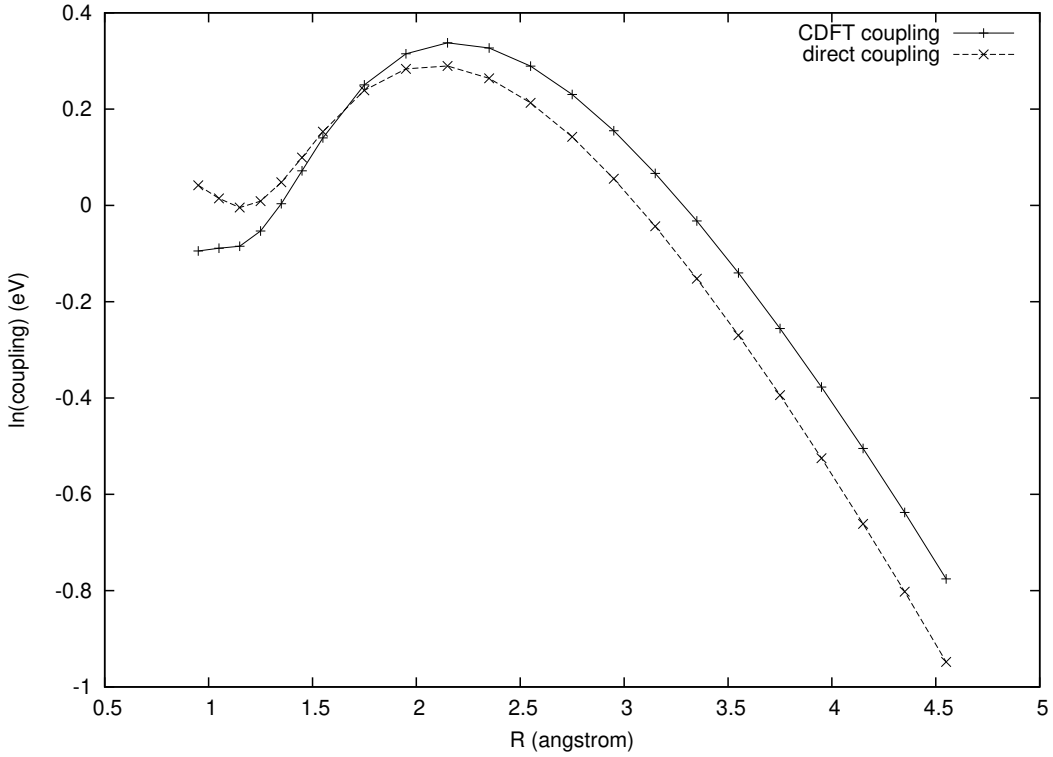

Figure 31: The coupling (in eV) between the lowest singlet states of LiH, calculated using the standard CDFT formula (equation (51), "CDFT coupling") and by directly taking the matrix element of the Hamiltonian ("direct").

and then diagonalizes this matrix in the basis of the adiabatic states.[155,256] GMH also allows for multiple diabats to have charge localized on a given site, which are forced to be locally adiabatic with respect to each other as the assumption of zero transition dipole moment is not reasonable in that case.[256] The GMH diabats are automatically orthogonal, and so the diabatic coupling is obtained by transforming the diagonal adiabatic Hamiltonian into the basis of dipole eigenstates; the physical coupling(s), H_{ab}, are just the off-diagonal elements of the transformed Hamiltonian. For two-state symmetric systems, GMH reproduces the energy gap method.

The GMH and CDFT couplings are very different in execution: the former requires some pre-existing route to adiabatic excited states (e.g. TDDFT) while the latter only requires ground state calculations in alternative potentials. In GMH, diabatic states and their couplings are deduced from the adiabats, while in CDFT diabatic states are constructed directly. Finally, in GMH there is a clear route toward exact diabatic couplings (by improving the adiabatic excited states) while in the latter the route toward exact couplings is somewhat murky. The primary reason GMH (and related methods) deserve mention here is that, like CDFT, GMH defines the diabatic states with relation to an operator. That is to say, in GMH one chooses diabatic states as eigenstates of the dipole moment, much as in CDFT one chooses diabats as states with defined charge. Thus, while the technical operations involved are quite distinct, the two methods share a common picture of diabatic states as being "special" with respect to some physical operator.

When producing multiple adiabatic energies is too expensive, cheaper alternatives to coupling elements are available. Making the approximation that only the HOMO of the donor and the LUMO of the acceptor contribute to the coupling drastically simplifies the computation of a direct coupling element between diabats: the coupling is then computed as the matrix element betwen those two orbitals; this is known as the fragment orbital (FO) method. Using single orbitals necessitates treating the donor and acceptor as independent

systems (as otherwise the distinction between donor and acceptor orbitals is dubious at best), so they cannot respond to each others' environment — all information about polarization and intermolecular interactions is thus lost. In practice, the LUMO of the acceptor is computed as the HOMO of the reduced acceptor, so that occupied orbitals are used on both sides of the matrix element.[272] By treating donor and acceptor as separate systems, it is easy to enforce the charge (spin) localization involved in the reactant and product states — the component subsystems are just systems with (half-)integer charge (spin). Difficulties arise from the use of separate systems, though, if there are bonds between donor and acceptor, or if there is significant mutual polarization between donor and acceptor.[272] Figure 32 shows the behavior of the FO-DFT coupling as a function of internuclear separation for the zinc dimer cation system from section 5.3, as well as CDFT couplings and the Generalized Mulliken-Hush (GMH) method described below. The FO-DFT method has a noticeably different

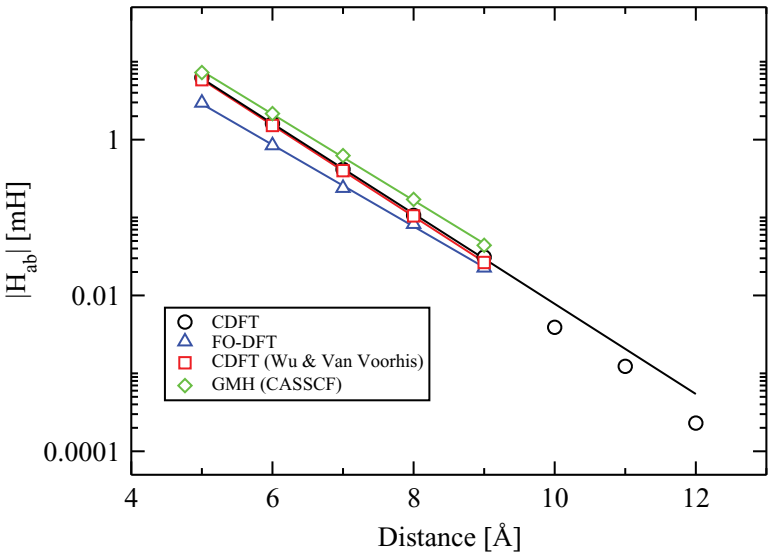

Figure 32: GMH, CDFT (plane-wave), CDFT (AO), and FO-DFT methods compared for diabatic coupling elements decaying with separation for the zinc dimer cation. Reprinted with permission from reference 272.

exponential decay factor than the other methods (as seen by the slope on the graph), as well as a substantially smaller coupling magnitude (up to a factor of two, more pronounced at

smaller separations). This discrepancy is attributed to the lack of polarization in the FO-DFT orbitals, as the HOMO of the CDFT system is found to be slightly polarized towards the acceptor.[272]

As in Figure 32, the GMH method is frequently used as a reference for comparison with other routes to diabatic electronic coupling elements. In the data presented there, the decay constants for zinc dimer cation placed the GMH value between the FO-DFT and CDFT-determined decay constants, and the difference in the magnitude of the coupling between GMH and CDFT is attributable to the differing definitions of diabatic states.[272] Nonetheless, GMH calculations require some care to obtain meaningful results, as they take as input multiple adiabatic states (wavefunctions), and the determination of adiabatic excited states is much less robust than the existing treatments for adiabatic ground states. For example, the commonly-used (for small systems) CASSCF approach is sensitive to the choice of active space and the number of states included in the state averaging;[295,296] furthermore, the GMH method can require a determination of which diabats are localized on the same site, a decision which is hard to make programmatically. Many of these difficulties can be overcome by defining the diabatic states as many-electron extensions of Boys localization.[245] This approach allows a GMH-like scheme to be applied transparently to large active spaces and multiple fragments.

Yet another alternate route from nonorthogonal fragment or CDFT states to diabatic couplings is taken in the work of Migliore,[297,298] which uses the adiabatic ground state to avoid directly computing coupling elements. This is similar in spirit to equation (58) but avoids using the ground-state energy (which is known to be unreliable for DFT transition states). Given diabatic states A and B (assuming a two-state framework), some algebraic manipulation shows that the coupling between the states is related to their overlap (S_{AB}), the energy gap between the diabatic states ($\Delta E_{AB} = E_A - E_B$) and the overlap of each

diabat with the ground state ($a \equiv \langle \Psi_A | \Psi_0 \rangle$ and $b \equiv \langle \Psi_B | \Psi_0 \rangle$) via:[298]

$$H_{ab} = \left| \frac{ab}{a^2 - b^2} \Delta E_{AB} \left(1 + \frac{a^2 + b^2}{2ab} \right) \frac{1}{1 - S_{AB}^2} \right| \tag{64}$$

Results for this coupling formula as applied to hole transfer in a π-stack of two DNA bases show that the coupling is relatively independent of basis set size, and compares reasonably with GMH and CASSCF-based methods.[298] Effectively, by replacing the adiabatic energy in equation (58) with the overlaps a and b (which contain the same information) one arrives at an expression that appears to be somewhat less sensitive to SIE effects. There are reasons to suspect that equation (64) is not completely immune to SIE, however; note that for the mixed valence systems in Figure 28 $a \approx b$ so that $a^2 - b^2 \approx 0$ and the coupling of equation (64) becomes potentially divergent for non-vanishing ΔE_{AB}. Thus, equation (64) should be used with some caution.

5.6 Illustrations

5.6.1 Electron Transfer

One of the most obvious uses of the diabatic coupling is in the prediction of electron transfer rates, in accord with the Marcus rate expression of eq (33). For example, we can return to the FAAQ dyad discussed in section 3.3. There, we saw that CDFT molecular dynamics in explicit solvent was capable of correctly describing the free energy landscape for charge recombination from the CT excited state (FA^+-AQ^-) to the ground state, including the accurate prediction of the driving force (ΔG) and reorganization energy (λ). In order to complete the Marcus picture, then, we need the diabatic coupling H_{ab} between the states, which is easily obtained using eq (51). However, since the reaction is occurring in a fluctuating environment, we cannot speak of only a single value of H_{ab} — rather, we need to speak of the *distribution* of H_{ab} values in the ensemble of reactant and product configurations. To

Configurations	$\langle H_{ab} \rangle$	σ_H
	Gas Phase	
Neutral	0.90	0.15
CT	0.73	0.18
	DMSO	
Neutral	0.61	0.12
CT	0.25	0.06

Table 10: Mean electronic couplings and deviations for the neutral and CT configurations of FAAQ in the gas phase and in DMSO solution. Energies in eV. Taken from reference 183.

put it a different way, we do not want to make the Condon approximation at the outset. If there are significant variations in the coupling as the reaction progresses, we want to see this, which requires re-computing the coupling at every snapshot of the simulation. This can be done, and results in the data in Table 10. Several things are clear from the data. First, the Condon approximation is reasonably accurate in these simulations, with the coupling fluctuating by only 10-20% for a given state. This is reassuring, as it means the Marcus picture of ET being driven by energy gap fluctuations (rather than fluctuations in H_{ab}) is likely valid for this molecule. Second, it is clear that the presence of solvent reduces the magnitude of the coupling, sometimes significantly. This point is important because it calls into question the standard protocol of using gas phase couplings in condensed phase simulations.[244,299] Finally, it is interesting to note that the couplings in the neutral ground state and the CT excited state are different, suggesting that the H_{ab} values for charge separation are somewhat different than those for charge recombination.

Overall, the couplings above overestimate the experimentally deduced couplings by about fivefold, which is not terrible agreement given the exponential sensitivty of H_{ab} to distance. Moving forward, we expect to see significant advances in the understanding of condensed-phase ET rates as CDFT becomes more widely applied.

5.6.2 Triplet Energy Transfer

One can use diabatic states to discuss energy transfer as well as electron transfer. In particular, CDFT offers a clean description of triplet excitation energy transfer (TEET). TEET is thought to play a role in photoprotection of the photsynthetic light harvesting complex; triplet excitations on chlorin moieties are efficiently transferred to neighboring carotenoids, preventing oxidative damage.[300,301]

In general, to predict the rate of TEET using the Marcus expression (eq (33)) one requires reactant (product) diabatic states where the triplet is localized on the donor (acceptor). These diabatic states are readily accesible in CDFT by constraining the spin, as discussed in section 4. From this point, the manipulations are strictly analogous to the case of electron transfer — one can define a driving force, reorganization energy and coupling term, and for the present we will focus on the coupling. The usual CDFT coupling formula of eq (51) applies to TEET, as do the approximate methods of eqs (57) and (58). Of course, the adiabatic state used for the triplet system will be the lowest triplet state, but otherwise the manipulations are strictly analogous.[269,302] For consistency with the literature, we refer to the TEET coupling from equation (56) as the "splitting method", and also use the mixed coupling of equation (58). Figure 33 shows the couplings computed by these methods for a stacked pair of formaldehyde molecules. Results for the mixed coupling applied to CHF states are notably absent from the plot, as these numbers are much larger than those of the other methods, *rising* from 3000 to 5000 meV as the distance increases! The CDFT mixed coupling results (shown) are also non-physical, with the coupling not decaying to zero at infinite separation (the singularity is just the sign of the coupling changing, on the log scale). The enormous errors for this model are consistent with the poor behavior seen when using the energy gap expression for electron transfer (cf Figure 28). For TEET, the unphysical results can be closely tied to fractional spin error, analagous to the fractional charge error frequently discussed in the context of DFT's self-interaction error.[302] By contrast, the direct

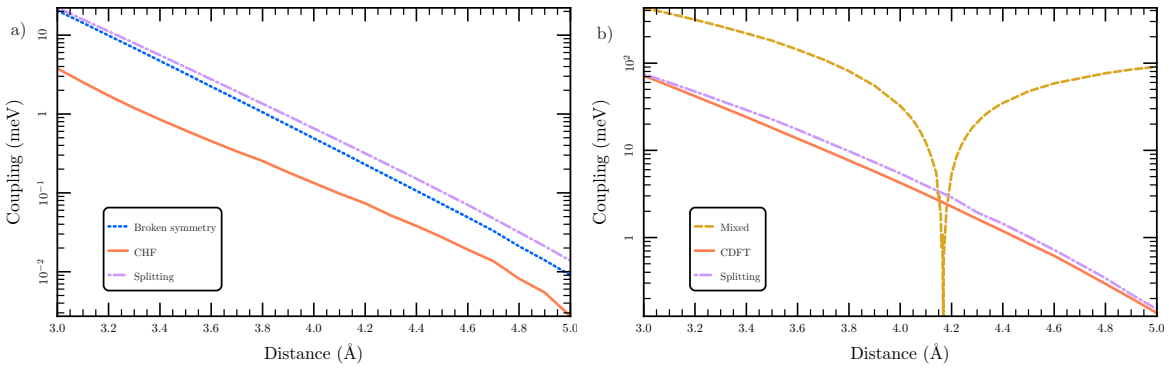

Figure 33: Triplet energy transfer coupling elements for stacked formaldehyde molecules using several different methods. (a) HF, with the coupling between broken symmetry states, CHF states, and the splitting method as applied to CIS excited-state energies. (b) PBE, with the CDFT coupling, mixed coupling, and splitting method as applied to TDDFT excited states. Adapted with permission from reference 269.

methods for computing the coupling (CDFT and BS) are successful at producing couplings of the proper magnitude and with the proper exponential decay as a function of distance. In particular, for PBE the CDFT results very closely parallel the splitting results, which are equivalent to the GMH predictions for this case.

5.6.3 Charge Transport in Organic Semiconductors

Organic semiconductors (OSCs) are a promising class of new materials. In an OLED device, they can be used as the active element in thin, efficient and flexible displays.[303] In a photovoltaic cell, they can be used as inexpensive, large area elements for converting solar energy into useful electricity.[304] In both of these applications, the ability of the material to transport charge (electrons and/or holes) is crucial to device performance, and improving the charge mobilities in OSCs is an ongoing area of research.[305] When used in conjunction with QM/MM simulations, CDFT is an extremely promising tool for studying charge transport in these soft, amorphous systems, as illustrated in Figure 34 for the particular example of a semicrystalline OSC composed of tris(8-hydroxyquinolinato)aluminum (Alq_3).[160] On a large length scale (e.g. tens of nanometers) the structure of the material is modeled using

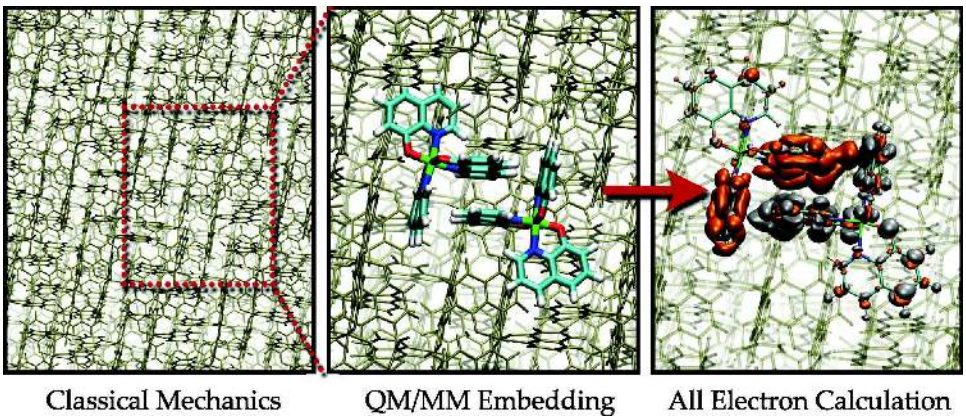

Figure 34: Cartoon illustration of the QM/MM method. Left: many unit cells of the bulk material form the MM region. Center: A small QM region is selected within the simulation box. Right: The electronic structure of the QM region in the electrostatic environment of the surrounding molecules. Used with permission from reference 160

molecular mechanics. One then selects a few (e.g. one or two) molecules from the solid and performs QM/MM calculations to determine the desired parameters (e.g. exciton energy, reorganization energy, coupling...). Finally, one repeats this process hundreds or thousands of times at thermally sampled configurations to obtain ensemble averages. In this manner, CDFT combined with QM/MM simulations provides a means to describe electron dynamics in complex environments at a moderate computational cost.

Charge transport in these materials is thought to proceed via a "hopping" mechanism. Basically, one envisions mesoscopic diffusion arising from a series of electron-transfer reactions between nearby molecules (or even within molecules, in the case of polymers). Each of these electron transfer events is governed by the Marcus rate expression, and this rate in turn is controlled by the electronic coupling. Thus, for electron (hole) transfer, we desire coupling elements of the form $\langle A^- A|\hat{H}|AA^-\rangle$ ($\langle A^+ A|\hat{H}|AA^+\rangle$), where $A \equiv \mathrm{Alq_3}$ in this case. Since CDFT is used to localize the carrier on the appropriate molecule, equation (51) applies directly to determine these couplings. Applying this prescription to compute electron and hole transfer couplings in $\mathrm{Alq_3}$ results in the distributions shown in Figure 35.[160] Here, the couplings are distinguished by the approximate lattice vector along which transfer

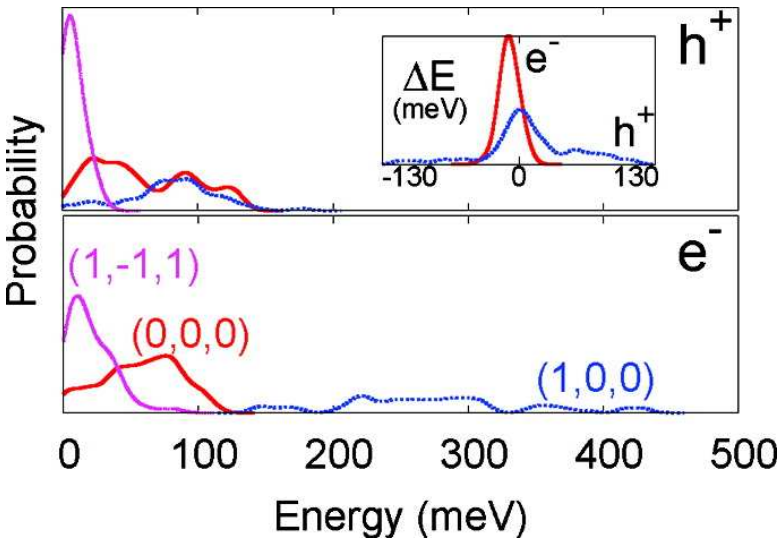

Figure 35: The electron and hole coupling distributions. Distributions are shown for nearest neighbors along three different lattice vectors. The inset shows the effect of smearing the MM charges from point charges into Gaussian distributions. Used with permission from reference 160.

occurs. There is clear separation between the different lattice vectors, indicating that over the course of the simulation (several ns) a given pair of molecules tends to retain the same relative orientation. The latter observation is consistent with the known glassy behavior of most OSCs. The second obvious feature is that electron transport accounts for most of the stronger couplings, with the holes being clustered more densely at smaller couplings. The existence of very large couplings suggests that electron transfer (and thus electron transport) should be more facile than hole transfer (and thus hole transport) in Alq_3. This prediction is consistent with the experiments, which find the electron mobility in Alq_3 is 100x as large as the hole mobility.[305] Indeed, the electron couplings are large enough to suggest that electron transport might occur via delocalized states (band-like transport), which would represent a fundamental shift in the understanding of this material.

The simulations above on Alq_3 are illustrative of how CDFT QM/MM can be used in OSCs, but really only represent a foretaste of the capabilities of the method — similar calculations can be used to evaluate CT state eneries, charge separation and recombination

rates, absorption and emission spectra and a host of other important material properties. The main impediment to progress is the disorder of the systems, which makes computing the relevant properties time-consuming. But as computational power increases, it seems certain that simulations of this type will guide the microscopic understanding of OSCs.

5.7 Future Work

In the solid-state and solution, for charge, singlet, and triplet energy transfer, diabatic couplings cotrol the flow of charge and energy between localized states. The results summarized above suggest that the CDFT formula for this coupling (equation (51)) gives an accurate and computationally reasonable approximation to this important quantity. However, the situation is far from perfect.

First, it is extremely difficult to get theory and experiment to agree to better than an order of magnitude for H_{ab}. Sometimes the theory is too high, sometimes too low, and the couplings tend to have a worryingly strong dependence on the basis set and the quality of the underlying wavefunction. Some prescription that gives consistent agreement with experiment is clearly desirable.

Second, there are cases where the CDFT coupling itself returns unphysical values. In some cases (cf Table 1) we can understand these errors as arising from a poor choice of atomic populations or a catastrophic failure of the underlying functional. However, occasionally the wavefunctions look qualitatively correct and yet still the couping is off by an order of magnitude or more. It is not clear what causes this unusual behavior. A fundamental understanding of these issues may involve decomposing different contributions to the coupling, as has recently been done for diabatized CIS states.[306]

Finally, it would be extremely useful to have analytic gradients of the CDFT coupling (eq (51)) as a function of nuclear position. Among other things, these gradients would allow us to further explore the validity of the Condon approximation and (in conjunction with the

CDFT-CI method described in the next section) make it possible to perform excited state molecular dynamics for low-lying electronic excited states.

The above wish list of future improvements notwithstanding, the CDFT coupling provides a useful tool for the analysis of charge and energy transfer in real problems and completes the diabatic picture that naturally arises from applying density constraints to the system.

6 Parameterizing Model Hamiltonians with CDFT

In the previous section, we saw how to treat CDFT states as diabatic states and compute diabatic couplings between them. Combined, these allow for construction of a complete diabatic picture of a system, accounting for the entire electronic Hamiltonian, by mapping the full N-electron system into a (much much smaller) diabatic basis.[55] Condensing the full system into an easily-computed small basis is a classic example of using a model Hamiltonian to describe a complex system, and in this respect CDFT shares many features with empirical valence bond theory[156,307] and Van-Vleck transformations in multireference theories of correlation.[308] Model Hamiltonians also abound in the computational sciences, with a great variety of functional forms that are each largely designed for a particular class of physical system: Hubbard[309,310] and Pariser-Pople-Parr (PPP) models[311,312] for π-conjugated molecules; LDA+U[313] and dynamical mean field theory[314] for localized orbitals in metals; Heisenberg models for magnetic systems;[191] exciton models for photosynthesis.[315] When using a model Hamiltonian form to describe a physical system, it is usually desirable to use *ab initio* data to parameterize the model so as to have a numerical connection with the actual physics. The relationship between *ab initio* theory and model form sometimes grows quite intertwined, as in the *ab initio* tight binding method[316,317] and dynamical mean-field theory.[314] In many cases, the underlying physics captured by a model Hamiltonian can be probed using CDFT, whether by producing a particular spin configuration of a magnetic system, adding extra charge to a single site to probe the Coulomb repulsion, or adding static correlation to a reaction transition state, or even combinations of these effects. Due to the diverse and varied nature of both applications and methodology, it is easiest to arrange these applications by the physical problems they address: charge hopping and delocalization,[318–321] spin systems,[225,322,323] strong correlation,[55,132] and electronic excited states.[47,324]

6.1 Charge Hopping

Broadly speaking, conduction is usually modelled in one of two ways: by invoking delocalized states, as in the band theory of metallic conduction[325] or using localized states in the hopping formalism.[326] Both models arise out of the same tight-binding (TB) model in which electrons occupy fixed sites that have both an energy ϵ and also a coupling t_{ij} to other sites;

$$H = \sum_i \epsilon_i c_i^\dagger c_i + \sum_{ij} t_{ij}(c_i^\dagger c_j + c_j^\dagger c_i) \tag{65}$$

where the $c^\dagger$ and c operators are the standard second-quantized creation and annihilation operators. Within chemistry, this model is more commonly referred to as extended Hückel theory. The relative magnitudes of the energy and coupling determine whether hopping or band transport dominates.[325] When $t_{ij}/(\epsilon_i - \epsilon_j)$ is large, delocalization results; localized "hopping" transport occurs when $t_{ij}/(\epsilon_i - \epsilon_j)$ is small. The latter regime is typically referred to as Anderson localization.[327]

Now, the tight binding approximation completely neglects electron-electron interaction, which will clearly influence charge transport. The Hubbard Hamiltonian adds the on-site electron repulsion terms to the TB formula:

$$H = \sum_i \epsilon_i c_i^\dagger c_i + \sum_{ij} t_{ij}(c_i^\dagger c_j + c_j^\dagger c_i) + \sum_i U_i \frac{n_i(n_i - 1)}{2} \tag{66}$$

where $n_i \equiv c_{i,\alpha}^\dagger c_{i,\alpha} + c_{i,\beta}^\dagger c_{i,\beta}$. Most notably, this Hubbard model is the basis for the LDA$+U$ method.[328]

In the above model Hamiltonians, ϵ_i and t_{ij} are single-particle terms, with a variety of different routes for approximation from *ab initio* data.[56,61] In particular, it is quite common to derive effective values of ϵ and t directly from the KS Hamiltonian.[79] Meanwhile, the most reasonable route to the on-site repulsion term U is provided by CDFT. Specifically, because

U_i penalizes only states where site i is doubly charged, we can easily probe U_i with CDFT by increasing the charge on the site in question. In particular, if the Hubbard expression is correct, the dependence of the change in total energy (ΔE) due to a change in the number of electrons (ΔN_i) should be approximately quadratic:

$$\Delta E = \alpha(\Delta N_i)^2 + O((\Delta N_i)^3) \tag{67}$$

The linear term vanishes irrespective of the approach because of charge equilibration in the ground state: if dE/dN_i was non-zero, the system could lower its energy by adding (or subtracting) electrons from the ith site. Thus, both the model Hamiltonian and an *ab initio* energy will vary approximately quadratically with the charge on a given atom. Further, for the Hubbard model, the magnitude of α will depend strongly on U; large U will tend to lead to large α. Thus, by comparing $\Delta E(\Delta N)$ from CDFT calculations with the corresponding Hubbard results, "ab initio" values of U can be obtained.

This prcedure is illustrated in fig 36.[318] Here the U parameters for polyyne are extracted by varying the charge on one of the carbons. Clearly, the parabolic approximation is excellent, supporting the use of the Hubbard model for this linear chain. It is also interesting to note that HF and DFT give essentially identical model parameters for this system.

One can of course use the same procedure to treat other molecular wires, such as the technologically more relevant case of polyacetylene.[329,330] Here, the carbon backbone is nonlinear, so there are three structural isomers to consider: the all-*trans* form, as well as the *cis-trans* and *trans-cis* isomers, which differ in whether the long or short bonds are parallel to the molecular axis. Meider and Springborg computed Hubbard parameters for these three isomers with the standard parabolic fit to obtain U.[319] These simulations went further, exploring whether the long-range electron-electron interactions neglected in the Hubbard model were relevant for the polyacetylene systems. To this end, they also parameterized an

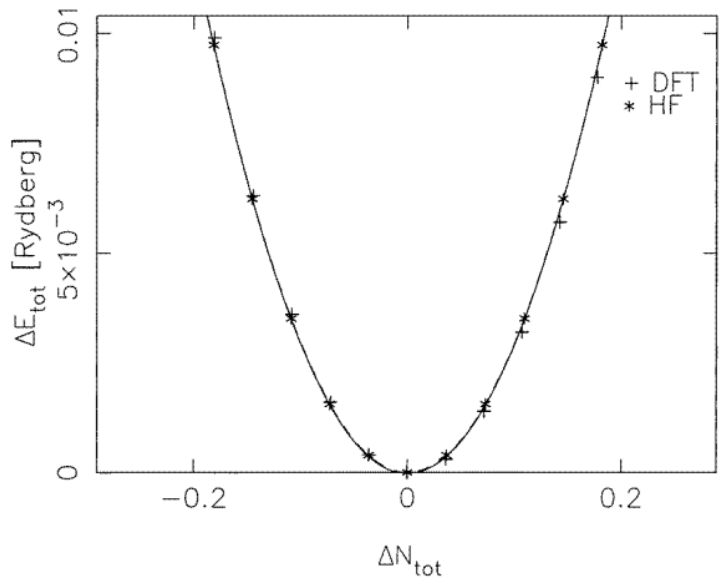

Figure 36: Finding U for an idealized carbyne (C $\equiv$ C$-$C $\equiv$ C$-\cdots$) by fitting $\partial^2 E/\partial \Delta N^2$ to a parabola. Constrained DFT results from calculations with LMTOs with $r_{\mathrm{MTS}} = 1.187$ au and bond lengths 2.375 and 2.70 au, in a basis with two sets of s, p, and d functions per atom. Four carbon atoms were included in the simulation cell, with periodic boundary conditions. "HF" is for calculations in a finite model system with eight carbons. Taken from reference 318.

Parameter	all-*trans*	*cis-trans*	*trans-cis*
$t_{n,n\pm1}$	3.35,2.88	3.44,2.59	3.14,2.86
$t_{n,n\pm2}$	-0.25	-0.16	-0.18
U	10.6	10.5	9.9
U_{nn}	0.2	0	1.0

Table 11: Hubbard parameters for the three isomers of polyacetylene, in eV. "*cis-trans*" has the short (double) bonds parallel to the polymer axis, and "*trans-cis*" has the long (single) bonds parallel to the axis. The two values given for the nearest-neighbor hopping integrals correspond to the shorter and longer bonds, respectively.

extended Hubbard model that adds Coulomb interactions between nearest-neighbor sites:

$$H = \sum_i \epsilon_i c_i^\dagger c_i + \sum_{ij} t_{ij}(c_i^\dagger c_j + c_j^\dagger c_i) + \sum_i U_i \frac{n_i(n_i-1)}{2} + \sum_i U_{nn} n_i n_{i+1} \tag{68}$$

Once again a numerical fit to the total energy as a function of (constrained) charge variation on a site is used to determine the values of the U_i and U_{nn} parameters, though as U_{nn} is the coefficient for a joint variation of population on two adjacent sites, a two-dimensional fit is needed with diagonal and cross terms.[319] As shown in Table 11, the computed values for U_{nn} are quite small, suggesting that the Hubbard model is a good approximate Hamiltonian for polyenes, as well. Interestingly, though, while the Coulomb repulsion is local, the longer-range next-nearest-neighbor hopping terms $t_{n,n\pm2}$ are large enough to affect the band structures of the polyacetylene isomers.[319]

Hubbard-like models are equally useful in understanding bulk systems, especially for high-T_c superconductors where the regions of parameter space that apply to the superconducting phase are not well-known. CDFT has been applied in this context to understand the electronic structure of the superconducting phase of lanthanum cuprates.[321] Here, the conduction is thought to occur between the copper d orbitals with the oxygen p orbitals moderating the conductance either through charging or superexchange. Thus, to model this system one requires three extended Hubbard parameters (U_d, U_p and U_{dp}) which require various constraint potentials to be applied to copper and oxygen (specifically using eq (2)).

For example, applying a fixed potential shift of 0.2 Hartree to the copper d orbitals in a 2×2 supercell of La_2CuO_4 gives the results in Figure 37.[321] The d DOS changes dramatically with the shift, with significant contribution being pushed past the Fermi level in comparison to the unconstrained case. Indeed, the integral of the d density is reduced by 0.370 electrons, but 0.144 electrons are gained in the $s + p$ channels, indicating that some 40% of the screening of the perturbation is on-site. Capturing the relevant charge response and screening effects is a delicate matter, but ultimately the authors were able to find a single set of Hubbard parameters that accurately reproduced the CDFT charge fluctuations: U_d=10.5 eV, U_p=4 eV and $U_{pd} = 1.2eV$. These parameters in turn place some important constraints on contemporary models of high-T_c superconductivity. Approaches of this type are quite closely related to the widely used LDA + U approach,[72] which we consider more closely in section 7.1.

6.2 Spin Models

The spin states of open-shell systems are perhaps the most obvious case where a model Hamiltonian could be useful. Here one has a manifold of nearly degenerate spin states that are energetically separated from all the other excited states of the system. It is therefore natural to develop models in which all the extraneous degrees of freedom (e.g. charges, orbitals, electron repulsion integrals, etc.) are integrated out and only the relevant spin degrees of freedom remain. Of course, these reduced Hamiltonians contain parameters that must be determined, and once again CDFT can play an important role in this process.

As a first example, consider the Heisenberg Hamiltonian (cf section 4)

$$\hat{H} = -2 \sum_{A<B} J_{AB} \, \hat{\mathbf{S}}_A \cdot \hat{\mathbf{S}}_B \tag{69}$$

As we have seen, CDFT does an excellent job of determining the exchange couplings J_{AB}

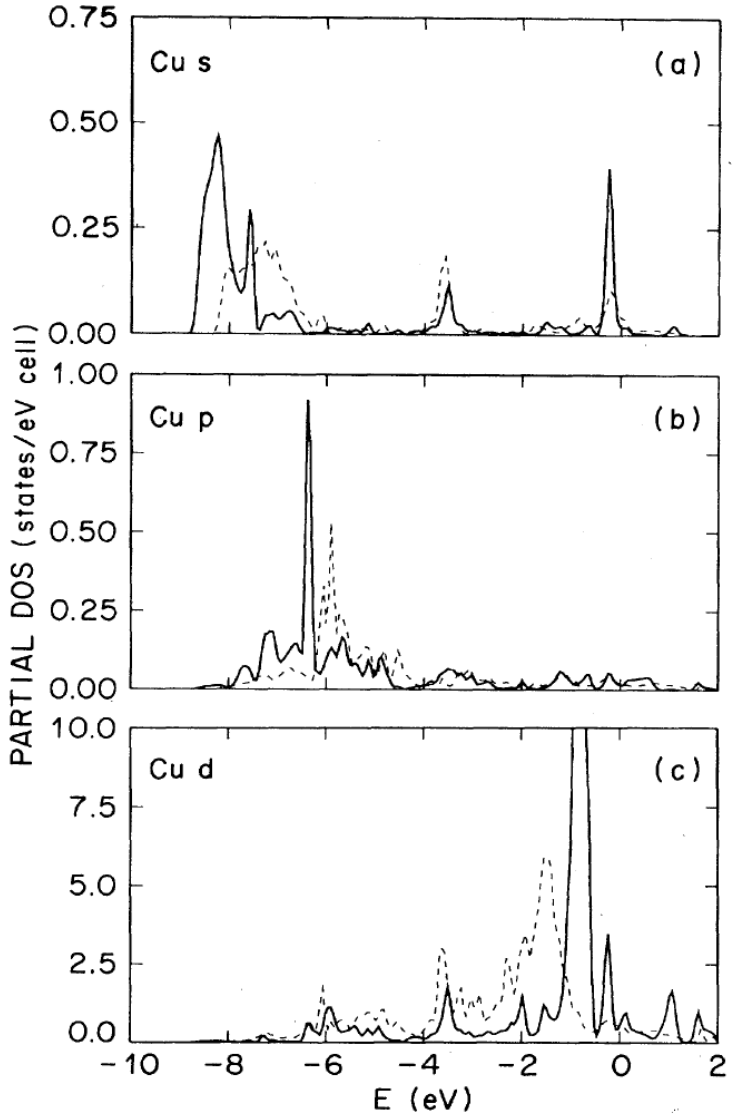

Figure 37: The effect of the constraining potential on different channel-specific partial DOSs. Solid lines represent the partial DOS for various orbitals of a copper atom in the unconstrained system, and dashed lines are the partial DOS when a 0.2 Hartree potential was applied to the d channel of that copper atom. Taken from reference 321.

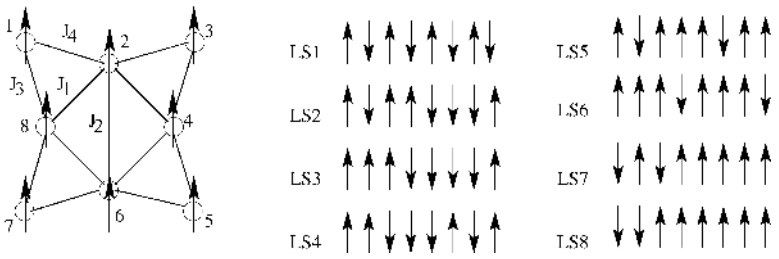

Figure 38: Depiction of the exchange coupling interactions between spin-5/2 Fe^{III} ions in Fe_8. The Fe_8 system is of particular note as it is a single-molecule magnet; a wide spread of phonomena such as macroscopic quantum tunneling, steplike hysteresis, and the potential for molecular magnetic data storage devices have led to interest in this class of molecules. Fe_8 in particular is noteworthy for having strong spin frustration, so that the details of the microscopic interactions can greatly affect the overall behavior. LS1–LS8 are the different spin configurations used to compute ranges of values for the couplings. Used with permission from reference 225.

that go into this Hamiltonian, by accurately predicting the energies of the uncoupled spin states (also known as Ising states). These uncoupled spin states are not (in general) eigensolutions of the Hamiltonian at hand, but they are well-represented by single determinants and have localized spins so that their energies are well-reproduced by common functionals. The eigenstates of equation (69), on the other hand, typically involve linear combinations of *many* uncoupled states. Phrased in the language of quantum chemistry, the associated wavefunctions have significant multireference character. As such, they are poorly represented in traditional DFT, even with constraints. However, by using CDFT to determine the exchange couplings and then using the model Hamiltonian to predict the eigenstates, the energy spectra of complex magnetic systems becomes accessible.

This methodology has been applied to quite complex systems — an eight-center spin network for the "ferric wheel" system is depicted in Figure 38.[225] In this case, CDFT was used to determine the eight low spin configurations (LS1-LS8) and these configurations were used to extract the four unique exchange couplings. Note that the eight spin configurations shown overdetermine the four symmetry-unique couplings, so that the derived couplings will depend somewhat on which spin states are included in the fit. Depending on the configurations

chosen, one obtains couplings in the ranges: $-130 \geq J_1 \geq -143\text{cm}^{-1}$, $-14 \geq J_2 \geq -21\text{cm}^{-1}$, $-42 \geq J_3 \geq -47\text{cm}^{-1}$, and $-10 \geq J_4 \geq -18\text{cm}^{-1}$; these compare quite well to the experimental ranges $-120 \geq J_1 \geq -140\text{cm}^{-1}$, $-20 \geq J_2 \geq -25\text{cm}^{-1}$, $-35 \geq J_3 \geq -41\text{cm}^{-1}$, and $-15 \geq J_4 \geq -18\text{cm}^{-1}$. In contrast, the couplings obtained from broken-symmetry DFT state energies for this complex are qualitatively incorrect, even producing some couplings of the wrong sign. The accurate parameterization of this Hamiltonian paves the way for subsequent quantum mechanical modeling of this molecule — including looking at quantum tunneling of the magnetization[331] and the dynamics of the molecular spin moment in a magnetic field.[243] In these situations, the accurate quantum wavefunction will involve a linear expansion in terms of $6^8 = 1,679,616$ spin configurations — a situation that would be completely hopeless using a single-configuration method like KS-DFT!

Not all systems are amenable to the Heisenberg Hamiltonian. In particular, magnetism in metallic systems fails to conform to the Heisenberg picture because the unpaired spins are not necessarily localized — instead one often deals with itinerant magnetism. In general, CDFT is not as amenable to these problems, but we should highlight one recent application that succeeded in treating magnetism in FeAl with the help of CDFT.[323] The standard approach for enforcing localization in metals is LDA + U, which we discuss further in section 7.[72] Briefly, LDA + U takes a standard LDA calculation and adds Hubbard U terms to certain atoms — typically d or f-block metals. This simple correction is enough to qualitatively correct the magnetic behavior of many systems where traditional DFT fails. However, there is an ambiguity in LDA + U that results from the double counting of electron repulsion terms between the LDA energy expression and the Hubbard U term. There are two limiting cases — the around mean field (AMF) and fully localized (FL) limits — where the double counting correction can be worked out. Because AMF always lowers the total energy and FLL raises it, interpolating between the two limits subject to the constraint that the total energy correction is zero seems a reasonable prescription.[323] To enforce the physical idea

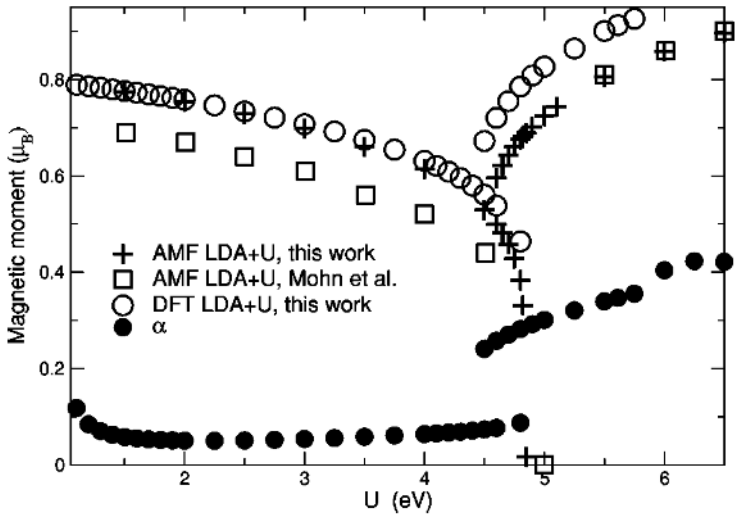

Figure 39: Magnetic moments of FeAl for AMF and the "DFT" flavors of LDA+U compared with the results of Mohn *et al.*[332] Taken from reference 323 ("this work" in the caption).

that the energy correction should be zero, one of course uses constrained DFT. That is to say, one uses constrained DFT *on top of* LDA + U to obtain a unique prescription for the double counting correction. The constraint is (as always) enforced via a corresponding Lagrange multiplier, which in this case appears as $(U - J)/2$. For a given U, the energy and J are then determined self-consistently so as to minimize the total energy subject to the constraint that the double counting correction is zero. It is convenient to characterize the system with an interpolation parameter, α. When $\alpha = 0$, the AMF limit is attained; $\alpha = 1$ corresponds to the FL limit. The behavior of α as a function of U in the magnetic system FeAl (shown in Figure 39) is quite fascinating. For small U, α is small, showing that the itinerant AMF limit is nearly attained; in contrast, the system is more intermediate between the two limits for large U. The behavior in the hysteresial region is of note, where paramagnetic and ferromagnetic solutions coexist.

One can also use CDFT to make reduced Hamiltonians that describe simultaneous charge and spin motion in conjugated molecular wires.[322] Within the realm of quantum chemistry, there is a long history of the use of qualitative molecular orbital theory to describe such

systems. One important representative from this family is the PPP model, which can be cast as an extended Hubbard model with generic two-site Coulombic repulsion:[311]

$$\hat{H} = -\beta \sum_{j}^{N-1} \sum_{\sigma} \left(\hat{c}^{\dagger}_{j,\sigma} \hat{c}_{j+1,\sigma} + \hat{c}^{\dagger}_{j+1,\sigma} \hat{c}_{j,\sigma} \right) - \sum_{j,k}^{N} \Gamma_{j,k} \hat{n}_j + \frac{1}{2} \sum_{j,k}^{N} \Gamma_{j,k} \hat{n}_j \hat{n}_k \tag{70}$$

$$\Gamma_{j,k} = \left(r_0 |j-k| + \frac{1}{g} \right)^{-1} \tag{71}$$

The adjustable parameters are β and g. Once again, the CDFT is useful in parameterizing the model based on *ab initio* data. Because conduction under finite bias probes states far from the ground state, it is not possible to parameterize β and g based simply on the parabolic behavior of the charge around the ground state, as done in Figure 36. Instead, a somewhat qualitative fitting approach needs to be taken, similar to early scanning techniques used[161,320] to attain target values for localized charge. Toward this end, Figure 40 shows the behavior of N_{tot} and M_{spin} over a range of applied potentials, both from CDFT and from the PPP model. The overall slope of the N_{tot} curve is controlled by the β parameter while the slope of the M_{spin} curve is controlled by g, effectively fixing values of $\beta = 0.16$ and $g = 0.55$ in the model. In this case, the PPP parameters so obtained are within a factor of two of values previously suggested.[333]

It is clear from the curves that the PPP model has excellent agreement with *ab initio* HF, but it does a less impressive job reproducing B3LYP. This discrepancy is attributable to the presence of SIE in B3LYP — indeed, by artificially introducing SIE into the PPP model (PPP-SIE in the figure) one obtains a model Hamiltonian that tracks the B3LYP results very well.

With these model parameters in hand, it is possible to use high-level correlation techniques based on the generator coordinate method[334–337] to explore the dynamics of charge conduction through these wires. These simulations allow for the treatment of quantum wave-

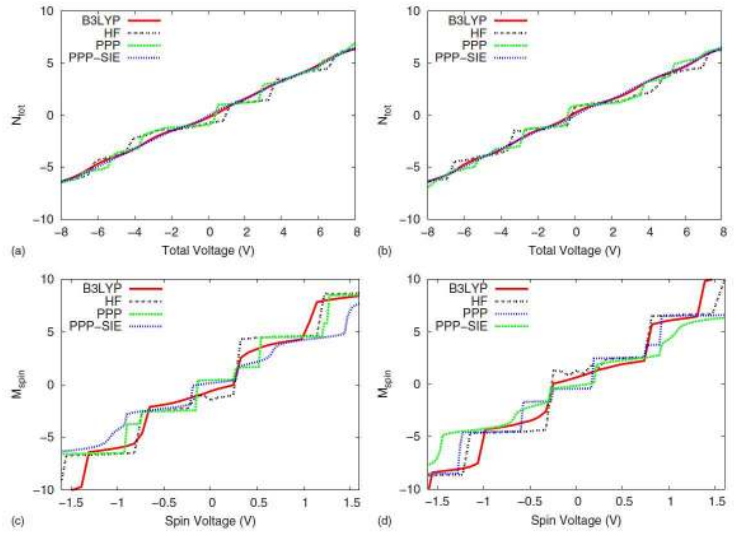

Figure 40: B3LYP and Hartree-Fock calculations on a polyacetylene wire $C_{50}H_{52}$, with corresponding PPP calculations for a 50-site chain, and "PPP-SIE" with artificially reduced exchange term, showing the dependence of population difference N_{tot} (source minus drain) upon spin-independent constraining potential V_{tot} with fixed spin-dependent potential of $V_{\mathrm{spin}} = 0.272V$, and net spin difference (source minus drain) M_{spin} upon spin-dependent potential V_{spin} with fixed spin-independent potential $V_{\mathrm{tot}} = 1.36V$. Shown for the anion $C_{50}H_{52}^{-}$ (a,c) and cation $C_{50}H_{52}^{+}$ (b,d). Taken from reference 322.

functions that involve millions of determinants and wires that are significantly longer than those which can be easily accessed using DFT or TDDFT. These correlated calculations show the disturbing trend that most functionals shift the transport gaps of these wires in the *wrong direction*. True many-body correlation causes the gap to increase, as the system approaches a Mott insulator transition,[338] while all common functionals narrow the gap significantly. Thus, once again we see that using CDFT in conjunction with a simple model Hamiltonian extends the reach of modern DFT.

6.3 Static Correlation

One of the biggest challenges remaining for quantum chemistry is the proper treatment of systems with strong (static) correlation.[339,340] Reaction barriers,[132,341,342] bond dissociation[55,343,344] and conical intersctions[46,47,345] all involve significant static correlation and remain the bêtes noires of computational methods, including DFT. Static correlation is loosely defined by the inability of a single determinant to correctly capture the nature of the wavefunction; this breakdown of the single-determinant approximation is nicely illustrated by an example. Consider the dissociation of a heteronuclear diatomic molecule such as LiF to infinite separation.[346,347] At short distances, the wavefunction is dominated by the ionic configuration, $|\mathrm{Li}^{+}\mathrm{F}^{-}\rangle$, which is well represented by a single determinant and therefore (by definition) has little or no static correlation. However, at long distances, the wavefunction will be dominated by the covalent singlet state $|\mathrm{Li}^{\uparrow}\mathrm{F}^{\downarrow}\rangle + |\mathrm{Li}^{\downarrow}\mathrm{F}^{\uparrow}\rangle$ which is *not* a single determinant. Thus, the molecule transitions from weak correlation at short bond lengths to strong (static) correlation at large distances. DFT traditionally has difficulty describing these types of strong correlation, since KS theory is traditionally formulated with just a single determinant. Multi-determinant KS methods have been attempted,[348] but are not in common use. Furthermore, in the LiF case, there is an additional complication due to SIE: pure semilocal DFT does not even dissociate to neutral fragments, but to an unphysically

stabilized fractionally charged $|\mathrm{Li}^{+\delta}\mathrm{F}^{-\delta}\rangle$ state.[349] The intermediate region is even more of a challenge, as an accurate method must navigate the transition from ionic to neutral, which involves commanding the balance between static correlation, weak dynamic correlation and SIE.

An elegant solution to this problem is to embrace the multiconfigurational nature of the system and introduce multiple Kohn-Sham determinants into the description of the system. The intermediate regime might then be described as

$$\Psi_{\text{stretched}} = c_1\Phi_{\text{ionic}} + c_2\Phi_{\text{neutral}} \tag{72}$$

$$c_1^2 + c_2^2 = 1 \tag{73}$$

The c_i form the CI vector of a model Hamiltonian, in the basis of the (as-yet unspecified) Φ_{ionic} and Φ_{neutral}. CDFT provides an easy framework to produce these chemically intuitive states by enforcing a combination of charge and spin constraints to the system. The CDFT energies then form the diagonal elements of this model Hamiltonian, whilst the off-diagonal elements are populated by the coupling elements of section 5.[47,54,55,132,272]

This formalism can be readily generalized to the case of N states generated by arbitrary constraints:

$$\begin{pmatrix} H_{11} & H_{12} & \cdots & H_{1N} \\ H_{21} & H_{22} & & H_{2N} \\ \vdots & & \ddots & \vdots \\ H_{N1} & H_{N2} & \cdots & H_{NN} \end{pmatrix} \begin{pmatrix} c_1 \\ c_2 \\ \vdots \\ c_N \end{pmatrix} = E \begin{pmatrix} 1 & S_{12} & \cdots & S_{1N} \\ S_{21} & 1 & & S_{2N} \\ \vdots & & \ddots & \vdots \\ S_{N1} & S_{N2} & \cdots & 1 \end{pmatrix} \begin{pmatrix} c_1 \\ c_2 \\ \vdots \\ c_N \end{pmatrix} \tag{74}$$

where the S terms incorporate the non-orthogonality of generic CDFT states. By analogy to conventional configuration-interaction (CI) methods which build and diagonalize an interaction matrix between Hartree-Fock determinants, this method is termed CDFT-CI, us-

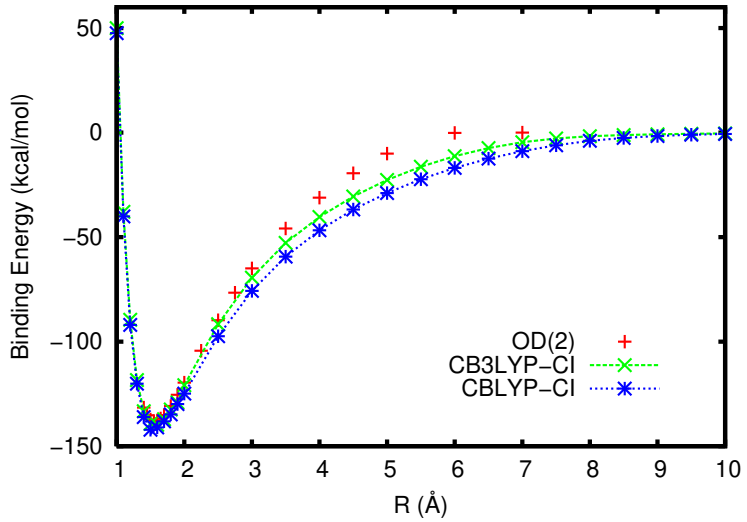

Figure 41: Dissociation curve of LiF as computed with various CDFT-CI prescriptions in a $6-311G++(3df,3pd)$ basis set. Optimized-orbital coupled cluster doubles calculations[350,351] with a second-order correction [OD(2)] results are included as a reference. Used with permission from reference 55.

ing interactions between CDFT Kohn-Sham determinants to produce better approximations to the true energy eigenvalues of the Hamiltonian.[55] CDFT-CI is quite remarkable in its generality — all of the other model Hamiltonians described in this section have been explicitly designed for a particular problem, or particular narrow class of problems. In contrast, CDFT-CI is less a single model Hamiltonian form and more a framework for constructing custom models — there is flexibility to use an arbitrary set of constrained states as the basis for the model Hamiltonian. Choosing these basis states (tailored for the particular system of interest) then defines the Hamiltonian, which CDFT-CI computes and diagonalizes to yield energies, CI vectors, and other one-electron properties.

Returning to the system which motivated this discourse, the dissociation curve for LiF using CDFT-CI is shown in Figure 41, within a four-state basis of $Li^{+}F^{-}$, $Li^{-}F^{+}$, $Li^{\uparrow}F^{\downarrow}$, and $Li^{\downarrow}F^{\uparrow}$. Results are presented for CDFT-CI using two different functionals; both perform well, with the hybrid B3LYP yielding the best results. As expected, passing through the dissociation region shows a smooth transition from ionic to neutral for all three curves, as tracked

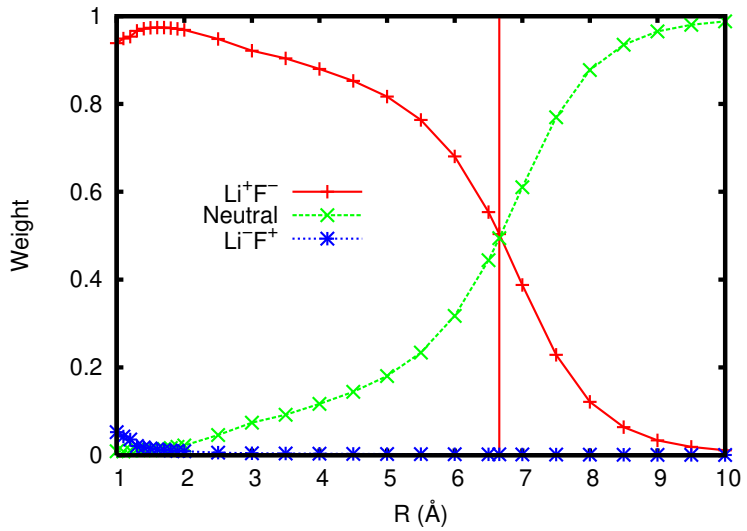

Figure 42: Weights of configurations in the final ground state of LiF. Used with permission from reference 55.

quantitatively by following the CI vectors, shown in Figure 42. The crossover between ionic and neutral basis states occurs at 6.6 Å, as expected from where the Coulombic attraction of the ions equals the difference of electron affinity and ionization potentials.[55] Unlike conventional DFT, all the CDFT-CI curves show the correct dissociation limit in Figure 41. The accuracy of BLYP and B3LYP around the equilibrium geometry is preserved, indicating that the CDFT-CI prescription does not spoil conventional DFT in regions with little static correlation. The PESs are accurately described everywhere — at the equilibrium geometry, at infinite separation, and in the troublesome region in-between where static correlation is strongest.

Static correlation also plays a significant role in intra- and intermolecular rearrangements, such as elementary reaction steps. The greatest challenge to DFT is at the reaction barrier, where bond breaking leads to strong static correlation,[341,352] and traditional functionals are known to predict poor reaction barrier heights.[349,353–355] Simple two-state CDFT-CI provides an alternative route to reaction barrier heights as follows. First, we assume that two basis states ("Reactant" and "Product") are sufficient to construct a diabatic picture of

	LSDA	CLSDA-CI	PBE	CPBE-CI	B3LYP	CB3LYP-CI
mean error	-16.7	-8.9	-10.0	-3.4	-5.0	1.2
mean absolute error	16.7	10.0	10.0	4.2	5.1	2.5

Table 12: Errors in system energy in kcal/mol for a set of 64 hydrogen transfer, heavy atom transfer, and nucleophilic substitution reactions, using a variety of functionals. Regular DFT and CDFT-CI results are contrasted.

the reaction. The wavefunction at the transition state is then a linear combination of these configurations. In this case, we can construct a good model Hamiltonian from two CDFT states — one constrained in accordance with the reactant fragments, the other in accord with the products. We then obtain the transition-state energy from the lowest eigenvalue of the CDFT-CI secular equation. The results of this method for a set of 64 reactions taken from the HTBH38/04 and NHTBH38 databases[341] are shown in Table 12.[132] The CDFT-CI barrier heights are typically improved by a factor of 2-3, which is significant; it is approximately the difference in quality attained when going from a pure functional to a hybrid.

The set of reactions includes many examples of hydrogen atom transfer, heavy atom transfer (e.g. from $CH_3 + FCl \rightleftharpoons CH_3F + Cl$), and nucleophilic substitution, largely between halogens and methyl groups. For these isogyric reactions, the difference between the "reactant state" and "product state" at the transition-state geometry is merely whether the electrons of the transferring group mingle with the reactant fragment or the product fragment, a seemingly minor condition when the written reaction does not involve charge transfer amongst fragments. Nonetheless, CDFT will produce different constrained states for these different conditions, and assembling a model Hamiltonian with their energies and coupling produces energy eigenvalues that are quite accurate. Explicitly constraining charge and spin to be localized reduces the effects of the DFT SIE which plagues ordinary ground-state calculations, especially at reaction transition states.

The reasons why CDFT-CI is so successful are relatively clear: by using CDFT states as

the basis for the CI we are able to effectively control the impact of SIE on the calculations and include dynamic correlation through the CDFT energies. By performing a CI calculation on top of the CDFT states, we add back in the static correltation that is artificially missing from the localized CDFT solutions. As a result, CDFT-CI seems like a well-balanced tool for the description of static correlation in molecular systems.

6.4 Excited States

Electronic excited states play a central role in the function of optoelectronic devices such as LEDs,[356] photoswitches,[357] and photovoltaics,[358] but the accurate description of these states is probably the greatest unsolved problem in quantum chemistry at present. As we have already seen, CDFT can describe a small handful of excited states directly (i.e. those involving long-range charge or spin separation). However, when CDFT is integrated into an appropriate model Hamiltonian, the range of excited states amenable to simulations expands dramatically. The reasons for this are twofold: the reduced Hamiltonian simulations are typically much *faster* than DFT calculations, so that larger systems can be simulated, and the simplicity of the model Hamiltonian often allows for a much more *sophisticated* treatment of electron correlation in the excited state. Both of these ideas were illustrated briefly above using the PPP model of polyacetylene to describe conduction dynamics. In this section, we focus on the final frontier of electronic excited states.

As a starting point, it would be ideal if one could accurately treat linear optical properties, such as the absorption and emission spectra of a system. Toward this end, let us consider the absorption spectrum of GaAs, shown in Figure 43.[324] The experimental spectrum is rather poorly reproduced by the independent particle approximation (IPA), particularly at low energies, where the electron-hole attraction is most pronounced. In order to account for electron interactions, we can supplement the IPA in much the same way we added electron-electron repulsion terms to the tight binding model to obtain PPP. In this case, adding all

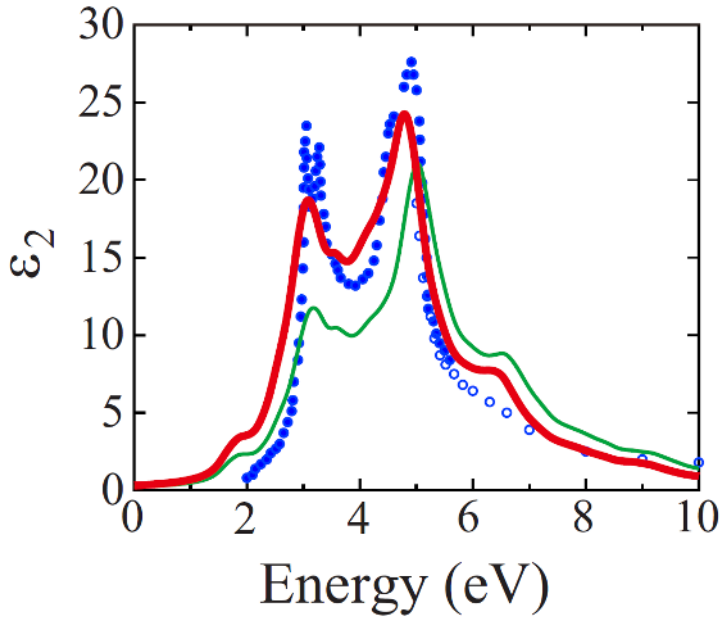

Figure 43: The optical absorption spectrum of GaAs. Circles represent experimental data from references 359 and 360, the thick red line is downfolded-CDFT CIS calculations, and the thin green line is from IPA calculations. Taken from reference 324.

two-center Coulomb repulsion terms results in the CNDO model,[361,362] which can be parameterized using CDFT exactly as described above. To transform the plane-wave DFT basis into a site model, maximally localized Wannier functions (MLWFs)[61,363,364] are used, and CDFT calculations determine U and a screened Coulomb repulsion V_{ij}. One can then take the derived CNDO calculation and perform CIS (configuration interaction with single excitations) to approximate the spectrum in the presence of interactions, as shown in the Figure. Clearly, the intensity of the low-energy excitation peak is suitably enhanced, indicating that the proper physics has been restored. It should be noted that the resulting CNDO-CIS calculations are much faster than the associated TDDFT spectrum, and yet the simpler calculation captures the important effects.

GaAs exemplifies the typical situation for solids, where a large set of excitations from the ground state are collectively important for describing the optical properties. In chemistry, one often has the opposite scenario: the low-lying excited states are often dominated by

only a handful of very important configurations. CDFT-CI excels in this regime, choosing a small handful of relevant configurations from chemical intuition to be the extent of the CI calculation. This formal picture is particularly important for the description of conical intersections — the seams of true degeneracy between electronic states in the high-dimensional configuration space.[295,345] At any such intersection, there are two directions in which the degeneracy is broken (arising from the two conditions that the energy gap and coupling must both go to zero at the intersection), so a three-dimensional plot shows only a single point of intersection, resembling a dual-lobed cone (hence the name).

A complete discussion of these fascinating objects is beyond the scope of this review. For the present purposes, we merely note that these topological features are particularly challenging for single reference methods, as the proximity of the ground and excited state necessarily introduces extremely strong multiconfigurational character into the system.[46,347] As TDDFT is a single-reference method, we expect it to fail qualitatively in the description of conical intersections, and this is indeed the case. For example, Figure 44(a) shows the TDDFT energies of water near its linear geometry, where symmetry dictates there must be a conical intersection.[47] The ground state potential surface is not bad, particularly at short distances, but TDDFT fails to describe even the qualitative topology of the intersection correctly: instead of finding a cone, TDDFT predicts a double seam. By comparison, the CAS(6,9) calculation (with 3057 determinants) shown in Figure 44(b) provides an accurate depcition of both the ground and excited state around this intersection. In order to describe this system correctly within the context of DFT, we turn to CDFT-CI. Our CI space spans just four physically motivated configurations: $HO^{-}H^{+}$, $H^{+}OH^{-}$, $H^{\uparrow}OH^{\downarrow}$, and $H^{\downarrow}OH^{\uparrow}$. No single one of these states is a good approximation to the ground or excited state of H_2O near the intersection. But by taking linear combinations of these states, CDFT-CI produces the conical intersection in Figure 44(c), which is quantitatively correct. CDFT-CI has a further advantage over CAS in that CAS cannot include any *dynamic* correlation, which the DFT

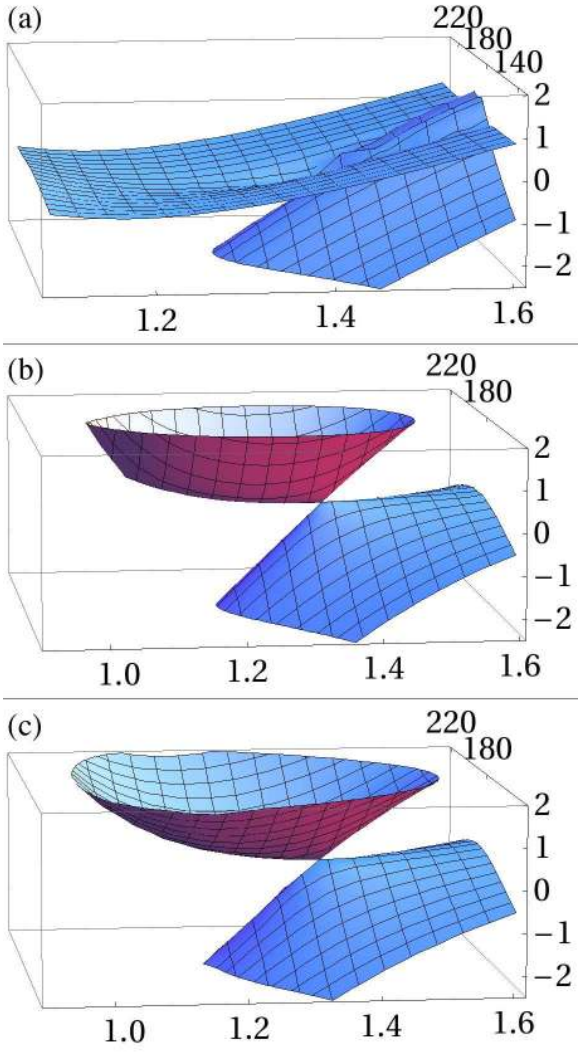

Figure 44: The conical intersection for linear water, shown as computed via TDDFT, CAS(6, 9) (six electrons in nine orbitals) and a four-state CDFT-CI. Used with permission from reference 47.

functional treats inherently; expensive corrections above CAS such as CASPT2 or MRCI are needed to introduce dynamic correlation into the computed states. Thus, CDFT-CI successfully leverages the ability of hybrid DFT functionals to describe dynamic correlation in combination with a description of static correlation among a hand-picked basis of spin- and charge-constrained states. Combined, they produce a custom model Hamiltonian that allows for a very concise and accurate description of the electronic energy manifold near this conical intersection. Overall, it would appear that the method holds significant promise for the description of low-lying excited states in molecular systems.

6.5 Conclusion and Future Work

As demonstrated in this section, the use of CDFT to parameterize model Hamiltonians proves to be a quite general tool, with applications to the band structure and excitation spectra of electronic solids, magnetic systems, conduction, molecular rearrangement and PES crossings. Once a particular Hamiltonian form has been parameterized, calculations using the model can be extended to larger systems or high-level computational techniques which would be prohibitively expensive as DFT calculations. We thus recognize the overarching theme that model Hamiltonians extend the reach of traditional DFT calculations both in terms of system size and accuracy.

There are, of course, a variety of prescriptions being used to connect the CDFT calculations to the models in the applications above. Among these, the CDFT-CI scheme is perhaps the most flexible and promising, as long as only a handful of states are chemically relevant. In this scheme, CDFT energies and couplings provide a diabatic basis for $\hat{H}$ that yields both the ground and excited states of a very general class of systems over a variety of conditions. This framework should be quite flexible, and may make *ab initio* molecular dynamics on electronic excited states more accessible to larger systems. Along these lines, the main hurdle to be overcome is the implementation of analytical gradients of the CDFT-CI energy with

respect to nuclear position (i.e. nuclear forces). Such an advance would allow for efficient location of non-symmetry-required CIs and excited-state molecular dynamics. Likewise, there is still room for innovation in the area of using CDFT to parameterize model Hamiltonians of predetermined form — models for studying intersystem crossing in three-spin systems are a prime candidate for such CDFT treatment.[365] Between the array of specialized models and the generic flexibility of CDFT-CI, CDFT has been indispensible in turning simple model Hamiltonians into accurate tools that yield chemical insight.

7 Related Approaches

The preceding sections illustrated how CDFT addresses several outstanding challenges in DFT while extending its range of applicability to situations where a diabatic representation is appropriate. Of course, other approaches have been proposed and implemented to address many of these needs. Not surprisingly, some of these alternatives share key attributes with CDFT.

In this penultimate section, we highlight new and ongoing developments in DFT that share common goals with the CDFT approach. We focus in particular on the reduction of self-interaction error in charge- and spin-localized systems, the generation of diabatic states through orbital localization, and the even-handed treatment of ground and excited states.

7.1 Overcoming Self-interaction Error in Approximate Density Functionals

Most density functional approximations harbor some degree of self-interaction error (SIE). Early studies of SIE were motivated by the observation that many approximate exchange-correlation functionals cannot supply an exchange-correlation energy that exactly cancels the Coulomb self-interaction of an arbitrary one-electron density.[366] The more general and more recently developed concept of many-electron SIE[354] frames this error as the deviation from linearity of the energy as a function of the number of electrons.[367,368] In practice, SIE in pure density functionals often manifests itself as a delocalization error, as it tends to incorrectly favor delocalized densities.[36,280] Global hybrid functionals with a large admixture of Hartree-Fock exchange can present the opposite (localization) error. For reviews on SIE, see refs 369 and 140; here we focus on methods that adopt standard functionals and attempt to correct or control the SIE, in the same spirit as CDFT. In particular, we highlight how CDFT and three other approaches — explicit self-interaction correction, DFT + U, and

range-separated hybrids — achieve some of the same goals.

The effects of SIE are most severe in systems with significant fractional electron character.[349] Stretched H_2^+ provides a simple example: semilocal functionals predict a much lower energy for the delocalized electron density $H^{+0.5}-H^{+0.5}$ than for the localized one H^+-H, even at infinite separation. The tendency of semilocal functionals to favor delocalized densities for mixed-valence compounds is another manifestation of this effect. Through the application of charge constraints, CDFT mitigates the over-delocalization effect at the cost of some degree of arbitrariness in the definition of the constraint itself; nevertheless, the benefits of reducing the fractional electron character of the system with CDFT are tangible in the successes of CDFT-CI for properties involving stretched systems, such as barrier heights and conical intersections.

Many-electron SIE is also at the heart of the band gap problem,[369] which has direct bearing on the accuracy of LR-TDDFT for CT excitation energies. The band gap problem refers to the discrepancy between the Kohn-Sham orbital energy difference $\epsilon_{\mathrm{LUMO}}-\epsilon_{\mathrm{HOMO}}$ obtained with semilocal functionals and the band gap, i.e. the difference between the electron affinity and the ionization potential. In LR-TDDFT, the Kohn-Sham orbital energy difference is the zeroth-order approximation to the excitation energy, and while higher-order corrections provide reasonably accurate valence excitation energies, these higher-order terms tend to zero for CT states.[44] The CDFT prescription for CT states entails a direct construction of the CT state density, thus circumventing the band gap problem and its consequences for LR-TDDFT.

Targeted efforts to correct for SIE have been ongoing since the first implementations of density functional approximations for practical calculations. The original Perdew-Zunger SIC introduces an orbital-by-orbital correction to the SIE which increases the computational complexity considerably.[366] The corrected functionals lead to improved orbital energies, but their performance for chemically significant quantities such as bond lengths and reaction

barrier heights proved worse in many instances than their uncorrected counterparts.[370–372] Unger introduced a related SIC which is closer in spirit to CDFT because it is formulated in terms of atomic density fragments defined in real space;[373] however, its practical application to molecular systems remains largely unexplored. The development of functionals that afford piecewise-linear energies as a function of electron number[367] is a major outstanding goal in approximate DFT and should enhance the predictive power of DFT for chemical properties and reactivity in the ground state.

The DFT+U methods mentioned in section 6 provide another way to mitigate the effects of SIE. In the DFT + U approach, one takes a typical LDA or GGA calculation and adds Hubbard U terms (*q.v.* Section 6.1) to certain atoms — for example, d or f-block metals. One then tunes the value of U (either on empirical grounds, using CDFT or linear response[64]) and then performs a new calculation where the LDA Hamiltonian is supplemented by the new on-site repulsion terms. By penalizing doubly-occupied orbitals on the the metal, delocalized states are disfavored (since they are superpositions of all possible local charge states) in favor of localized, fixed-charge states. This is how DFT + U partially compensates for SIE.

The charge-localized states generated by LDA + U are qualitatively correct in an array of different Mott insulators and exotic conductors, so LDA + U has a wide impact: it has been used to understand magnetism in lanthanum cobaltates,[374] to describe the electronic structure of perovskites[75] and correlated metals[323] and to predict redox potentials of transition metal systems,[375] among other applications. The U correction can also be used to penalize non-integer populations on electron donors and acceptors in ET applications.[376] Furthermore, DFT+U has shown promise in correcting the failure of LDA and GGA functionals to predict the ground state spin multiplicity of certain transition metal complexes[377] and of adatoms adsorbed on graphene.[378] To illustrate, in Figure 45, the energy of several low-lying spin states of the pentacoordinate heme-imidazole complex, Fe(II)P(Im), are plotted against the value of the Hubbard U parameter. The plot shows that the DFT+U

ground state crosses over from the triplet to the quintet around $U = 2$ eV; the quintet is the experimentally observed ground state and is recovered for physically reasonable values of U.

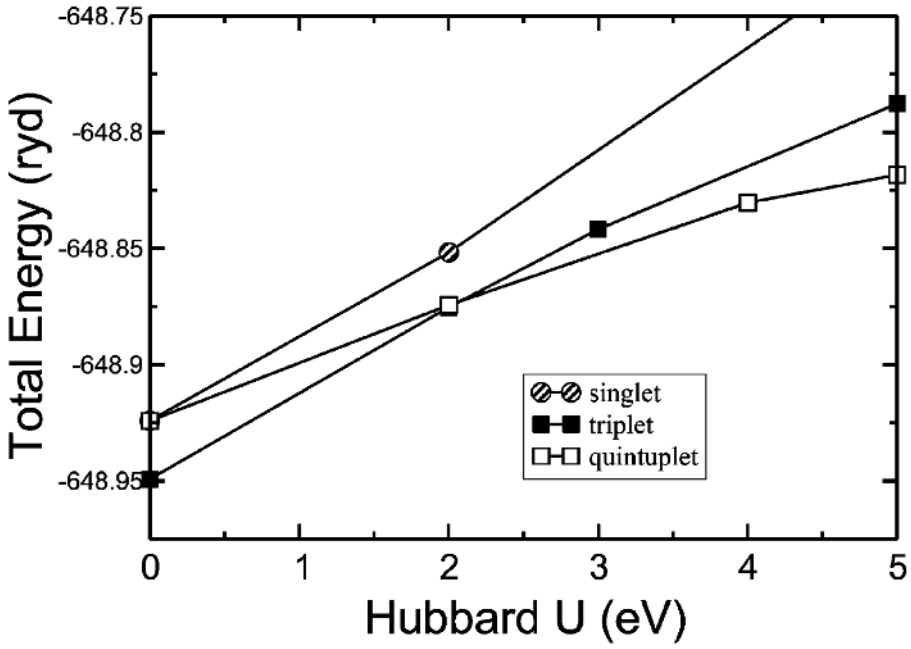

Figure 45: Dependence of low-lying spin state energies of Fe(II)-P(Im) on the Hubbard U parameter. Reproduced with permission from ref 377.

The physics of DFT $+ U$ and CDFT are quite similar: both methods mitigate or remove SIE from existing functionals. The role of the Hubbard U in DFT $+ U$ is replaced by the constraining potential V in CDFT. Thus, depending on one's perspective, DFT $+ U$ is either an extension of CDFT (as the U parameter can be determined via CDFT) or as a parallel method that accomplishes many of the same aims in a different context.

Of course, we wouldn't need to correct for SIE if we had the exact density functional; by extension, we can anticipate that better approximate functionals will suffer less severely from many-electron SIE. As an example, we consider the class of functionals known as range-separated[138–140] or long-range corrected[136,379] functionals, which have been shown to be more robust to the effects of SIE[140] than their conventional hybrid counterparts. These functionals employ a judicious balance of exact and semilocal exchange, beyond the simple admixture

employed in global hybrid functionals. The success of global hybrids can be attributed to cancellation of delocalization error in the semilocal exchange functional by localization error introduced by exact exchange.[280] However, this error cancellation is incomplete in global hybrids; in particular, it fails to recover the correct asymptotic behavior of the exchange-correlation potential.[380] Range-separated functionals recover the correct $1/R$ asymptote and are becoming widely adopted. Their use in LR-TDDFT calculations[137] shows particular promise.

As an example of how long-range correction schemes and CDFT can accomplish similar goals, we consider the lowest CT state of the ethylene-tetrafluoroethylene dimer (C_2H_4—C_2F_4) as a function of intermolecular distance. This complex is an exemplar for both the failures of LR-TDDFT with conventional hybrids[44] as well as the successes of the range-separation approach.[137] Figure 46 shows the energy of the CT state as predicted by LR-TDDFT with the global hybrid PBE0 and a long-range corrected variant, as well as by CDFT with the B3LYP global hybrid; each curve is shifted so that its zero of energy occurs at intermolecular separation $R = 5$ Å. Without range separation, LR-PBE0 severely underestimates the energy of the CT state at long distances because of the incorrect asymptotic form of the exchange-correlation potential, whereas its long-range corrected variant tracks the $-1/R$ reference curve quite well. CDFT also correctly describes the distance-dependence of the CT state energy, without the need for a long-range correction scheme.

In the forseeable future, the improvement of range-separated hybrids could potentially cure SIE problems in DFT and TDDFT, at least for practical purposes. In this situation, methods like CDFT and DFT+U would no longer be needed to avoid unphysical delocalization and poor CT excited states. However, even with a practically exact functional, CDFT could still play a useful role in constructing diabatic states and parameterizing model Hamiltonians for complex problems, as discussed below.

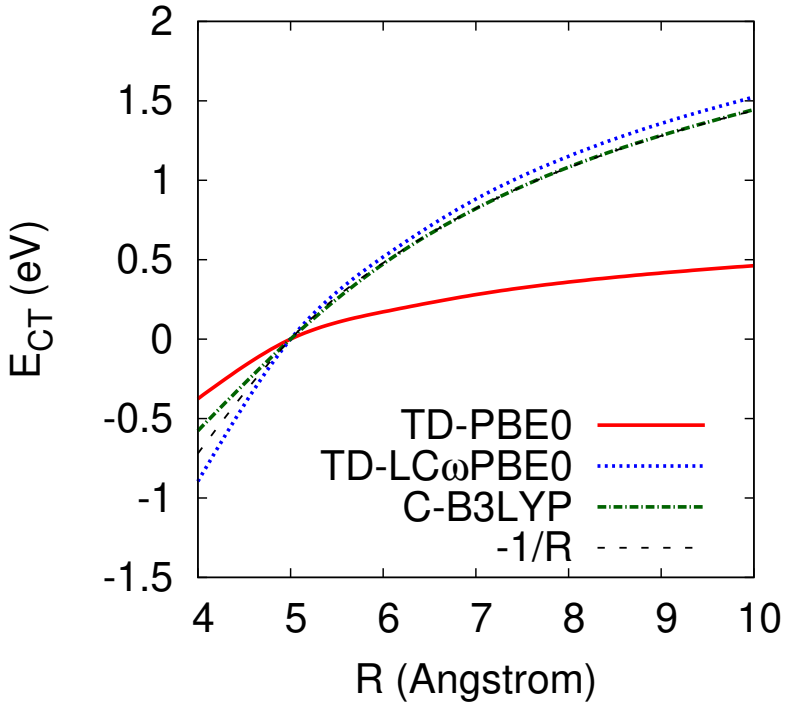

Figure 46: Energy of the CT state of the ethylene-tetrafluoroethylene complex as a function of intermolecular distance for LR-TDDFT and CDFT. LR-TDDFT with the long-range corrected functional LC-ωPBE0 and CDFT both correctly track the $-1/R$ curve, in contrast with LR-TDDFT using conventional hybrids.

7.2 Orbital Localization Approaches to Diabatic States

Density constraints provide a conceptually simple route to diabatic states, but in some cases the self-consistent determination of the constraining potential can be difficult to achieve. There exists a complementary class of self-consistent methods, known as block-localization (BL) methods,[261] which construct diabatic states by assigning atomic basis functions to predefined molecular fragments and solving the HF or KS equations while forcing the density matrix to be block diagonal with respect to these fragements.[381] The MOs produced in BL-HF and BL-DFT calculations are each fully localized on one of the fragments, hence they are sometimes referred to as absolutely localized molecular orbitals (ALMOs).[382] ALMOs are mutually orthogonal within each block, but are nonorthogonal in general across blocks. Nevertheless, the technique has been successfully used to accelerate SCF calculations on weakly interacting systems, where it is also known as locally projected SCF for molecular interactions (SCF MI).[382]

Like CDFT, BL-DFT carries some of the concepts of valence bond (VB) theory into the realm of first-principles calculations. Its connections to the construction of diabatic states has been highlighted by Cembran and coworkers.[383] BL-DFT provides a natural vehicle for the analysis of VB constructs such as resonance structures. Mo and coworkers illustrated this connection by examining the DFT and BL-DFT descriptions of the allyl radical, cation and anion.[381] The vertical resonance energy,

$$E_{\mathrm{v}}^{\mathrm{res}} = E(\text{BL-DFT}|\text{DFT}) - E(\text{DFT}|\text{DFT}) \tag{75}$$

and the adiabatic resonance energy,

$$E_{\mathrm{a}}^{\mathrm{res}} = E(\text{BL-DFT}|\text{BL-DFT}) - E(\text{DFT}|\text{DFT}) \tag{76}$$

were both obtained, where $E(\mathrm{A}|\mathrm{B})$ represents the energy obtained by method A at the optimized geometry from method B. The resonance energies and optimized geometries are shown in Table 13.

	Delocalized structure	Localized structure		Resonance energy	
allyl	R_0	R_1	R_2	vertical	adiabatic
radical	1.378	1.323	1.509	32.1	23.2
cation	1.377	1.328	1.472	51.1	46.3
anion	1.390	1.336	1.508	48.5	41.8

Table 13: Optimal C−C bond lengths (Å) and resonance energies (kcal/mol) in allyl systems from DFT (delocalized, hence only one unique bond-length R_0) and BL-DFT (localized, with shorter and longer C−C bond lengths R_1 and R_2). Reproduced with permission from ref 381.

Bond lengths for the localized structures are comparable to typical C−C single- and double-bond lengths; thus BL-DFT produces resonance structures that are in keeping with the tenets of basic VB theory. The BL-DFT resonance energies of the allyl cation and anion are similar, amounting to roughly twice the resonance energy of the allyl radical. The elucidation of formal charge states in small systems like allyl can present a challenge for CDFT because the short charge separation distance enhances the sensitivity of the energy to the definition of the constraint regions. The reduced flexibility in the definition of the constraints in BL-DFT makes the BL-DFT approach less precise but still provides a valuable tool for the analysis of VB states from first principles.

A powerful extension of the block localization technique to treat large systems, such as a collection of solvent molecules, at an approximate QM level has been developed by Gao and coworkers.[384–386] The general strategy consists of solving the HF or KS equations for each solvent molecule subject to the electric field due to a collection of point charges associated with the surrounding molecules. These point charges are derived from the localized wavefunction of the corresponding solvent molecules, thus introducing an additional layer of self-consistency to be satisfied; nevertheless, the approach offers a viable route to de-

scribe, for example, a solvent or protein environment, in a framework based on a product wavefunction for the entire system.

BL-DFT has found several applications in the decomposition of molecular interaction energies into contributions such as multipole interactions, polarization and charge-transfer effects, as recently reviewed in ref 387. Mo *et al.* identified the polarization of benzene in benzene-cation complexes as a significant, sometimes dominant, contribution to the interaction energy,[381] underscoring the need to account for polarizability in classical simulations of biologically relevant processes such as transport through ion channels. Khaliullin and coworkers used a BL-DFT approach to decompose the interaction energies of the water dimer,[388] aqueous metal ion clusters,[389] small donor-acceptor complexes,[390] and weakly bound organometallic complexes.[389] They used this information to quantify the role of CT in the binding energies of these complexes.

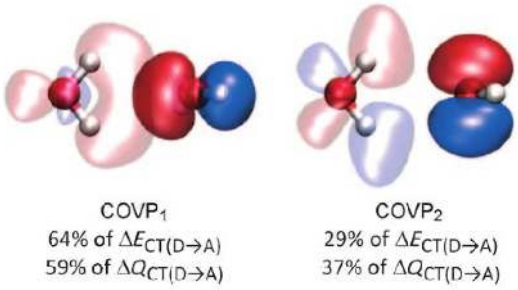

Figure 47: Illustration of two major ALMO contributions to intermolecular CT-induced bonding in the water dimer. Nearly opaque orbitals are occupied, while the more transparent orbitals are virtual. Reproduced with permission from ref 388.

Figure 47 exemplifies how BL-DFT calculations can inform and assess the rationalization of weak interactions like hydrogen bonding, back-bonding, and hyperconjugation in terms of overlap between occupied and virtual MOs. Here, CT in the water dimer is decomposed in terms of complementary occupied-virtual orbital pairs (COVP) for a geometry in which both protons of one water are equidistant from the oxygen of the other water. Altogether, the CT contribution to the binding energy was found to be a minority component which

becomes minimal at the orientation depicted in Figure 47. It is also at this geometry where more than one donor orbital contributes substantially to the CT effect.

Overall, CDFT and BL-DFT share much in spirit, as both techniques generate localized, self-consistent diabatic states in a DFT framework. However, because of the restricted form of the density matrix invoked in BL-DFT, the primary focus in BL-DFT applications has been on intermolecular interactions and the simulation of large condensed phase systems.

7.3 Balanced Treatment of Ground and Excited States in DFT

Density functional theory is formally a ground-state theory;[3] several challenges hinder its formal extension to excited states.[391–394] Nevertheless, DFT-based methods that can describe ground and excited states on the same footing are highly desirable for practical calculations on large systems with several important electronic states. CDFT and CDFT-CI meet this challenge by describing diabatic states as ground states in the presence of different constraining potentials. Diagonalization of the CDFT-CI Hamiltonian then provides both ground and low-lying excited adiabatic states.

Another way to extend the machinery of ground-state Kohn-Sham DFT to excited states is to construct higher-energy Slater determinants self-consistently from the Kohn-Sham orbitals.[8,395] This is usually accomplished by occupying the KS orbitals in a prescribed non-Aufbau manner at each step of the SCF procedure. This procedure goes by several names: ΔSCF,[396] ΔDFT,[26] excited state DFT,[397] and — delightfully — constrained DFT[398,399] (Here the constraint is on the KS orbital occupations rather than on the density).

The idea behind the ΔSCF approach to excited states was first presented by Ziegler, Rauk and Baerends for the computation of multiplet energies in the context of the Xα method.[395] Their work highlights the fact that single-determinant SCF calculations of excited states do not necessarily yield spin eigenfunctions. For example, the lowest singlet excited state of a closed-shell molecule is an open-shell species whose correct description requires two

determinants (Figure 48). Ziegler and coworkers proposed a sum rule that corrects single-determinant ΔSCF energies for spin contamination; in the case of the open-shell singlet, the purification formula is

$$E_s = 2E_{\uparrow\downarrow} - E_{\uparrow\uparrow} \tag{77}$$

where $E_{\uparrow\downarrow}$ and $E_{\uparrow\uparrow}$ represent the energies of the mixed and triplet determinants of Figure 48, respectively.

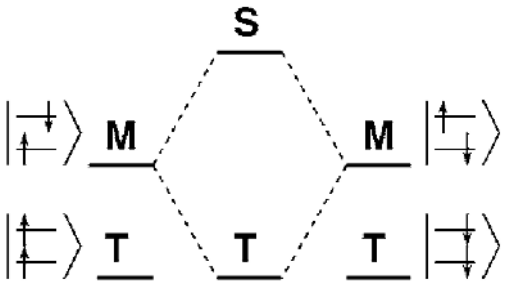

Figure 48: Four singly excited determinants form a basis for one singlet and three triplet spin eigenfunctions. SCF calculations produce single determinants, so some form of spin purification is required to obtain the energy of the pure singlet. Adapted with permission from ref 400.

The SCF equations are often more difficult to converge for electronic states with non-Aufbau orbital occupations, and this is a potential drawback of the ΔSCF method. Modern SCF algorithms are so efficient at seeking the global energy minimum that it can be difficult to maintain non-Aufbau occupations through SCF convergence. However, there are no formal limitations to the convergence of ΔSCF states, and several techniques have been proposed and implemented to retain the target configuration, including the maximum overlap method (MOM),[401] the constrained orthogonality method (COM),[402] and SCF metadynamics.[403]

With the development of practical tools for obtaining ΔSCF states, a number of interesting applications have surfaced in recent years. ΔSCF has proven capable of describing a wide variety of excited states — from valence excitations in dyes[404] and in proteins[405] to

core excitations[406] and Rydberg states[397] — with errors typically only a fraction of an eV in each case. ΔSCF has been shown to provide similar,[404] and in some cases, superior[406] performance to the more frequently employed LR-TDDFT. For example, Robinson and Besley's ΔSCF/MM simulations of the UV/Vis spectrum of the ET protein plastocyanin[405] achieved an accuracy comparable to that of a more expensive multireference configuration interaction (MRCI) approach, while LR-TDDFT significantly underestimates the excitation energies for the two most prominent peaks in the spectrum (Figure 49). These encouraging applications point to a bright future for ΔSCF.

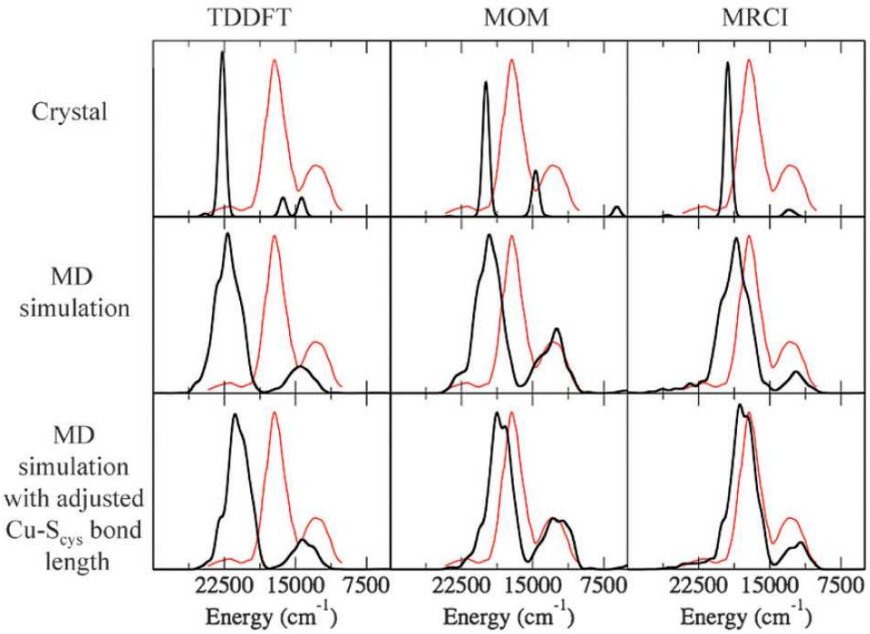

Figure 49: Comparison of simulated UV-Visible spectra of plastocyanin evaluated with TDDFT and with the MOM approach to ΔSCF. Experimental reference spectra are shown in red. Reproduced with permission from ref 405.

Although the Ziegler sum rule, equation 77, is a convenient way to correct the energy of a ΔSCF state for spin contamination, it does not provide access to a spin-adapted density, nor to any other spin-adapted one-electron properties. It is thus desirable in some situations to achieve spin adaptation of the ΔSCF state at the level of the KS orbitals. These observations

motivated the development of the restricted open-shell Kohn-Sham (ROKS) methods.[407,408] Filatov and Shaik derived ROKS by analogy to Roothaan's vector coupling formalism for restricted open-shell Hartree Fock (ROHF) theory,[409] and they found multiplet energies in reasonable agreement with experiment for a range of small molecules,[410] shown in Table 14. Frank and coworkers established ROKS as a computationally efficient DFT method for excited state molecular dynamics.[408,411] Arguments disfavoring restricted open-shell calculations in the context of Kohn-Sham DFT have appeared in the literature,[412] but it should be noted that these arguments address ROKS for ground states of high-spin systems and do not apply to the low-spin excited states under consideration here.

Molecule	LDA	BLYP	BP86	FT97	Expt.
O_2	1.06	0.97	1.01	1.08	0.97
SO	0.77	0.72	0.78	0.80	0.73
C_2^+	1.35	1.04	1.20	1.23	1.37
H_2CO	3.36	3.38	3.32	3.42	3.50

Table 14: Lowest molecular excitation energies (in eV) from ROKS calculations. Reproduced with permission from ref 410.

ROKS has been successfully applied to the calculation of excited-state potential energy surfaces[413] and nonadiabatic coupling vectors,[400] among others. A considerable practical advantage shared by ROKS and CDFT is their accessibility for MD simulations, bestowed by the similarity of their implementation to that of ground-state DFT. The spirit of the ROKS approach has been extended to systems exhibiting significant static correlation in the ground state through the restricted ensemble-referenced Kohn-Sham (REKS) method,[414] and these methods together supply an efficient scheme for studying complex photochemistry such as photoisomerization processes in a molecular rotor.[415]

Looking forward, we note that ΔSCF determinants can, in principle, provide a well-tuned, compact set of reference states for a CI calculation. Thom and Head-Gordon have used SCF metadynamics[403] to obtain a basis of ΔHF reference states for CI calculations of

the ground and low-lying excited states of LiF and O_3.[293] These calculations suggest that multireference schemes based on ΔSCF states could be a practical complementary approach to CDFT-CI for obtaining ground and low-lying excited states with similar accuracy from a low-dimensional CI calculation. Future work should establish the strengths and weaknesses of ΔSCF states as a basis for multireference calculations.

8 Conclusion

The purpose of this review is threefold: to motivate and introduce the CDFT formalism; to summarize the diverse body of applications to date; and to offer some guidance to prospective users. There are likely dozens of creative ways that the ideas behind CDFT could be synthesized into new contexts and unexplored applications; thus, even when approximations to the XC functional eliminate the original motivating need for CDFT, we anticipate that the ideas presented in this review will retain much of their value for applications in other areas.

In this review, we emphasized the usefulness of CDFT as a practical strategy for several important problems. CDFT offers a degree of control over the effects of self-interaction error in approximate XC functionals, thereby combating the tendency of semilocal functionals to over-delocalize the density. The charge constraints in CDFT provide a natural way to define diabatic states for electron transfer with limited empiricism. These constraints also define a prescription for calculating the properties of certain excited states, such as charge-transfer and low-lying spin states, with ground-state DFT calculations. Couplings between CDFT states can be exploited to obtain accurate adiabatic states for systems with significant static correlation, and CDFT states and couplings can be exploited to construct physically motivated models of complex phenomena. Together, these features make CDFT a versatile and practical tool for modern density functional studies.

Several noteworthy limitations of CDFT were addressed in the preceding sections. CDFT applies real-space constraints on the density, and the constraints are defined by partitioning of the density according to an atomic population scheme. This introduces two ambiguities. First, assigning nuclei to the various constraint regions entails applying some degree of chemical intuition, and there may not be an obvious, unique, best choice for this partitioning. Second, the form of the constraint potential depends on the population scheme, and there is

some arbitrariness inherent in how any of these prescriptions carves up the density. From the perspective of obtaining excited-state information from ground state calculations, another major limitation of CDFT is that it can only describe a subset (albeit an important subset) of electronic excitations. Likewise, CDFT might not be the right tool for modeling certain diabatic states.

We close with some thoughts about future horizons for CDFT. Established evidence that CDFT provides a computationally efficient framework for modeling diabatic ET states should fuel further CDFT studies of ET in solution and of charge transport in OSCs, with the long-term goal of quantifying the energetics and kinetics of energy conversion from excitons. These simulations can inform the rational design of optimized artificial photosynthetic architectures and organic electronics, eventually advancing cheaper PV materials and brighter, more durable OLED displays. CDFT studies of ET processes in complex molecular architectures may also lead to improved chemical sensors and perhaps even to novel reactivity. Regarding the CDFT method itself, the most promising avenue for advances concerns the electronic coupling. What is the most accurate prescription for computing the coupling? Is there a more rigorous formulation waiting to be uncovered? What about derivatives of the electronic coupling? These are often assumed to be zero or negligibly small, and they are difficult to probe experimentally; but CDFT provides a way to quantify them in principle. Finally, there is ample room for more extensive application of CDFT and CDFT-CI to a range of important model and real-world problems: charge transport in graphene, exciton-CT dissociation kinetics, photochemical bleaching, proton-coupled electron transfer mechanisms, singlet fission, and double excitations are all tempting candidates for investigation with CDFT techniques. We anticipate that experimental and theoretical work on many of these problems — and many more we haven't conceived of — would benefit from the quantitative insights that CDFT has been shown to deliver.

9 Acknowledgment

This work was supported by a grant from the National Science Foundation (CHE-1058219). TK gratefully acknowledges a fellowship from the Chesonis Family Foundation. TV gratefully acknowledges a Packard Fellowship.

References

[1] Parr, R. G.; Yang, W. *Density-Functional Theory of Atoms and Molecules*; Oxford University Press: New York, 1989.

[2] Koch, W.; Holthausen, M. C. *A Chemist's Guide to Density Functional Theory*; Wiley-VCH: Weinheim, 2001.

[3] Hohenberg, P.; Kohn, W. *Phys. Rev.* **1964**, *136*, B864–B871.

[4] Kohn, W.; Sham, L. J. *Phys. Rev.* **1965**, *140*, A1133–A1138.

[5] Perdew, J. P.; Burke, K.; Ernzerhof, M. *Phys. Rev. Lett.* **1996**, *77*, 3865–3868.

[6] Becke, A. D. *J. Chem. Phys.* **1993**, *98*, 5648–5652.

[7] Zhao, Y.; Schultz, N. E.; Truhlar, D. G. *J. Chem. Theory Comput.* **2006**, *2*, 364–382.

[8] Ziegler, T. *Chem. Rev.* **1991**, *91*, 651–667.

[9] Parr, R. G.; Yang, W. *Annu. Rev. Phys. Chem.* **1995**, *46*, 701–728.

[10] Scuseria, G. E. *J. Phys. Chem. A* **1999**, *103*, 4782–4790.

[11] Schreckenbach, G.; Ziegler, T. *Theor. Chim. Acta* **1998**, *99*, 71–82.

[12] Saladino, A. C.; Larsen, S. C. *Catal. Today* **2005**, *105*, 122–133.

[13] Lin, Z. *Acc. Chem. Res.* **2010**, *43*, 602–611.

[14] Leopoldini, M.; Marino, T.; Michelini, M.; Rivalta, I.; Russo, N.; Sicilia, E.; Toscano, M. *Theor. Chim. Acta* **2007**, *117*, 765–779.

[15] Siegbahn, P. E. M.; Blomberg, M. R. A. *Chem. Rev.* **2000**, *100*, 421–437.

[16] Raugei, S.; Gervasio, F. L.; Carloni, P. *Phys. Stat. Sol. B* **2006**, *243*, 2500–2515.

[17] Riley, K. E.; Op't Holt, B. T.; Merz Jr., K. M. *J. Chem. Theory Comput.* **2007**, *3*, 407–433.

[18] Tuckerman, M. E.; Martyna, G. J. *J. Phys. Chem. B* **2000**, *104*, 159–178.

[19] Schlegel, H. B. *J. Comput. Chem.* **2003**, *24*, 1514–1527.

[20] Car, R.; Parrinello, M. *Phys. Rev. Lett.* **1985**, *55*, 2471–2474.

[21] Raugei, S.; Kim, D.; Klein, M. L. *Quant. Struct.-Act. Rel.* **2002**, *21*, 149–165.

[22] Iannuzzi, M.; Laio, A.; Parrinello, M. *Phys. Rev. Lett.* **2003**, *90*, 238302.

[23] Degtyarenko, I.; Biarnés, X.; Nieminen, R. M.; Rovira, C. *Coord. Chem. Rev.* **2008**, *252*, 1497–1513.

[24] Runge, E.; Gross, E. K. U. *Phys. Rev. Lett.* **1984**, *52*, 997–1000.

[25] Marques, M. A. L.; Gross, E. K. U. *Annu. Rev. Phys. Chem.* **2004**, *55*, 427–455.

[26] Dreuw, A.; Head-Gordon, M. *Chem. Rev.* **2005**, *105*, 4009–4037.

[27] Vicek Jr., A.; Zális, S. *Coord. Chem. Rev.* **2007**, *251*, 258–287.

[28] Senn, H. M.; Thiel, W. *Curr. Opin. Chem. Biol.* **2007**, *11*, 182–187.

[29] Curutchet, C.; Muñoz Losa, A.; Monti, S.; Kongsted, J.; Scholes, G. D.; Mennucci, B. *J. Chem. Theory Comput.* **2009**, *5*, 1838–1848.

[30] Olsen, J. M.; Aidas, K.; Kongsted, J. *J. Chem. Theory Comput.* **2010**, *6*, 3721–3734.

[31] Lanzani, G.; Martinazzo, R.; Materzanini, G.; Pino, I.; Tantardini, G. F. *Theor. Chim. Acta* **2007**, *117*, 805–825.

[32] Jacquemin, D.; Perpète, E. A.; Ciofini, I.; Adamo, C. *Acc. Chem. Res.* **2009**, *42*, 326–334.

[33] Singh, D. J.; Du, M. H. *Phys. Rev. Lett.* **2008**, *100*, 237003.

[34] Fantacci, S.; Amat, A.; Sgamellotti, A. *Acc. Chem. Res.* **2010**, *43*, 802–813.

[35] Vydrov, O. A.; Scuseria, G. E.; Perdew, J. P. *J. Chem. Phys.* **2007**, *126*, 154109.

[36] Cohen, A. J.; Mori-Sánchez, P.; Yang, W. *Science* **2008**, *321*, 792–794.

[37] Durant, J. L. *Chem. Phys. Lett.* **1996**, *256*, 595–602.

[38] Wu, Q.; Van Voorhis, T. *J. Phys. Chem. A* **2006**, *110*, 9212–9218.

[39] Rudra, I.; Wu, Q.; Van Voorhis, T. *J. Chem. Phys.* **2006**, *124*, 024103.

[40] Riley, K. E.; Pitoňák, M.; Jurecka, P.; Hobza, P. *Chem. Rev.* **2010**, *110*, 5023–5063.

[41] Lee, K.; Murray, E. D.; Kong, L. Z.; Lundqvist, B. I.; Langreth, D. C. *Phys. Rev. B* **2010**, *82*, 081101.

[42] Grimme, S.; Antony, J.; Ehrlich, S.; Krieg, H. *J. Chem. Phys.* **2010**, *132*, 154104.

[43] Vydrov, O. A.; Van Voorhis, T. *J. Chem. Phys.* **2010**, *133*, 244103.

[44] Dreuw, A.; Weisman, J. L.; Head-Gordon, M. *J. Chem. Phys.* **2003**, *119*, 2943–2946.

[45] Dreuw, A.; Head-Gordon, M. *J. Am. Chem. Soc.* **2004**, *126*, 4007–4016.

[46] Levine, B. G.; Ko, C.; Quenneville, J.; Martínez, T. J. *Mol. Phys.* **2006**, *104*, 1039–1051.

[47] Kaduk, B.; Van Voorhis, T. *J. Chem. Phys.* **2010**, *133*, 061102.

[48] Romaniello, P.; Sangalli, D.; Berger, J. A.; Sottile, F.; Molinari, L. G.; Reining, L.; Onida, G. *J. Chem. Phys.* **2009**, *130*, 044108.

[49] Furche, F. *J. Chem. Phys.* **2008**, *129*, 114105.

[50] Grimme, S.; Neese, F. *J. Chem. Phys.* **2007**, *127*, 154116.

[51] Dederichs, P. H.; Blugel, S.; Zeller, R.; Akai, H. *Phys. Rev. Lett.* **1984**, *53*, 2512–2515.

[52] Wu, Q.; Van Voorhis, T. *Phys. Rev. A* **2005**, *72*, 024502.

[53] Wu, Q.; Van Voorhis, T. *J. Chem. Theory Comput.* **2006**, *2*, 765–774.

[54] Wu, Q.; Voorhis, T. V. *J. Chem. Phys.* **2006**, *125*, 164105.

[55] Wu, Q.; Cheng, C.-L.; Voorhis, T. V. *J. Chem. Phys.* **2007**, *127*, 164119.

[56] Zhang, Z.; Satpathy, S. *Phys. Rev. B* **1991**, *44*, 13319–13331.

[57] Steiner, M. M.; Albers, R. C.; Sham, L. J. *Phys. Rev. B* **1992**, *45*, 13272–13284.

[58] Solovyev, I. V.; Dederichs, P. H. *Phys. Rev. B* **1994**, *49*, 6736–6740.

[59] Vielsack, G.; Weber, W. *Phys. Rev. B* **1996**, *54*, 6614–6623.

[60] Pickett, W. E.; Erwin, S. C.; Ethridge, E. C. *Phys. Rev. B* **1998**, *58*, 1201–1209.

[61] Schnell, I.; Czycholl, G.; Albers, R. C. *Phys. Rev. B* **2002**, *65*, 075103.

[62] Yaresko, A. N.; Antonov, V. N.; Fulde, P. *Phys. Rev. B* **2003**, *67*, 155103.

[63] Wierzbowska, M.; Delin, A.; Tosatti, E. *Phys. Rev. B* **2005**, *72*, 035439.

[64] Cococcioni, M.; de Gironcoli, S. *Phys. Rev. B* **2005**, *71*, 035105.

[65] Solovyev, I. V.; Imada, M. *Phys. Rev. B* **2005**, *71*, 045103.

[66] Nakamura, K.; Arita, R.; Yoshimoto, Y.; Tsuneyuki, S. *Phys. Rev. B* **2006**, *74*, 235113.

[67] Solovyev, I. V. *Phys. Rev. B* **2006**, *73*, 155117.

[68] Cano-Cortés, L.; Dolfen, A.; Merino, J.; Behler, J.; Delley, B.; Reuter, K.; Koch, E. *Eur. Phys. J. B* **2007**, *56*, 173–176.

[69] Tablero, C. *J. Phys. Condens. Matter* **2007**, *19*, 466209.

[70] Imai, Y.; Otsuka, Y.; Imada, M. *J. Phys. Condens. Matter* **2007**, *19*, 365230.

[71] Tablero, C. *J. Chem. Phys.* **2007**, *126*, 164703.

[72] Anisimov, V. I.; Zaanen, J.; Andersen, O. K. *Phys. Rev. B* **1991**, *44*, 943–954.

[73] Stefanou, N. *J. Phys. Condens. Matter* **1994**, *6*, 11221.

[74] Solovyev, I. V.; Dederichs, P. H.; Anisimov, V. I. *Phys. Rev. B* **1994**, *50*, 16861–16871.

[75] Satpathy, S.; Popović, Z. S.; Vukajlović, F. R. *Phys. Rev. Lett.* **1996**, *76*, 960–963.

[76] Pajda, M.; Kudrnovský, J.; Turek, I.; Drchal, V.; Bruno, P. *Phys. Rev. B* **2001**, *64*, 174402.

[77] Imai, Y.; Solovyev, I.; Imada, M. *Phys. Rev. Lett.* **2005**, *95*, 176405.

[78] Shorikov, A. O.; Lukoyanov, A. V.; Korotin, M. A.; Anisimov, V. I. *Phys. Rev. B* **2005**, *72*, 024458.

[79] Yamasaki, A.; Chioncel, L.; Lichtenstein, A. I.; Andersen, O. K. *Phys. Rev. B* **2006**, *74*, 024419.

[80] Anisimov, V.; Korotin, D.; Streltsov, S.; Kozhevnikov, A.; Kuneš, J.; Shorikov, A.; Korotin, M. *Sov. Phys. JETP Lett.* **2008**, *88*, 729–733.

[81] Anisimov, V. I.; Korotin, D. M.; Korotin, M. A.; Kozhevnikov, A. V.; Kune, J.; Shorikov, A. O.; Skornyakov, S. L.; Streltsov, S. V. *J. Phys. Condens. Matter* **2009**, *21*, 075602.

[82] Wang, Y.; Niranjan, M. K.; Burton, J. D.; An, J. M.; Belashchenko, K. D.; Tsymbal, E. Y. *Phys. Rev. B* **2009**, *79*, 212408.

[83] Shi, S.; Wysocki, A. L.; Belashchenko, K. D. *Phys. Rev. B* **2009**, *79*, 104404.

[84] Shorikov, A. O.; Pchelkina, Z. V.; Anisimov, V. I.; Skornyakov, S. L.; Korotin, M. A. *Phys. Rev. B* **2010**, *82*, 195101.

[85] Jiang, H.; Gomez-Abal, R. I.; Rinke, P.; Scheffler, M. *Phys. Rev. B* **2010**, *82*, 045108.

[86] An, J. M.; Barabash, S. V.; Ozolins, V.; van Schilfgaarde, M.; Belashchenko, K. D. *Phys. Rev. B* **2011**, *83*, 064105.

[87] Williams, A. R.; Moruzzi, V. L.; Kübler, J.; Schwarz, K. *Bull. Am. Phys. Soc.* **1984**, *29*, 278.

[88] Schwarz, K.; Mohn, P. *J. Phys. F: Met. Phys.* **1984**, *14*, L129.

[89] Moruzzi, V. L.; Marcus, P. M.; Schwarz, K.; Mohn, P. *Phys. Rev. B* **1986**, *34*, 1784–1791.

[90] Marcus, P. M.; Moruzzi, V. L. *J. Appl. Phys.* **1988**, *63*, 4045–4050.

[91] Stefanou, N.; Papanikolaou, N. *J. Phys. Condens. Matter* **1993**, *5*, 5663.

[92] Kurz, P.; Bihlmayer, G.; Blügel, S.; Hirai, K.; Asada, T. *Phys. Rev. B* **2001**, *63*, 096401.

[93] Kurz, P.; Förster, F.; Nordström, L.; Bihlmayer, G.; Blügel, S. *Phys. Rev. B* **2004**, *69*, 024415.

[94] Mryasov, O. N.; Nowak, U.; Guslienko, K. Y.; Chantrell, R. W. *Europhys. Lett.* **2005**, *69*, 805.

[95] Singer, R.; Fähnle, M.; Bihlmayer, G. *Phys. Rev. B* **2005**, *71*, 214435.

[96] Fähnle, M.; Singer, R.; Steiauf, D.; Antropov, V. P. *Phys. Rev. B* **2006**, *73*, 172408.

[97] Sandratskii, L. M.; Singer, R.; Şaşıoğlu, E. *Phys. Rev. B* **2007**, *76*, 184406.

[98] Singer, R.; Dietermann, F.; Steiauf, D.; Fähnle, M. *Phys. Rev. B* **2007**, *76*, 052403.

[99] Sandratskii, L. M. *Phys. Rev. B* **2008**, *78*, 094425.

[100] Steiauf, D.; Seib, J.; Fähnle, M. *Phys. Rev. B* **2008**, *78*, 020410.

[101] Honolka, J. et al. *Phys. Rev. B* **2009**, *79*, 104430.

[102] Seib, J.; Steiauf, D.; Fähnle, M. *Phys. Rev. B* **2009**, *79*, 064419.

[103] De Angeli, L.; Steiauf, D.; Singer, R.; Köberle, I.; Dietermann, F.; Fähnle, M. *Phys. Rev. B* **2009**, *79*, 052406.

[104] Saubanère, M.; Tanveer, M.; Ruiz-Díaz, P.; Pastor, G. M. *Phys. Stat. Sol. B* **2010**, *247*, 2610–2620.

[105] Cricchio, F.; Grånäs, O.; Nordström, L. *Phys. Rev. B* **2010**, *81*, 140403.

[106] Újfalussy, B.; Wang, X.-D.; Nicholson, D. M. C.; Shelton, W. A.; Stocks, G. M.; Wang, Y.; Gyorffy, B. L. *J. Appl. Phys.* **1999**, *85*, 4824–4826.

[107] Újfalussy, B.; Lazarovits, B.; Szunyogh, L.; Stocks, G. M.; Weinberger, P. *Phys. Rev. B* **2004**, *70*, 100404.

[108] Ghosh, S. K.; Singh, V. A. *J. Phys. Condens. Matter* **1989**, *1*, 1971.

[109] Astala, R.; Stott, M. J. *Phys. Rev. B* **2006**, *73*, 115127.

[110] Akai, H.; Blügel, S.; Zeller, R.; Dederichs, P. H. *Phys. Rev. Lett.* **1986**, *56*, 2407–2410.

[111] Pankratov, O.; Scheffler, M. *Phys. Rev. Lett.* **1995**, *75*, 701–704.

[112] Methfessel, M.; Fiorentini, V.; Oppo, S. *Phys. Rev. B* **2000**, *61*, 5229–5236.

[113] Fonseca, L. R. C.; Jimenez, J. L.; Leburton, J. P.; Martin, R. M. *Phys. Rev. B* **1998**, *57*, 4017–4026.

[114] Eriksson, O.; Wills, J. M.; Colarieti-Tosti, M.; Lebègue, S.; Grechnev, A. *Int. J. Quantum Chem.* **2005**, *105*, 160–165.

[115] Hourahine, B.; Aradi, B.; Frauenheim, T. *J. Phys. Conf. Ser.* **2010**, *242*, 012005.

[116] Voronoi, G. F. *J. Reine Angew. Math.* **1908**, *134*, 198–287.

[117] Becke, A. D. *J. Chem. Phys.* **1988**, *88*, 2547–2553.

[118] Hirshfeld, F. L. *Theor. Chim. Acta* **1977**, *44*, 129–138.

[119] Bultinck, P.; Alsenoy, C. V.; Ayers, P. W.; Carbó-Dorca, R. *J. Chem. Phys.* **2007**, *126*, 144111–1444119.

[120] Lillestolen, T. C.; Wheatley, R. J. *Chem. Commun.* **2008**, 5909–5911.

[121] Cohen, M. H.; Wasserman, A. *Israel J. Chem.* **2004**, *43*, 219–227.

[122] Cohen, M.; Wasserman, A. *J. Stat. Phys.* **2006**, *125*, 1121–1139.

[123] Cohen, M. H.; Wasserman, A. *J. Phys. Chem. A* **2007**, *111*, 2229–2242.

[124] Bader, R. *Atoms in molecules — a quantum theory*; Oxford University Press: Oxford, 1990.

[125] Mulliken, R. S. *J. Chem. Phys.* **1955**, *23*, 1833–1840.

[126] Löwdin, P. *J. Chem. Phys.* **1950**, *18*, 365–375.

[127] Foster, J. P.; Weinhold, F. *J. Am. Chem. Soc.* **1980**, *102*, 7211–7218.

[128] Reed, A. E.; Weinstock, R. B.; Weinhold, F. *J. Chem. Phys.* **1985**, *83*, 735–746.

[129] Chang, H.; Harrison, J. F.; Kaplan, T. A.; Mahanti, S. D. *Phys. Rev. B* **1994**, *49*, 15753–15758.

[130] Oberhofer, H.; Blumberger, J. *J. Chem. Phys.* **2009**, *131*, 064101.

[131] Johnson, B. G.; Gill, P. M. W.; Pople, J. A. *J. Chem. Phys.* **1993**, *98*, 5612–5626.

[132] Wu, Q.; Kaduk, B.; Voorhis, T. V. *J. Chem. Phys.* **2009**, *130*, 034109.

[133] Schlüter, M.; Varma, C. M. In *Valence Instabilities*; Wachter, P., Boppart, H., Eds.; North-Holland, 1982.

[134] Bringer, A. *Solid State Commun.* **1983**, *46*, 591–593.

[135] Yamaguchi, Y.; Yokoyama, S.; Mashiko, S. *J. Chem. Phys.* **2002**, *116*, 6541–6548.

[136] Iikura, H.; Tsuneda, T.; Yanai, T.; Hirao, K. *J. Chem. Phys.* **2001**, *115*, 3540–3544.

[137] Tawada, Y.; Tsuneda, T.; Yanagisawa, S.; Yanai, T.; Hirao, K. *J. Chem. Phys.* **2004**, *120*, 8425–8433.

[138] Gerber, I. C.; Angyan, J. G. *Chem. Phys. Lett.* **2005**, *415*, 100–105.

[139] Vydrov, O. A.; Heyd, J.; Krukau, A. V.; Scueria, G. E. *J. Chem. Phys.* **2006**, *125*, 074106.

[140] Baer, R.; Livshits, E.; Salzner, U. *Annu. Rev. Phys. Chem.* **2010**, *61*, 85–109.

[141] Marcus, R. A. *J. Chem. Phys.* **1956**, *24*, 966–978.

[142] Marcus, R. A. *Annu. Rev. Phys. Chem.* **1964**, *15*, 155–196.

[143] Barbara, P. F.; Meyer, T. J.; Ratner, M. A. *J. Phys. Chem. A* **1996**, *100*, 13148–13168.

[144] Bixon, M.; Jortner, J. *Adv. Chem. Phys.* **2007**, *106*, 35–202.

[145] Marcus, R. A. *Biochim. Biophys. Acta* **1985**, *811*, 265–322.

[146] Gould, I. R.; Noukakis, D.; Gomez-Jahn, L.; Young, R. H.; Goodman, J. L.; Farid, S. *Chem. Phys.* **1993**, *176*, 439–456.

[147] Schenter, G. K.; Garrett, B. C.; Truhlar, D. G. *J. Phys. Chem. B* **2001**, *105*, 9672–9685.

[148] Matyushov, D. V.; Voth, G. A. *Rev. Comp. Chem.* **2002**, *18*, 147–210.

[149] Gould, I. R.; Ege, D.; Moser, J. E.; Farid, S. *J. Am. Chem. Soc.* **1990**, *112*, 4290–4301.

[150] Matyushov, D. V.; Schmid, R. *J. Chem. Phys.* **1995**, *103*, 2034–2049.

[151] Doolen, R.; Simon, J. D.; Baldridge, K. K. *J. Phys. Chem.* **1995**, *99*, 13938–13947.

[152] Goeltz, J. C.; Benson, E. E.; Kubiak, C. P. *J. Phys. Chem. B* **2010**, *114*, 14729–14734.

[153] Nelsen, S. F.; Blackstock, S. C.; Kim, Y. *J. Am. Chem. Soc.* **1987**, *109*, 677–682.

[154] Van Voorhis, T.; Kowalczyk, T.; Kaduk, B.; Wang, L.-P.; Cheng, C.-L.; Wu, Q. *Annu. Rev. Phys. Chem.* **2010**, *61*, 149–170.

[155] Cave, R. J.; Newton, M. D. *Chem. Phys. Lett.* **1996**, *249*, 15–19.

[156] Warshel, A.; Weiss, R. M. *J. Am. Chem. Soc.* **1980**, *102*, 6218–6226.

[157] Wesolowski, T. A.; Warshel, A. *J. Phys. Chem.* **1993**, *97*, 8050–8053.

[158] Sit, P. H.-L.; Cococcioni, M.; Marzari, N. *Phys. Rev. Lett.* **2006**, *97*, 028303.

[159] Ghosh, P.; Gebauer, R. *J. Chem. Phys.* **2010**, *132*, 104102.

[160] Difley, S.; Wang, L.-P.; Yeganeh, S.; Yost, S. R.; Van Voorhis, T. *Acc. Chem. Res.* **2010**, *43*, 995–1004.

[161] Prezhdo, O. V.; Kindt, J. T.; Tully, J. C. *J. Chem. Phys.* **1999**, *111*, 7818–7827.

[162] Soudackov, A.; Hammes-Schiffer, S. *J. Am. Chem. Soc.* **1999**, *121*, 10598–10607.

[163] Robin, M. B.; Day, P. *Adv. Inorg. Chem. Radiochem.* **1968**, *10*, 247.

[164] Lu, Y. H.; Quardokus, R.; Lent, C. S.; Justaud, F.; Lapinte, C.; Kandel, S. A. *J. Am. Chem. Soc.* **2010**, *132*, 13519–13524.

[165] Gautier, N.; Dumur, F.; Lloveras, V.; Vidal-Gancedo, J.; Veciana, J.; Rovira, C.; Hudhomme, P. *Angew. Chem. Int. Ed.* **2003**, *42*, 2765–2768.

[166] Basilevsky, M. V.; Chudinov, G. E.; Rostov, I. V.; Liu, Y. P.; Newton, M. D. *J. Mol. Struct. (Theochem)* **1996**, *371*, 191–203.

[167] Cramer, C. J.; Truhlar, D. G. *Chem. Rev.* **1999**, *99*, 2161–2200.

[168] Aguilar, M. A. *J. Phys. Chem. A* **2001**, *105*, 10393–10396.

[169] Tomasi, J.; Mennucci, B.; Cammi, R. *Chem. Rev.* **2005**, *105*, 2999–3093.

[170] Klamt, A.; Schüürmann, G. *J. Chem. Soc., Perkin Trans. 2* **1993**, 799–805.

[171] Okamoto, K.; Hasobe, T.; Tkachenko, N. V.; Lemmetyinen, H.; Kamat, P. V.; Fukuzumi, S. *J. Phys. Chem. A* **2005**, *109*, 4662–4670.

[172] Van Ramesdonk, H. J.; Bakker, B. H.; Groeneveld, M. M.; Verhoeven, J. W.; Allen, B. D.; Rostron, J. P.; Harriman, A. *J. Phys. Chem. A* **2006**, *110*, 13145–13150.

[173] Hwang, J.-K.; Warshel, A. *J. Am. Chem. Soc.* **1987**, *109*, 715–720.

[174] Tachiya, M. *J. Chem. Phys.* **2008**, *129*, 066102.

[175] Kuharski, R. A.; Bader, J. S.; Chandler, D.; Sprik, M.; Klein, M. L.; Impey, R. W. *J. Chem. Phys.* **1988**, *89*, 3248–2357.

[176] Carter, E. A.; Hynes, J. T. *J. Phys. Chem.* **1989**, *93*, 2184–2187.

[177] Blumberger, J. *Phys. Chem. Chem. Phys.* **2008**, *10*, 5652–5667.

[178] Blumberger, J.; Lamoureux, G. *Mol. Phys.* **2008**, *106*, 1597–1611.

[179] Bernhard, P.; Helm, L.; Ludi, A.; Merbach, A. E. *J. Am. Chem. Soc.* **1985**, *107*, 312–317.

[180] Hu, H.; Yang, W. *Annu. Rev. Phys. Chem.* **2008**, *59*, 573–601.

[181] Strader, M. L.; Feller, S. E. *J. Phys. Chem. A* **2002**, *106*, 1074–1080.

[182] Lamoureux, G.; Roux, B. *J. Chem. Phys.* **2003**, *119*, 3025–3039.

[183] Kowalczyk, T.; Wang, L.-P.; Van Voorhis, T. *submitted*.

[184] Hoekstra, R. M.; Telo, J. P.; Wu, Q.; Stephenson, R. M.; Nelsen, S. F.; Zink, J. I. *J. Am. Chem. Soc.* **2010**, *132*, 8825–8827.

[185] Nelsen, S. F.; Weaver, M. N.; Telo, J. P. *J. Am. Chem. Soc.* **2007**, *129*, 7036–7043.

[186] Callan, J. F.; de Silva, A. P.; Magri, D. C. *Tetrahedron* **2005**, *61*, 8551–8588.

[187] Kowalczyk, T.; Lin, Z.; Van Voorhis, T. *J. Phys. Chem. A* **2010**, *114*, 10427–10434.

[188] Blundell, S. J. *Contemp. Phys.* **2007**, *48*, 275–290.

[189] Hayashi, H. *J. Chinese Chem. Soc.* **2002**, *49*, 137–160.

[190] Shuai, Z.; Beljonne, D.; Silbey, R. J.; Brédas, J. L. *Phys. Rev. Lett.* **2000**, *84*, 131–134.

[191] Heisenberg, W. *Z. Phys.* **1928**, *49*, 619–636.

[192] Bastardis, R.; Guihèry, N.; de Graaf, C. *J. Chem. Phys.* **2008**, *129*, 104102.

[193] Nesbet, R. K. *Phys. Rev.* **1961**, *122*, 1497–1508.

[194] Clark, A. E.; Davidson, E. R. *J. Chem. Phys.* **2001**, *115*, 7382–7392.

[195] Reiher, M. *Faraday Disc.* **2007**, *135*, 97–124.

[196] Behler, J.; Delley, B.; Lorenz, S.; Reuter, K.; Scheffler, M. *Phys. Rev. Lett.* **2005**, *94*, 036104.

[197] Österlund, L.; Zorić, I.; Kasemo, B. *Phys. Rev. B* **1997**, *55*, 15452–15455.

[198] Honkala, K.; Laasonen, K. *Phys. Rev. Lett.* **2000**, *84*, 705–708.

[199] Yourdshahyan, Y.; Razaznejad, B.; Lundqvist, B. *Phys. Rev. B* **2002**, *65*, 075416.

[200] Behler, J.; Reuter, K.; Scheffler, M. *Phys. Rev. B* **2008**, *77*, 115421.

[201] Lorenz, S.; Gross, A.; Scheffler, M. *Chem. Phys. Lett.* **2004**, *395*, 210–215.

[202] Lorenz, S.; Scheffler, M.; Gross, A. *Phys. Rev. B* **2006**, *73*, 115431.

[203] Carbogno, C.; Behler, J.; Reuter, K.; Gross, A. *Phys. Rev. B* **2010**, *81*, 035410.

[204] Yuan, Q. H.; Li, J. B.; Fan, X. L.; Lau, W. M.; Liu, Z. F. *Chem. Phys. Lett.* **2010**, *489*, 16–19.

[205] Olsen, T.; Schiøtz, J. *J. Chem. Phys.* **2010**, *133*, 134109.

[206] Blundell, S. J.; Pratt, F. L. *J. Phys. Condens. Matter* **2004**, *16*, R771–R828.

[207] *Molecular Magnetism: From Molecular Assemblies to the Devices*; Coronado, E., Delhaès, P., Gatteschi, D., Miller, J. S., Eds.; Springer: New York, 2010.

[208] Friedman, J. R.; Sarachik, M. P. *Annu. Rev. Condens. Matter Phys.* **2010**, *1*, 109–128.

[209] Noodleman, L. *J. Chem. Phys.* **1981**, *74*, 5737–5743.

[210] Ruiz, E.; Cano, J.; Alvarez, S.; Alemany, P. *J. Comput. Chem.* **1999**, *20*, 1391–1400.

[211] Nishino, M.; Yamanaka, S.; Yoshioka, Y.; Yamaguchi, K. *J. Phys. Chem. A* **1997**, *101*, 705–712.

[212] Noodleman, L.; Baerends, E. J. *J. Am. Chem. Soc.* **1984**, *106*, 2316–2327.

[213] Yamanaka, S.; Kawakami, T.; Nagao, H.; Yamaguchi, K. *Chem. Phys. Lett.* **1994**, *231*, 25–33.

[214] Calzado, C. J.; Cabrero, J.; Malrieu, J. P.; Caballol, R. *J. Chem. Phys.* **2002**, *116*, 3985–4000.

[215] von Barth, U. *Phys. Rev. A* **1979**, *20*, 1693–1703.

[216] Song, H. H.; Zheng, L. M.; Liu, Y. J.; Xin, X. Q.; Jacobson, A. J.; Decurtins, S. *J. Chem. Soc., Dalton Trans.* **2001**, *22*, 3274–3278.

[217] Felthouse, T. R.; Laskowski, E. D.; Hendrickson, D. N. *Inorg. Chem* **1977**, *16*, 1077–1089.

[218] Mathoniere, C.; Kahn, O.; Daran, J. C.; Hilbig, H.; Kohler, F. H. *Inorg. Chem* **1993**, *32*, 4057–4062.

[219] Sun, Y.; Melchior, M.; Summers, D. A.; Thompson, R. C.; Rettig, S. J.; Orvig, C. *Inorg. Chem* **1998**, *37*, 3119–3121.

[220] Haselhorst, G.; Wieghardt, K.; Keller, S.; Schrader, B. *Inorg. Chem* **1993**, *32*, 520–525.

[221] Sinnecker, S.; Neese, F.; Noodleman, L.; Lubitz, W. *J. Am. Chem. Soc.* **2004**, *126*, 2613–2622.

[222] Tandon, S. S.; Thompson, L. K.; Manuel, M. E.; Bridson, J. N. *Inorg. Chem* **1994**, *33*, 5555–5570.

[223] Julve, M.; Lloret, F.; Faus, F.; Verdaguer, M.; Caneschi, A. *Inorg. Chem* **1995**, *34*, 157–165.

[224] Birkelbach, F.; Winter, M.; Flörke, U.; Haupt, H. J.; Butzlaff, C.; Lengen, M.; Bill, E.; Trautwein, A. X.; Weighardt, K.; Chaudhuri, P. *Inorg. Chem* **1994**, *33*, 3990–4001.

[225] Rudra, I.; Wu, Q.; Van Voorhis, T. *Inorg. Chem* **2007**, *46*, 10539–10548.

[226] Pontillon, Y.; Caneschi, A.; Gatteschi, D.; Sessoli, R.; Ressouche, E.; Schweizer, J.; Lelievre-Berna, E. *J. Am. Chem. Soc.* **1999**, *121*, 5342–5343.

[227] Furukawa, Y.; Kawakami, S.; Kumagai, K.; Baek, S. H.; Borsa, F. *Phys. Rev. B* **2003**, *68*, 180405.

[228] Cao, Y.; Parker, I. D.; Yu, G.; Zhang, C.; Heeger, A. J. *Nature* **1999**, *397*, 414–417.

[229] Wilson, J. S.; Dhoot, A. S.; Seeley, A. J. A. B.; Khan, M. S.; Kohler, A.; Friend, R. H. *Nature* **2001**, *413*, 828–831.

[230] Wohlgenannt, M.; Jiang, X. M.; Vardeny, Z. V.; Janssen, R. A. J. *Phys. Rev. Lett.* **2002**, *88*, 197401.

[231] Difley, S.; Beljonne, D.; Van Voorhis, T. *J. Am. Chem. Soc.* **2008**, *130*, 3420–3427.

[232] Wohlgenannt, M.; Vardeny, Z. V.; Shi, J.; Francis, T. L.; Jiang, X. M.; Mermer, O.; Veeraraghavan, G.; Wu, D.; Xiong, Z. H. *IEE Proc.-Circuits Devices Syst.* **2005**, *152*, 385–392.

[233] Verhoeven, J. W. *J. Photochem. Photobiol. C* **2006**, *7*, 40–60.

[234] Holmes, R. J.; Forrest, S. R.; Tung, Y. J.; Kwong, R. C.; Brown, J. J.; Garon, S.; Thompson, M. E. *Appl. Phys. Lett.* **2003**, *82*, 2422–2424.

[235] Segal, M.; Singh, M.; Rivoire, K.; Difley, S.; Van Voorhis, T.; Baldo, M. A. *Nat. Mater.* **2007**, *6*, 374–378.

[236] Miura, T.; Carmieli, R.; Wasielewski, M. R. *J. Phys. Chem. A* **2010**, *114*, 5769–5778.

[237] Wegner, M.; Fischer, H.; Grosse, S.; Vieth, H. M.; Oliver, A. M.; Paddon-Row, M. N. *Chem. Phys.* **2001**, *264*, 341–353.

[238] Schmidt, J. R.; Shenvi, N.; Tully, J. C. *J. Chem. Phys.* **2008**, *129*, 114110.

[239] Wang, J. H.; Becke, A. D.; Smith, V. H. *J. Chem. Phys.* **1995**, *102*, 3477–3480.

[240] Anderson, P. W. *Concepts in Solids*; World Scientific: Singapore, 1997.

[241] Köhler, H.; Sticht, J.; Kübler, J. *Physica B* **1991**, *172*, 79–84.

[242] Stocks, G. M.; Ujfalussy, B.; Wang, X.; Nicholson, D. M. C.; Shelton, W. A.; Wang, Y.; Canning, A.; Gyöffry, B. L. *Philos. Mag. B* **1998**, *78*, 665–673.

[243] Gebauer, R.; Baroni, S. *Phys. Rev. B* **2000**, *61*, R6459–R6462.

[244] Aaqvist, J.; Warshel, A. *Chem. Rev.* **1993**, *93*, 2523–2544.

[245] Subotnik, J. E.; Yeganeh, S.; Cave, R. J.; Ratner, M. A. *J. Chem. Phys.* **2008**, *129*, 244101.

[246] Pacher, T.; Cederbaum, L. S.; Köppel, H. *J. Chem. Phys.* **1988**, *89*, 7367–7381.

[247] Kim, H. J.; Hynes, J. T. *J. Am. Chem. Soc.* **1992**, *114*, 10508–10528.

[248] Pacher, T.; Köppel, H.; Cederbaum, L. S. *J. Chem. Phys.* **1991**, *95*, 6668–6680.

[249] Pacher, T.; Cederbaum, L.; Köppel, H. *Adv. Chem. Phys.* **1993**, *84*, 293–391.

[250] Nakamura, H.; Truhlar, D. G. *J. Chem. Phys.* **2001**, *115*, 10353–10372.

[251] Nakamura, H.; Truhlar, D. G. *J. Chem. Phys.* **2002**, *117*, 5576–5593.

[252] Nakamura, H.; Truhlar, D. G. *J. Chem. Phys.* **2003**, *118*, 6816–6829.

[253] Cattaneo, P.; Persico, M. *Chem. Phys.* **1997**, *214*, 49–60.

[254] Ruedenberg, K.; Atchity, G. J. *J. Chem. Phys.* **1993**, *99*, 3799–3803.

[255] Atchity, G. J.; Ruedenberg, K. *Theor. Chim. Acta* **1997**, *97*, 47–58.

[256] Cave, R. J.; Newton, M. D. *J. Chem. Phys.* **1997**, *106*, 9213–9226.

[257] Pacher, T.; Mead, C. A.; Cederbaum, L. S.; Köppel, H. *J. Chem. Phys.* **1989**, *91*, 7057–7062.

[258] Thiel, A.; Köppel, H. *J. Chem. Phys.* **1999**, *110*, 9371–9383.

[259] Köppel, H.; Gronki, J.; Mahapatra, S. *J. Chem. Phys.* **2001**, *115*, 2377–2388.

[260] Song, L.; Gao, J. *J. Phys. Chem. A* **2008**, *112*, 12925–12935.

[261] Mo, Y.; Gao, J. *J. Phys. Chem. A* **2000**, *104*, 3012–3020.

[262] Difley, S.; Voorhis, T. V. *J. Chem. Theory Comput.* **2011**, *7*, 594–601.

[263] Zhu, X.-Y.; Yang, Q.; Muntwiler, M. *Acc. Chem. Res.* **2009**, *42*, 1779–1787.

[264] Coropceanu, V.; Cornil, J.; da Silva Filho, D. A.; Olivier, Y.; Silbey, R.; Brédas, J.-L. *Chem. Rev.* **2007**, *107*, 926–952.

[265] Ding, F.; Wang, H.; Wu, Q.; Van Voorhis, T.; Chen, S.; Konopelski, J. P. *J. Phys. Chem. A* **2010**, *114*, 6039–6046.

[266] Hush, N. S. *J. Chem. Phys.* **1958**, *28*, 962–972.

[267] Hush, N. S. *Chem. Phys.* **1975**, *10*, 361–366.

[268] Creutz, C.; Newton, M. D.; Sutin, N. *J. Photochemistry and Photobiology A: Chemistry* **1994**, *82*, 47–59.

[269] Yeganeh, S.; Van Voorhis, T. *J. Phys. Chem. C* **2010**, *114*, 20756–20763.

[270] Silbey, R. *Annu. Rev. Phys. Chem.* **1976**, *27*, 203–223.

[271] Dexter, D. L. *J. Chem. Phys.* **1953**, *21*, 836–850.

[272] Oberhofer, H.; Blumberger, J. *J. Chem. Phys.* **2010**, *133*, 244105.

[273] Mikkelsen, K. V.; Ratner, M. A. *Chem. Rev.* **1987**, *87*, 113–153.

[274] McConnell, H. M. *J. Chem. Phys.* **1961**, *35*, 508–515.

[275] Hoffmann, R.; Imamura, A.; Hehre, W. J. *J. Am. Chem. Soc.* **1968**, *90*, 1499–1509.

[276] Sidis, V.; Kubach, C.; Fussen, D. *Phys. Rev. A* **1983**, *27*, 2431–2446.

[277] Paulson, B. P.; Curtiss, L. A.; Bal, B.; Closs, G. L.; Miller, J. R. *J. Am. Chem. Soc.* **1996**, *118*, 378–387.

[278] Hsu, C.-P.; Fleming, G. R.; Head-Gordon, M.; Head-Gordon, T. *J. Chem. Phys.* **2001**, *114*, 3065–3072.

[279] Kurlancheek, W.; Cave, R. J. *J. Phys. Chem. A* **2006**, *110*, 14018–14028.

[280] Mori-Sánchez, P.; Cohen, A. J.; Yang, W. *Phys. Rev. Lett.* **2008**, *100*, 146401.

[281] Sponer, H.; Teller, E. *Rev. Mod. Phys.* **1941**, *13*, 75.

[282] Casida, M. E. In *Time-Dependnet Density Functional Response Theory for Molecules*; World Scientific, 1995; pp 155–192.

[283] Thouless, D. J. *Nucl. Phys.* **1960**, *21*, 225–232.

[284] Smith, F. T. *Phys. Rev.* **1969**, *179*, 111–123.

[285] Baer, M. *Chem. Phys. Lett.* **1975**, *35*, 112 – 118.

[286] Mead, C. A.; Truhlar, D. G. *J. Chem. Phys.* **1982**, *77*, 6090–6098.

[287] Zener, C. *P. R. Soc. London* **1932**, *137*, 696–702.

[288] Gadéa, F. X.; Pélissier, M. *J. Chem. Phys.* **1990**, *93*, 545–551.

[289] Domcke, W.; Woywod, C.; Stengle, M. *Chem. Phys. Lett.* **1994**, *226*, 257–262.

[290] Liyanage, R.; Gordon, R. J.; Field, R. W. *J. Chem. Phys.* **1998**, *109*, 8374–8387.

[291] Farazdel, A.; Dupuis, M.; Clementi, E.; Aviram, A. *J. Am. Chem. Soc.* **1990**, *112*, 4206–4214.

[292] Logan, J.; Newton, M. D. *J. Chem. Phys.* **1983**, *78*, 4086–4091.

[293] Thom, A. J. W.; Head-Gordon, M. *J. Chem. Phys.* **2009**, *131*, 124113.

[294] Kaduk, B.; Voorhis, T. V. *in preparation*.

[295] Yarkony, D. R. *Rev. Mod. Phys.* **1996**, *68*, 985.

[296] Coe, J. D.; Martínez, T. J. *J. Phys. Chem. A* **2006**, *110*, 618–630.

[297] Migliore, A.; Corni, S.; Felice, R. D.; Molinari, E. *J. Chem. Phys.* **2006**, *124*, 064501.

[298] Migliore, A. *J. Chem. Phys.* **2009**, *131*, 114113.

[299] Lemaur, V.; Steel, M.; Beljonne, D.; Brédas, J.-L.; Cornil, J. *J. Am. Chem. Soc.* **2005**, *127*, 6077–6086.

[300] Takiff, L.; Boxer, S. G. *J. Am. Chem. Soc.* **1988**, *110*, 4425–4426.

[301] Gust, D.; Moore, T. A.; Moore, A. L. *Acc. Chem. Res.* **1993**, *26*, 198–205.

[302] Cohen, A. J.; Mori-Sánchez, P.; Yang, W. *J. Chem. Phys.* **2008**, *129*, 121104.

[303] Gustafsson, G.; Treacy, G.; Cao, Y.; Klavetter, F.; Colaneri, N.; Heeger, A. *Synthetic Metals* **1993**, *57*, 4123–4127.

[304] Park, S. H.; Roy, A.; Beaupre, S.; Cho, S.; Coates, N.; Moon, J. S.; Moses, D.; Leclerc, M.; Lee, K.; Heeger, A. J. *Nat. Photonics* **2009**, *3*, 297–302.

[305] Kwiatkowski, J. J.; Nelson, J.; Li, H.; Bredas, J. L.; Wenzel, W.; Lennartz, C. *Phys. Chem. Chem. Phys.* **2008**, *10*, 1852–1858.

[306] Vura-Weis, J.; Newton, M. D.; Wasielewski, M. R.; Subotnik, J. E. *J. Phys. Chem. C* **2010**, *114*, 20449–20460.

[307] Kamerlin, S. C. L.; Warshel, A. *WIREs Comput. Mol. Sci.* **2011**, *1*, 30–45.

[308] Van Vleck, J. H. *Phys. Rev.* **1929**, *33*, 467–506.

[309] Anderson, P. W.; Baskaran, G.; Zou, Z.; Hsu, T. *Phys. Rev. Lett.* **1987**, *58*, 2790–2793.

[310] Zhang, F. C.; Rice, T. M. *Phys. Rev. B* **1988**, *37*, 3759–3761.

[311] Pariser, R.; Parr, R. G. *J. Chem. Phys.* **1953**, *21*, 466–471.

[312] Pople, J. A. *Trans. Faraday Soc.* **1953**, *49*, 1375–1385.

[313] Feiguin, A.; Gazza, C. J.; Trumper, A. E.; Ceccatto, H. A. *J. Phys. Condens. Matter* **1997**, *9*, L27–L32.

[314] Georges, A.; Kotliar, G.; Krauth, W.; Rozenberg, M. J. *Rev. Mod. Phys.* **1996**, *68*, 13.

[315] Koolhaas, M.; van Mourik, F.; van der Zwan, G.; van Grondelle, R. *J. Luminescence* **1994**, *60-61*, 515–519.

[316] Foulkes, W. M. C.; Haydock, R. *Phys. Rev. B* **1989**, *39*, 12520–12536.

[317] Sankey, O. F.; Niklewski, D. J. *Phys. Rev. B* **1989**, *40*, 3979–3995.

[318] Meider, H.; Springborg, M. *J. Phys. Condens. Matter* **1998**, *10*, 6953–6971.

[319] Meider, H.; Springborg, M. *Chem. Phys. Lett.* **1999**, *300*, 339–345.

[320] Gunnarsson, O.; Andersen, O. K.; Jepsen, O.; Zaanen, J. *Phys. Rev. B* **1989**, *39*, 1708–1722.

[321] Hybertsen, M. S.; Schlüter, M.; Christensen, N. E. *Phys. Rev. B* **1989**, *39*, 9028–9041.

[322] Evans, J. S.; Cheng, C.-L.; Van Voorhis, T. *Phys. Rev. B* **2008**, *78*, 165108.

[323] Petukhov, A. G.; Mazin, I. I.; Chioncel, L.; Lichtenstein, A. I. *Phys. Rev. B* **2003**, *67*, 153106.

[324] Nakamura, K.; Yoshimoto, Y.; Arita, R.; Tsuneyuki, S.; Imada, M. *Phys. Rev. B* **2008**, *77*, 195126.

[325] Ashcroft, N. W.; Mermin, N. D. *Solid State Physics*; Brooks Cole, 1976.

[326] Miller, A.; Abrahams, E. *Phys. Rev.* **1960**, *120*, 745–755.

[327] Anderson, P. W. *Phys. Rev.* **1958**, *109*, 1492–1505.

[328] Anisimov, V. I.; Aryasetiawan, F.; Lichtenstein, A. I. *J. Phys. Condens. Matter* **1997**, *9*, 767.

[329] Danielsen, P. L. *J. Phys. C: Solid State Phys.* **1986**, *19*, L741.

[330] Basescu, N.; Liu, Z.-X.; Moses, D.; Heeger, A. J.; Naarmann, N.; Theophilou, N. *Nature* **1987**, *327*, 403–405.

[331] Honecker, A.; Meier, F.; Loss, D.; Normand, B. *Eur. Phys. J. B* **2002**, *27*, 487–495.

[332] Mohn, P.; Persson, C.; Blaha, P.; Schwarz, K.; Novák, P.; Eschrig, H. *Phys. Rev. Lett.* **2001**, *87*, 196401.

[333] Mataga, N.; Nishimoto, K. *Z. Phys. Chem. Neue Fol.* **1957**, *13*, 140–157.

[334] Hill, D. L.; Wheeler, J. A. *Phys. Rev.* **1953**, *89*, 1102–1145.

[335] Griffin, J. J.; Wheeler, J. A. *Phys. Rev.* **1957**, *108*, 311–327.

[336] Capelle, K. *J. Chem. Phys.* **2003**, *119*, 1285–1288.

[337] Orestes, E.; Capelle, K.; da Silva, A. B. F.; Ullrich, C. A. *J. Chem. Phys.* **2007**, *127*, 124101.

[338] Mott, N. *Proc. Phys. Soc. A* **1949**, *62*, 416.

[339] Colle, R.; Salvetti, O. *J. Chem. Phys.* **1983**, *79*, 1404–1407.

[340] Becke, A. D. *J. Chem. Phys.* **2003**, *119*, 2972–2977.

[341] Zhao, Y.; González-García, N.; Truhlar, D. G. *J. Phys. Chem. A* **2005**, *109*, 2012–2018.

[342] Viegas, L. P.; Branco, A.; Varandas, A. J. C. *J. Chem. Theory Comput.* **2010**, *6*, 2751–2761.

[343] Fuchs, M.; Niquet, Y.-M.; Gonze, X.; Burke, K. *J. Chem. Phys.* **2005**, *122*, 094116.

[344] Valone, S.; Levy, M. *Phys. Rev. A* **2009**, *80*, 042501.

[345] Matsika, S. In *Conical Intersections in Molecular Systems*; John Wiley & Sons, Inc., 2007; pp 83–124.

[346] Dutoi, A. D.; Head-Gordon, M. *Chem. Phys. Lett.* **2006**, *422*, 230–233.

[347] Werner, H.-J.; Meyer, W. *J. Chem. Phys.* **1981**, *74*, 5802–5807.

[348] Gräfenstein, J.; Cremer, D. *Chem. Phys. Lett.* **2000**, *316*, 569–577.

[349] Zhang, Y.; Yang, W. *J. Chem. Phys.* **1998**, *109*, 2604–2608.

[350] III, G. D. P.; Bartlett, R. J. *J. Chem. Phys.* **1982**, *76*, 1910–1918.

[351] Sherrill, C. D.; Krylov, A. I.; Byrd, E. F. C.; Head-Gordon, M. *J. Chem. Phys.* **1998**, *109*, 4171–4181.

[352] Lynch, B. J.; Fast, P. L.; Harris, M.; Truhlar, D. G. *J. Phys. Chem. A* **2000**, *104*, 4811–4815.

[353] Perdew, J. P.; Levy, M. *Phys. Rev. B* **1997**, *56*, 16021–16028.

[354] Ruzsinszky, A.; Perdew, J. P.; Csonka, G. I.; Vydrov, O. A.; Scuseria, G. E. *J. Chem. Phys.* **2007**, *126*, 104102.

[355] Mori-Sánchez, P.; Cohen, A. J.; Yang, W. *J. Chem. Phys.* **2006**, *125*, 201102.

[356] Burroughes, J. H.; Bradley, D. D. C.; Brown, A. R.; Marks, R. N.; Mackay, K.; Friend, R. H.; Burns, P. L.; Holmes, A. B. *Nature* **1990**, *347*, 539–541.

[357] Irie, M.; Fukaminato, T.; Sasaki, T.; Tamai, N.; Kawai, T. *Nature* **2002**, *420*, 759–760.

[358] Shaheen, S. E.; Brabec, C. J.; Sariciftci, N. S.; Padinger, F.; Fromherz, T.; Hummelen, J. C. *Appl. Phys. Lett.* **2001**, *78*, 841–843.

[359] Lautenschlager, P.; Garriga, M.; Logothetidis, S.; Cardona, M. *Phys. Rev. B* **1987**, *35*, 9174–9189.

[360] Aspnes, D. E.; Studna, A. A. *Phys. Rev. B* **1983**, *27*, 985.

[361] Pople, J. A.; Santry, D. P.; Segal, G. A. *J. Chem. Phys.* **1965**, *43*, S129–S135.

[362] Pople, J. A.; Segal, G. A. *J. Chem. Phys.* **1965**, *43*, S136–S151.

[363] Marzari, N.; Vanderbilt, D. *Phys. Rev. B* **1997**, *56*, 12847–12865.

[364] Souza, I.; Marzari, N.; Vanderbilt, D. *Phys. Rev. B* **2001**, *65*, 035109.

[365] Yeganeh, S.; Wasielewski, M. R.; Ratner, M. A. *J. Am. Chem. Soc.* **2009**, *131*, 2268–2273.

[366] Perdew, J. P.; Zunger, A. *Phys. Rev. B* **1981**, *23*, 5048–5079.

[367] Perdew, J. P.; Parr, R. G.; Levy, M.; Balduz, J. L. *Phys. Rev. Lett.* **1982**, *49*, 1691–1694.

[368] Perdew, J. P.; Ruzsinszky, A.; Constantin, L. A.; Sun, J.; Csonka, G. I. *J. Chem. Theory Comput.* **2009**, *5*, 902–908.

[369] Kümmel, S.; Kronik, L. *Rev. Mod. Phys.* **2008**, *80*, 3–60.

[370] Goedecker, S.; Umrigar, C. J. *Phys. Rev. A* **1997**, *55*, 1765–1771.

[371] Vydrov, O. A.; Scuseria, G. E.; Perdew, J. P.; Ruzsinszky, A.; Csonka, G. I. *J. Chem. Phys.* **2006**, *124*, 094108.

[372] Stengel, M.; Spaldin, N. A. *Phys. Rev. B* **2008**, *77*, 155106.

[373] Unger, H.-J. *Phys. Lett. A* **2001**, *284*, 124–129.

[374] Nekrasov, I. A.; Streltsov, S. V.; Korotin, M. A.; Anisimov, V. I. *Phys. Rev. B* **2003**, *68*, 235113.

[375] Zhou, F.; Cococcioni, M.; Marianetti, C. A.; Morgan, D.; Ceder, G. *Phys. Rev. B* **2004**, *70*, 235121.

[376] Sit, P. H.-L.; Cococcioni, M.; Marzari, N. *J. Electroanal. Chem.* **2007**, *607*, 107–112.

[377] Scherlis, D. A.; Cococcioni, M.; Sit, P.; Marzari, N. *J. Phys. Chem. B* **2007**, *111*, 7384–7391.

[378] Casolo, S.; Flage-Larsen, E.; Lovvik, O. M.; Darling, G. R.; Tantardini, G. F. *Phys. Rev. B* **2010**, *81*, 205412.

[379] Rohrdanz, M. A.; Herbert, J. M. *J. Chem. Phys.* **2008**, *129*, 034107.

[380] Leininger, T.; Stoll, H.; Werner, H. J.; Savin, A. *Chem. Phys. Lett.* **1997**, *275*, 151–160.

[381] Mo, Y.; Song, L.; Lin, Y. *J. Phys. Chem. A* **2007**, *111*, 8291–8301.

[382] Khaliullin, R. Z.; Head-Gordon, M.; Bell, A. T. *J. Chem. Phys.* **2006**, *124*, 204105.

[383] Cembran, A.; Song, L.; Mo, Y.; Gao, J. *J. Chem. Theory Comput.* **2009**, *5*, 2702–2716.

[384] Gao, J. *J. Phys. Chem. B* **1997**, *101*, 657–663.

[385] Gao, J. *J. Chem. Phys.* **1998**, *109*, 2346–2354.

[386] Xie, W.; Gao, J. *J. Chem. Theory Comput.* **2007**, *3*, 1890–1900.

[387] Mo, Y.; Bao, P.; Gao, J. *Phys. Chem. Chem. Phys.* **2011**, *13*, 6760–6775.

[388] Khaliullin, R. Z.; Bell, A. T.; Head-Gordon, M. *Chem. Eur. J.* **2009**, *15*, 851–855.

[389] Khaliullin, R. Z.; Cobar, E. A.; Lochan, R. C.; Bell, A. T.; Head-Gordon, M. *J. Phys. Chem. A* **2007**, *111*, 8753–8765.

[390] Khaliullin, R. Z.; Bell, A. T.; Head-Gordon, M. *J. Chem. Phys.* **2008**, *128*, 184112.

[391] Görling, A. *Phys. Rev. A* **1999**, *59*, 3359–3374.

[392] Levy, M.; Nagy, A. *Phys. Rev. Lett.* **1999**, *83*, 4361–4364.

[393] Gaudoin, R.; Burke, K. *Phys. Rev. Lett.* **2004**, *93*, 173001.

[394] Ayers, P. W.; Levy, M. *Phys. Rev. A* **2009**, *80*, 012508.

[395] Ziegler, T.; Rauk, A.; Baerends, E. J. *Theor. Chim. Acta* **1977**, *43*, 261–271.

[396] Gavnholt, J.; Olsen, T.; Engelund, M.; Schiotz, J. *Phys. Rev. B* **2008**, *78*, 075441.

[397] Cheng, C.-L.; Wu, Q.; Van Voorhis, T. *J. Chem. Phys.* **2008**, *129*, 124112.

[398] Artacho, E.; Rohlfing, M.; Cote, M.; Haynes, P. D.; Needs, R. J.; Molteni, C. *Phys. Rev. Lett.* **2004**, *93*, 116401.

[399] Tiago, M. L.; Ismail-Beigi, S.; Louie, S. G. *J. Chem. Phys.* **2005**, *122*, 094311.

[400] Billeter, S. R.; Egli, D. *J. Chem. Phys.* **2006**, *125*, 224103.

[401] Gilbert, A. T. B.; Besley, N. A.; Gill, P. M. W. *J. Phys. Chem. A* **2008**, *112*, 13164–13171.

[402] Baruah, T.; Pederson, M. R. *J. Chem. Theory Comput.* **2009**, *5*, 834–843.

[403] Thom, A. J. W.; Head-Gordon, M. *Phys. Rev. Lett.* **2008**, *101*, 193001.

[404] Kowalczyk, T.; Yost, S. R.; Van Voorhis, T. *J. Chem. Phys.* **2011**, *134*,.

[405] Robinson, D.; Besley, N. A. *Phys. Chem. Chem. Phys.* **2010**, *12*, 9667–9676.

[406] Besley, N. A.; Gilbert, A. T. B.; Gill, P. M. W. *J. Chem. Phys.* **2009**, *130*, 124308.

[407] Filatov, M.; Shaik, S. *Chem. Phys. Lett.* **1998**, *288*, 689–697.

[408] Frank, I.; Hutter, J.; Marx, D.; Parrinello, M. *J. Chem. Phys.* **1998**, *108*, 4060–4069.

[409] Roothaan, C. C. J. *Rev. Mod. Phys.* **1960**, *32*, 179–185.

[410] Filatov, M.; Shaik, S. *J. Chem. Phys.* **1999**, *110*, 116–125.

[411] Grimm, S.; Nonnenberg, C.; Frank, I. *J. Chem. Phys.* **2003**, *119*, 11574–11584.

[412] Pople, J. A.; Gill, P. M. W.; Handy, N. C. *Int. J. Quantum Chem.* **1995**, *56*, 303–305.

[413] Frank, I.; Damianos, K. *J. Chem. Phys.* **2007**, *126*, 125105.

[414] Filatov, M.; Shaik, S. *Chem. Phys. Lett.* **1999**, *304*, 429–437.

[415] Kazaryan, A.; Kistemaker, J. C. M.; Schafer, L. V.; Browne, W. R.; Feringa, B. L.; Filatov, M. *J. Phys. Chem. A* **2010**, *114*, 5058–5067.